Energy Education and Research Collaboration **EERC**

# Sixth Quarterly Report
# Phase II
# December 1, 2010


Prepared by

Prof. Nariman Farvardin, Provost
Principal Investigator and EERC Project Director

Prof. Avram Bar-Cohen, Chair
EERC Project Deputy Director

Dr. Azar Nazeri
EERC Research Manager




THE UNIVERSITY OF MARYLAND AND THE PETROLEUM INSTITUTE OF ABU DHABI, UAE

# EERC Key Contributors

## University of Maryland – College Park, MD, USA

Shapour Azarm
Balakumar Balachandran
David Bigio
Hugh A. Bruck
Kyu Yong Choi
Nikil Chopra
Avram Bar-Cohen
Serguei Dessiatoun
Ashwani K. Gupta
Satyandra K. Gupta
Yunho Hwang
P.K. Kannan
Mohammad Modarres
Reinhard Radermacher
Amir Shooshtari

## Petroleum Institute – Abu Dhabi, UAE

Youssef Abdel-Majid
Ahmed Al Shoaibi
Saleh Al Hashimi
Ebrahim Al-Hajri, Returning ADNOC Scholar
Ali Almansoori
Mohamed Alshehhi
Sai Cheong Fok
Afshin Goharzadeh
Didarul Islam
Hamad Karki
Isoroku Kubo
Michael Ohadi
Peter Rodgers
Abdennour Seibi

# Table of Contents

# Executive Summary

The following is a summary of the major project activities that have taken place over the completed quarter. For more detail, see the individual reports in the last section of this report.

## Thrust 1: Energy Recovery and Conversion

**Sulfur Recovery from Gas Stream using Flameless and Flame Combustion Reactor**
A.K. Gupta, A. Al Shoaibi

- Further investigated the inner blue cone formed in $H_2/O_2$ flame upon the injection of trace amount of hydrogen sulfide.
- Investigated spectra $H_2S/O_2$ flame under lean conditions. The spectra showed strong absorption bands of $SO_2$ within 280-310nm.
- Examined $H_2S$/air flame chemical speciation under Claus conditions along the reactor axis at two different radial locations. A lower variation in combustion products was observed at R=0.5in compared to results at R=0.5in.
- Analyzed sulfur deposits formed at cold regions of the reactor and inside the sampling line using x-ray powder diffractometer. These results revealed that the deposits are cyclo-$S_8$ (α-sulfur) with orthorhombic crystal structure. The formation of α-sulfur is mainly due to the agglomeration of elemental sulfur ($S_2$) at low temperatures.

**Separate Sensible and Latent Cooling with Solar Energy**
R. Radermacher, Y. Hwang, I. Kubo

- Finished construction of the ducts.
- Finished connecting the separate ducts to each other.
- Finished sealing the ducts from inside.
- Installed the equipment into the ducts.
- Finished installation of fans.
- Prepared insulation boards for the ducts.

**Waste Heat Utilization in the Petroleum Industry**
R. Radermacher, Y. Hwang, S. Al Hashimi, P. Rodgers

- Validated cascade $CO_2$ liquefaction cycle model
- Investigated the savings from cold $CO_2$ energy recovery in the APCI LNG plant and the $CO_2$ liquefaction cycle
- Compared this work optimized MCR refrigerant mixture versus optimized MCR refrigerant mixture in literature
- Optimized of all the configurations of gas turbine triple combined cycle with single pressure steam cycle configurations.

## Thrust 2: Energy-Efficient Transport Process Projects

**Multidisciplinary Design and Characterization of Polymer Composite Seawater Heat Exchanger Module**

P. Rodgers, A. Bar-Cohen, S.K. Gupta, D. Bigio, H.A. Bruck

- Investigated the effective thermal conductivity of a PA12-carbon fiber composite used in an injection-molded prototype heat exchanger.
- Developed a technique for characterizing mixing of polymer composites in a twin screw extruder.
- Developed a discretized, mapped-meshed finite element model using hygrothermally aged mechanical properties to assess feasibility of replacing metallic heat exchangers at the Das Island liquefied natural gas facility with polymer composite heat exchangers. Several of the mapped meshes studied had lower sum of squares errors and shorter runtimes relative to the previously accepted free mesh. The final, optimized mesh had 183,500 elements, which was 64% fewer than the initial brick mesh. The reduction in elements significantly reduced computation time.
- Assessed feasibility of modeling orthotropic heat exchanger module as an isotropic model with averaged properties. The results indicate that, over the range of isotropic properties studied, the stress distributions of isotropic models do not replicate the stress distributions of an orthotropic property. As such, the orthotropic model cannot be simplified to an isotropic material with averaged properties
- Refined model simplification guidelines and techniques for mold filling metamodel of Plate-Fin polymer heat exchangers.
- Developed new datapoint selection methodology for improving the accuracy of the mold-filling statistical metamodel. The recommended techniques ensure that any computationally expensive expansions to the dataset are utilized to search the areas of the statistical metamodel that are the sources of most accuracy error.

**Microchannel-Based Absorber/Stripper and Electrostatic Precipitators for $CO_2$ Separation from Flue Gas**

S. Dessiatoun, A. Shooshtari, M. Ohadi, M. Alshehhi, A. Goharzadeh

- Improved experimental setup to eliminate gas bubbles traveling between electrodes; upgraded instrumentation on experimental setup.
- Performed experimental study of absorption of $CO_2$ in a single microchannel reactor. Results showed a nonlinear trend between the electrical conductivity and the amount of $CO_2$ absorbed by the amine solution.
- Collected new set of data for lower supply flow rate of DEA solution (i.e. 10 ml/min) into the microchannel. The results showed slightly better absorption performance compared to the results obtained for a twice higher flow rate of DEA solution.

**Microreactors for Oil and Gas Processes Using Microchannel Technologies**

S. Dessiatoun, A. Shooshtari, M. Ohadi, K.Y. Choi, A. Goharzadeh, E. Al-Hairi

- Designed tubular polymerization microreactor
- Initiated study of ethylene absorption in the diluent

## Thrust 3: Energy System Management

**Integration of Engineering and Business Decisions for Robust Optimization of Petrochemical Systems**

S. Azarm, P.K. Kannan, A. Almansoori, S. Al Hashimi

- Conducted preliminary research on extending our recently developed optimization technique to consider both irreducible and reducible interval uncertainties.
- Proposed a simulation model using an agent-based approach for modeling multiple competing petrochemical firms in a market system.
- Improved an engineering simulation model of a reactor-distillation process using Aspen HYSYS.
- Continued work on recent joint publications.

**Dynamics and Control of Drill Strings**

B. Balachandran, H. Karki, Y. Abdelmagid

- Conducted parametric studies of a drill-string system. The rotor exhibits regular orbital motions at low driving speeds but this behavior becomes irregular with increase of the drive speed in a moderate speed range. For higher speeds, the rotor is seen to return regular orbital motions before it reverts back to irregular motions at the highest end of speeds used in the present studies.
- Examined motions and trajectories of the rotor through experimental and numerical investigations with a reduced-order model. The initial rotor position is an important determinant of the rotor motions, due to the contact between the rotor and the outer shell.

**Studies on Mobile Sensor Platforms**

B. Balachandran, N. Chopra, H. Karki, S.C. Fok

- Ran EKF SLAM algorithm and obtained results
- Constructed experimental setup to test SLAM algorithms

**Development of a Probabilistic Model for Degradation Effects of Corrosion-Fatigue Cracking in Oil and Gas Pipelines**

M. Modarres, A. Seibi

- Performed literature review specifying the temperature dependencies of creep curve parameters
- Compared empirical and Evan's creep models by applying statistical methods
- Renewed the separation of the Winbugs corrosion-fatigue model to corrosion and corrosion-fatigue parts. This time, we used the pitting corrosion data from the PI intern program to update the Winbugs corrosion model
- Prepared experimental test setup for experimental efforts in support of corrosion and creep model development.

# Introduction

The EERC enjoyed a busy sixth quarter. In addition to continued progress on individual projects, visits between the two institutions furthered collaboration. Professor Mike Ohadi is, of course, back at UMD, with a new Provost at PI, Dr. Ismail Tag, taking the position in September 2010. Dr. Nazeri visited PI in October and met with the new Provost and many PI faculty and administration officers. While UMD/PI research collaboration is going strong, Dr. Nazeri observed that a more systematic transfer of best practices in education and administration from UMD to PI could be of great benefit to PI. As a result, in consultation with interested faculty and staff at PI, a plan was developed to expand EERC activities into programs such as mini-Baja, student exchange, women in engineering and others. Each program has identified faculty and staff who will sponsor the work on the PI side. This program was introduced to EERC faculty and students in a video conference on December 4th. The following explains these activities in detail:

1. **Women in Science and Engineering**: By learning from a similar program at UMD, this program will enhance recruiting of future students to PI's Women in Science and Engineering Program, improve retention of existing students, promote the role of women in engineering fields, and establish mentorship programs at local levels for female students.

   **Program Coordinator**: Director of Women in Science and Engineering – WISE Program (Dr. Nadia Alhasani) and one female faculty

2. **Team Building Workshop:** This program will focus on PI's efforts towards obtaining ABET accreditation. A series of faculty workshops and lectures will be offered through PI's CELT to facilitate team building in the curricula and explore various strategies to ensure the desired outcomes.

   **Program Coordinators:** Head of CELT (Dr. Brian Bielenberg) and ABET Coordinator (Dr. Mohan Rao)

3. **Student Exchange Program**: This program allows undergraduate UMD and PI students to study at both campuses for a short period during winter or summer break or for a semester long stay. Students will take classes and engage in research and other academic and student activities at the host institution. This program offers once in a life-time experience for engineering students at UMD to take courses at PI, interact on a daily basis with people of different cultures, and learn valuable skills for success in college and beyond. After having participated in a study abroad experience, students often return more mature and motivated in their studies and report higher levels of international awareness and intercultural understanding, which are fundamental to fostering peace in our world.

   **Program Coordinator:** Director of Student Affairs (Dr. Sami Ainane)

4. **Short Sabbaticals of PI faculty at UMD:** PI and UMD faculty may spend a summer or a semester at the other institution to teach and conduct research on collaborative projects or new initiatives. This will bring valuable research and

educational resources otherwise unavailable to the faculty at their own campuses.

**Program Coordinator:** PI Faculty (TBD)

5. **Baja SAE**: This program is a student-based international competition that centers on designing and building an all-terrain car, which would then be entered into an international competition. This program will be modeled and guided by a similar program at UMD, which has consistently been a winner in the national and international competitions. This program will: 1) provide opportunities for engineering students to apply traditional classroom knowledge to complicated hands-on projects, 2) develop engineering skills and teach team work, responsibility and organization, and 3) encourage participation of PI in international competition, thus providing international visibility for the institution.

   **Program Coordinator:** Associate Chair of Mechanical Engineering + 1 faculty + 1 lab engineer (Dr. Nader Vahdati)

6. **Transfer of Best Practices in Administration**: UMD will continue to work with PI to streamline the processes that facilitate the collaboration's activities, and help remove obstacles for programs such as the summer internship program, application and admission of graduate students and ADNOC Scholars to UMD, and course delivery to graduate students.

   **Program Coordinator:** EERC Coordinator (Dr. Ebrahim Al Hajri)

7. **Distance-Delivery of Master of Engineering Programs and Certificates:** This program is to develop and offer, in coordination with the Office of Advanced Engineering Education (OAEE) at UMD, a Master of Engineering program and a certificate program to PI graduate students, ADNOC engineers and the Abu Dhabi engineering community. The specific projects of particular interest to PI, based on previous consultations, are project management, fire protection, risk and reliability, and energy. These unique and highly rated programs can lead to degrees and certificates through 100% on-line courses.

   **Program Coordinator:** Manager of Continuing Education (Dr. Isoroku Kubo) and Dr. Clarence Rodrigues

8. **Bridging between ADNOC and Research:** PI will work with UMD to facilitate the exposure of EERC research activities to ADNOC and Operating Companies (OpCos) to establish the necessary connections between EERC research faculty (both UMD and PI) and the oil and gas industries to promote the understanding of the ADNOC research needs by faculty at UMD and PI and OpCos' understanding of the faculties expertise and capabilities.

   **Program Coordinator:** Director of Research (Dr. Karl Bertussen)

The major source of funding for the above programs will be provided from the "New Initiation" funds of EERC Phase II, upon mutual understanding and agreement of PI and UMD. The programs can start as soon as the details of the programs and their budgets are worked out and agreed upon by both sides. A detailed work plan, to include the schedules, budgets, goals and outcomes of each project, will be developed with the respective Program Coordinator to ensure successful launch and implementation. Dr. Azar Nazeri, the Program Manager of the EERC, will be responsible for developing, establishing and executing the programs from the UMD side.

# Individual Project Reports

# Thrust 1
# Energy Recovery and Conversion

# Sulfur Recovery from Gas Stream using Flameless and Flame Combustion Reactor

**UMD Investigators: Ashwani K. Gupta**
**GRA: Hatem Selim**
**PI Investigators: Ahmed Al Shoaibi**
**Start Date: October 2006**

## 1. Objectives / Abstract

The main objective is to obtain fundamental information on thermal process of sulfur recovery from sour gas by conventional flame combustion as well as flameless combustion, using numerical and experimental studies. Our ultimate goal is to determine optimal operating conditions for enhanced sulfur conversion. Therefore, an experimental study of the flameless combustion processes of the Claus furnace is proposed so that the results can be used in the normal flame process for determining improved performance. In this study we will explore different operating conditions and perform in flame and exhaust gas analyses of both flame and flameless modes of reactor operation in order to seek our quest for better understanding of the process with the goal to attain enhanced sulfur capture efficiency.

Specific objectives are to provide:

- A comprehensive literature review of the existing flame combustion process for sulfur removal with special reference to sulfur chemistry
- Near isothermal reactor conditions and how such conditions assist in the enhanced sulfur recovery process
- CFD simulation of the flame and flameless combustion in the furnace.
- Determination of the chemical kinetics and the major reaction pathways to seek for high performance
- Design of a reactor for experimental verification of the numerical results
- Measurements and characterization of the combustion furnace under various conditions, including the conditions that utilize high temperature air combustion principles for flameless combustion
- Experiments with different sulfur content gas streams using the flame and flameless combustion furnace modes of operation.
- Installation of the appropriate diagnostics for quantification of stable and intermediate sulfur compounds in the process and exit stream
- Flow, thermal and chemical speciation characteristics of the reactor
- Product gas stream characteristics and evaluation of sulfur recovery and performance in the process

## 2. Deliverables for the Completed Quarter

- Further investigation of the blue cone spectrum using both coarse and fine spectrometer gratings according to their suitability for spectra representation. The results are coupled with the chemical speciation of the blue cone using gas chromatograph.
- Examine the emission spectrum of $H_2S/O_2$ flame under lean conditions ($\Phi$=0.5) and couple the obtained results with the reaction chemistry.
- Investigate the chemical speciation of $H_2S$/air flame axially at two different radial locations (R=0.0, R=0.5in). The reactants mixture was set at Claus conditions.
- Investigate the crystal structure of sulfur deposits formed inside the sampling line and the cold regions of the reactor using X-Ray powder diffractometer.
- Initiate writing two technical papers for submission to publication in a journal.

## 3. Summary of Project Activities

During the reported quarter, our progress continued with major focus on the experimental part of the project. Further investigation of the inner blue cone formed in $H_2/O_2$ flame upon the injection of trace amount of hydrogen sulfide was conducted. The first approach of the study was to provide full details of the emission spectrum of the blue. The global spectrum was obtained using the coarse grating, and the fine grating was used for presenting the details of the spectrum. The second approach was to couple results of the spectrographs with the chemical speciation of the blue cone in order to gain insight about blue cone chemical reactions.

The emission spectrum of $H_2S/O_2$ flame under lean conditions ($\Phi$=0.5) was investigated using only the fine grating of the spectrometer. It was not possible to use coarse grating in the spectrometer for obtaining global spectrum because of the wide variation in peak intensity, which hindered showing all the spectrum details in one spectrograph. On the other hand, we tried to repeat the same study on $H_2S$/air flame, but it did not give promising emission spectrographs in which significant emissions were observed. The $H_2S$/air flame had a very faint whitish color.

Examination of $H_2S$/air flame speciation has been conducted under Claus conditions. The experimental setup has been modified to be able to scan the reactor in both the radial and axial directions by adding another traverse mechanism in the radial direction. Both traverse mechanisms move independently in the radial and axial directions. The reactor was scanned axially at two different radial locations. We also tried to implement the same investigation on $H_2S/O_2$ flame under Claus conditions, but the flame was highly unstable because of its low flame speed, which caused the flame to persistently blow out during gas sampling.

During all our experiments sulfur deposits were formed inside the gas sampling line and on the relatively cold regions of the reactor. The deposits were skimmed off of the reactor and analyzed at the x-ray crystallographic laboratory at UMD. Sulfur deposits crystal structure was analyzed using x-ray powder diffraction.

During the past quarter we started writing two technical papers to be submitted for journal publications.

## 4. Progress

### 4.1 $H_2$/air and blue cone optical emission spectroscopy

Experiments were conducted to investigate the emission spectrum of hydrogen/air flame without/with the addition of trace amounts of hydrogen sulfide.

*Experimental conditions*

Hydrogen flow rate: 3 lit/min

Air flow rate: 7.2 lit/min

$H_2S$ flow rate: 4 $cm^3$/min

Figure 1 shows a wide spectrum of hydrogen/air flame between 230nm and 500nm. The spectrum shows one global peak around 309.13nm, which is attributed to OH* radical. Figure 2 elaborates the global peak of OH* radical using the fine grating between 250nm and 315nm. Three major peaks of OH* radical were observed: the first peak is at 306.13nm, the second and the strongest peak is at 309.09 nm, and the third major peak is at 312.9nm. These results agree with the findings reported in the literature by several investigators. However, the wave length of the strongest peak of OH* is controversial, having been reported at 306, 307.8, 308, and 310nm.

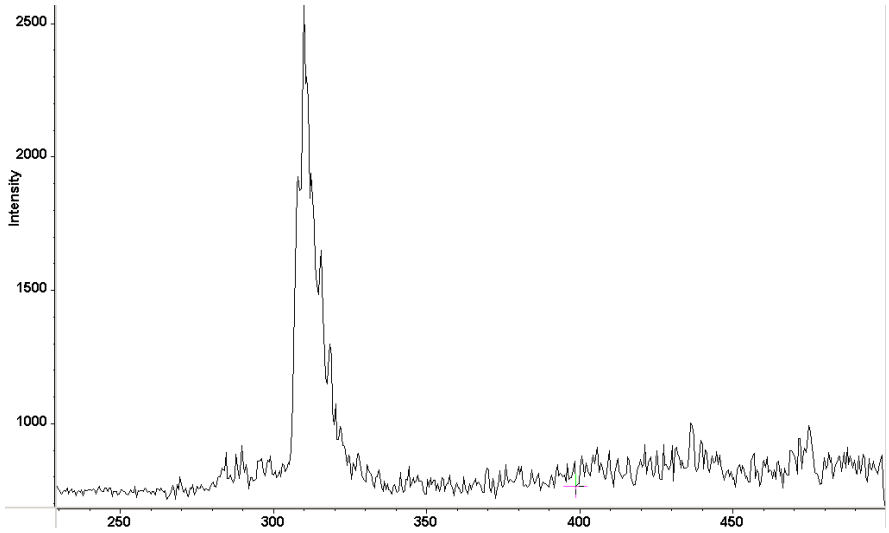


**Figure 1. Emission spectrum of hydrogen/air flame (230nm-500nm).**

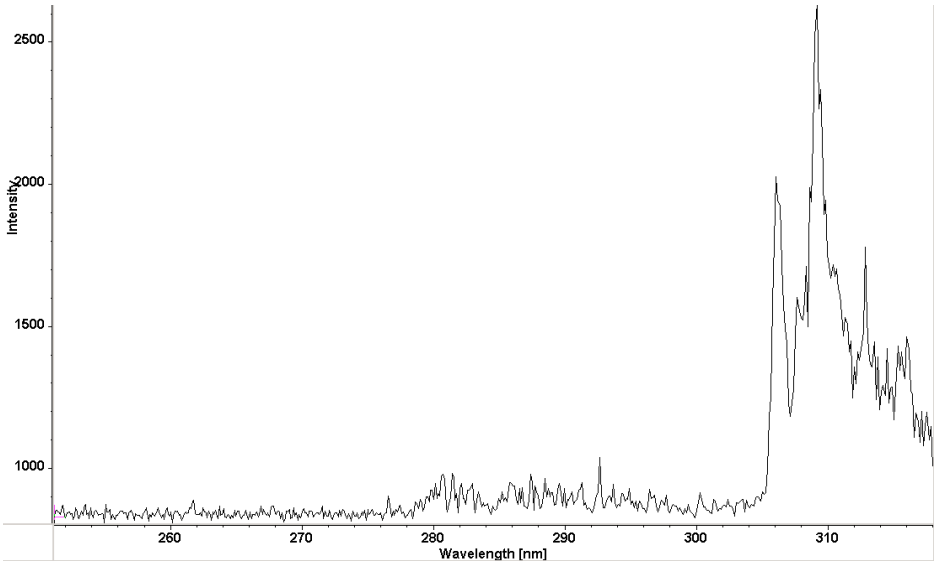


**Figure 2. Emission spectrum of hydrogen/air flame (250nm-318nm).**

Hydrogen/air flame has a very faint color (almost colorless), but with the addition of a trace amount of $H_2S$ a strong bluish inner cone was formed at the flame base. Figure 3 shows the spectrum of this blue cone using the coarse spectrometer grating. A strong series of peaks can be observed between 330 and 470nm. On the other hand, the previously observed OH* peaks were suppressed significantly upon the addition of $H_2S$. Only the strongest peak of OH* at 309.09nm could be observed. The reaction of hydrogen sulfide consumes OH during the reaction to form primarily SO then $SO_2$ as an end product. This justifies the deterioration that occurred in OH* peaks. It is worth noting that the fiber optic used for emitted light collection was placed in the same location for all presented spectra at $L= Z/D_{jet}=1.773$, where Z is the distance in axial direction measured from the burner tip and $D_{jet}$ is the diameter of the inner injection tube of the burner.

The emission spectrum of the inner blue cone does not change within the core of blue cone. However, the spectrum of the inner blue cone starts to fade near its tip (L=5.32) and the OH* peak becomes the dominant peak. Figure 4 shows the spectrum at the tip of the inner blue cone where the OH* peak becomes dominant and the blue cone bands start to diminish. This proves that hydrogen sulfide combustion has almost completed, which will be further verified with the GC results. The spectrum of the blue cone has been divided into small spectra using the fine grating in order to identify accurately the wavelength of each peak and to give better understanding of the chemical reactions.

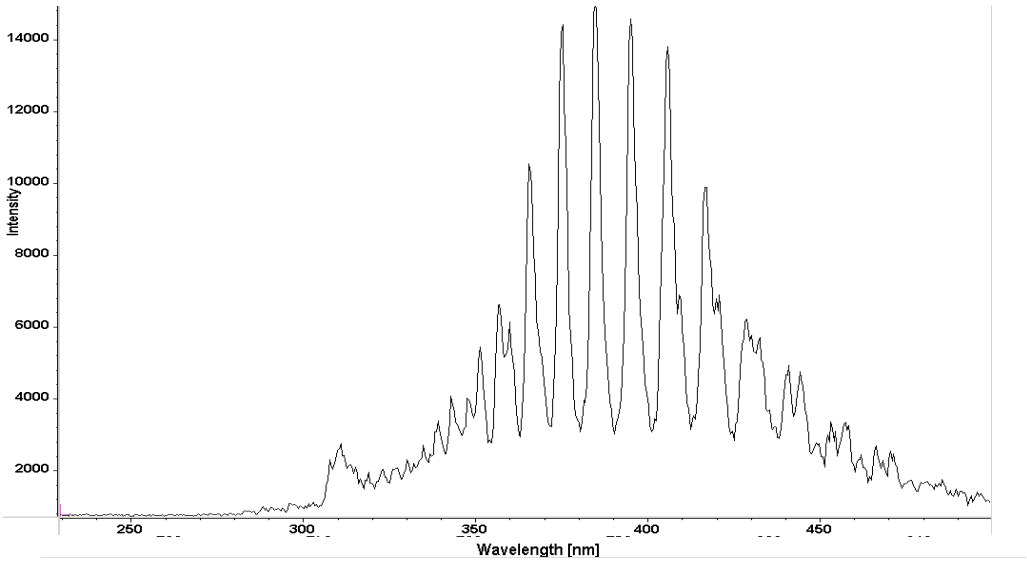


**Figure 3. Emission spectrum of hydrogen/air flame, with addition of $H_2S$ (230nm-500nm).**

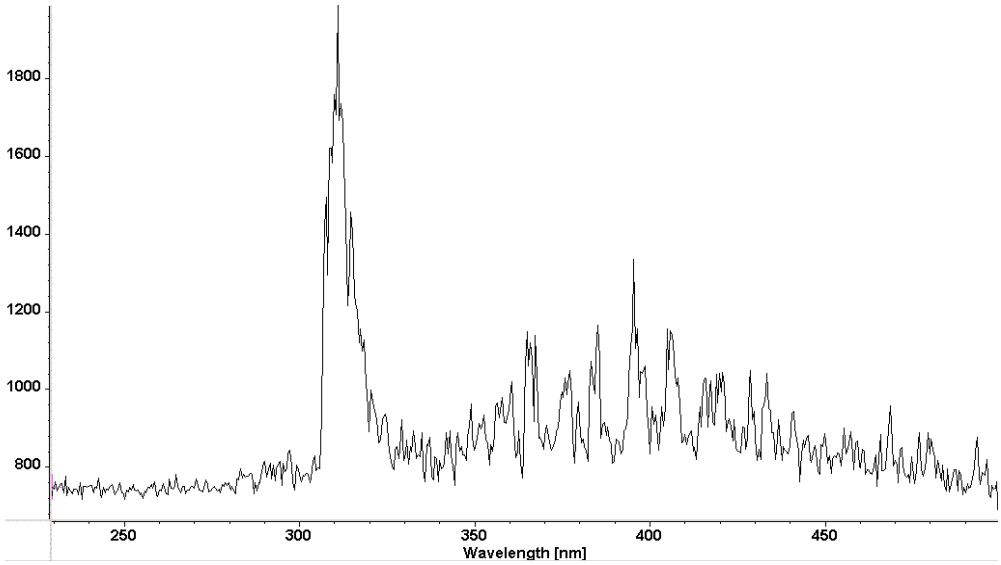


**Figure 4. Emission spectrum of hydrogen/air flame, with addition of H2S, at the tip of the inner cone (230nm-500nm).**

Figures 5, 6, and 7 present in detail the spectrum of the inner blue cone formed in hydrogen/air flame upon the injection of a trace amount of hydrogen sulfide. No significant bands were observed below 306nm. The peaks observed beyond 320nm have been attributed by several investigators to SO*, $SO_2$*, or $SO_3$*. The spectrum of SO* was found to be extended from 394.1nm to 244.2nm with more than 40 peaks distributed along this band of wavelengths. However, these bands are not likely to be occurring under one condition, and they are more common in rich flames. In the current study, it is unlikely to have all these bands since the concentration of sulfur species is very minimal and the mixture is slightly lean. However, some of the observed bands can be attributed to SO* which are the relatively weak bands within 320-350nm. The likelihood that $SO_2$* is the cause of the blue cone bands beyond 350nm is minimal, as the GC analysis of the combustion products inside the blue cone did not show any sign of $SO_2$ (figs. 9, 10 and 11). Moreover, the reported spectra of $SO_2$* showed the presence of a group of distinct peaks superimposed on a continuum band, which is attributed to $SO_2$ afterglow. Sulfur dioxide afterglow causes increase in the background signal of the spectrum between 250nm and 500nm (details of $SO_2$ afterglow will be discussed later). The explanation of $SO_3$* as responsible for the peaks beyond 340nm is the most acceptable one. Several investigators in the literature suggested that the peaks beyond 350nm are attributed to the presence of $SO_3$*. Sulfur trioxide can be formed in the reaction zone due to the reaction between sulfur dioxide and atomic oxygen or hydroxyl group as follows:

$$SO_2 + O \Leftrightarrow SO_3 + 81\ Kcal \quad (1)$$

$$SO_2 + OH \Leftrightarrow SO_3 + H - 20Kcal \quad (2)$$

Reactions (1) and (2) create a strong channel for the formation of $SO_3$*, which is responsible for the continuous band of peaks beyond 350nm. On the other hand, excited hydrogen radical possesses an important role in $H_2S$ combustion. Therefore, peaks beyond 400nm are likely attributed to the Balmer series formed by H*. Sulfur trioxide is responsible for most of the peaks within 350-400nm, while H* is responsible for most of the peaks above 400nm. However, the interference between $SO_3$* peaks and H* peaks is still an issue that needs further investigation. Hydrogen radical is formed through the group of reactions as follows:

$$SO_2 + OH \Leftrightarrow SO_3 + H \quad (3)$$
$$S + OH \Leftrightarrow SO + H \quad (4)$$
$$SO + OH \Leftrightarrow SO_2 + H \quad (5)$$

Reactions (2) through reaction (5) also elucidate the suppression observed in OH* peaks upon the injection of $H_2S$.

Even though SH is considered the most important intermediate species during $H_2S$ combustion, it did not show strong bands in this presented spectrum. The bands of SH* emission are difficult to distinguish in the spectrum because it is mostly masked by SO* peaks. However, absorption bands of SH are the proper method to distinguish its presence. Absorption bands of SH are reported in the literature to be at 323.5nm and 327.8nm. This relatively agrees with the results presented in this investigation where the light intensity shows its lowest magnitudes at 324.03nm and 328.62nm. Table 1 shows the wavelength of all peaks observed in the spectrum of the inner blue cone:

**Table 1. Blue cone emissions peaks**

| Wavelength (nm) | Species | Wavelength (nm) | Species | Wavelength (nm) | Species |
|---|---|---|---|---|---|
| 309.09 | OH* | 346.59 | SO* band | 408.43 | $SO_3$ and H* bands |
| 322.21 | SO* | 347.83 | | 415.86 | |
| 324.03 | SH (absorption band) | 349.85 | | 425.71 | |
| 326.62 | SO* | 355.24 | $SO_3$ and H* bands | 430.0 | |
| 328.62 | SH (absorption band) | 358.77 | | 439.6 | |
| 333.92 | SO* band | 364.75 | | 443.7 | |
| 336.99 | | 368.42 | | 449.09 | |
| 338.97 | | 373.42 | | 453.8 | |
| 341.61 | | 383.16 | | 458.8 | |
| 343.15 | | 393.71 | | 465.2 | |
| 344.7 | | 404.57 | | | |

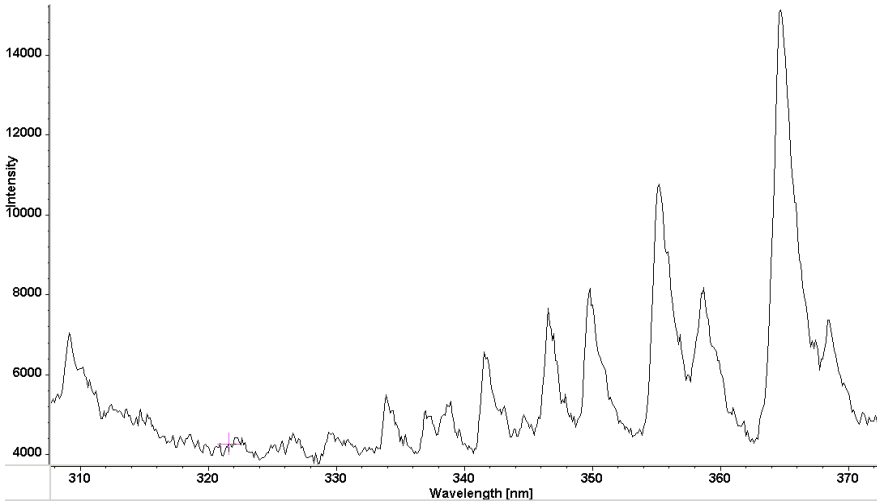


**Figure 5. Emission spectrum of hydrogen/air flame, with addition of trace amount of $H_2S$ (308-372nm).**

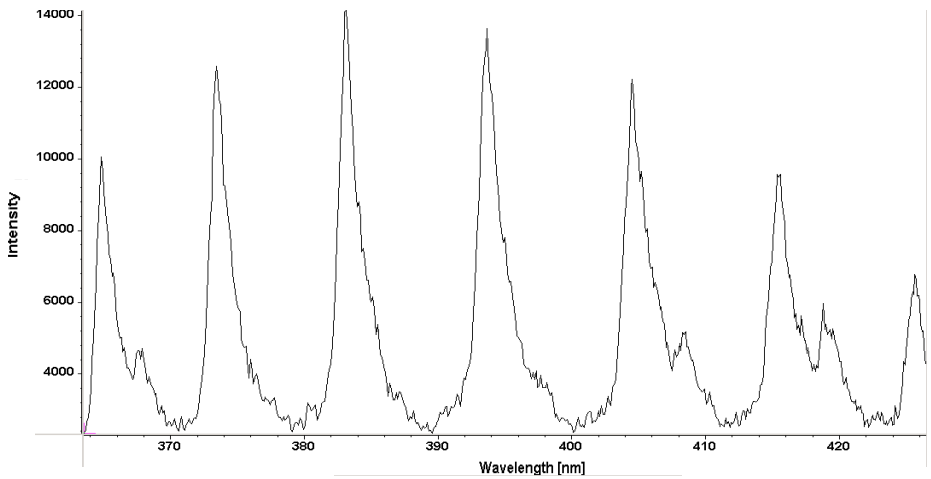


**Figure 6. Emission spectrum of hydrogen/air flame, with addition of trace amount of $H_2S$ (364-426nm).**

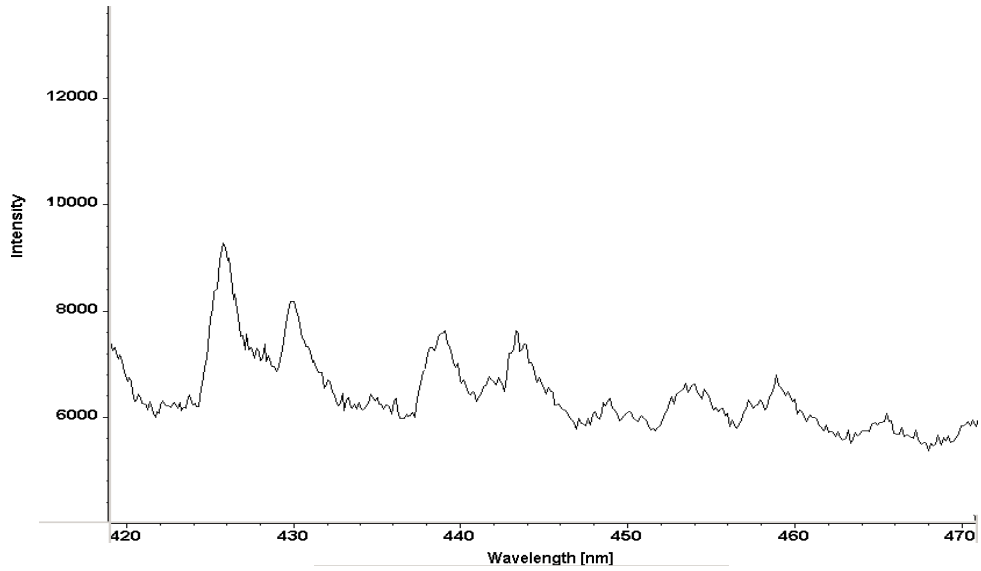


**Figure 7. Emission spectrum of hydrogen/air flame, with addition of trace amount of $H_2S$ (420-470nm).**

Gas chromatograph was used for sampled gas analysis at different points of the blue cone. Figure 8 shows a photo of the blue cone, and the axial and radial sampling locations as function in (L and W), where

W= $R/D_{jet}$
R: distance in radial direction measured from the burner centerline
$D_{jet}$: diameter of the inner injection tube of the burner

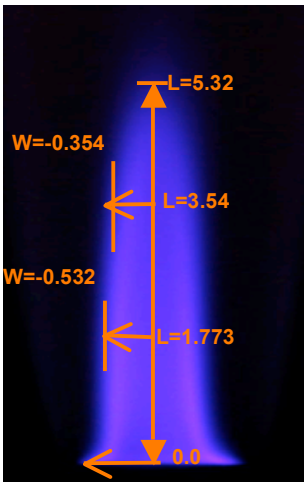


**Figure 8. Photo of the inner blue cone formed in $H_2$/air flame upon the injection of $H_2S$.**

Due to symmetry, gas sampling was carried out on only one half of the cone. Figures 9, 10, and 11 present mole fraction of stable combustion products $H_2S$, $H_2$, and $O_2$, respectively. The figures show that $H_2S$ is totally consumed at the tip of the inner cone, which supports the previous conclusions based on emission spectra. On the other hand, the chromatograms did not contain any $SO_2$ mole fraction, which verifies the interpretation of the formation of $SO_3$ discussed above.

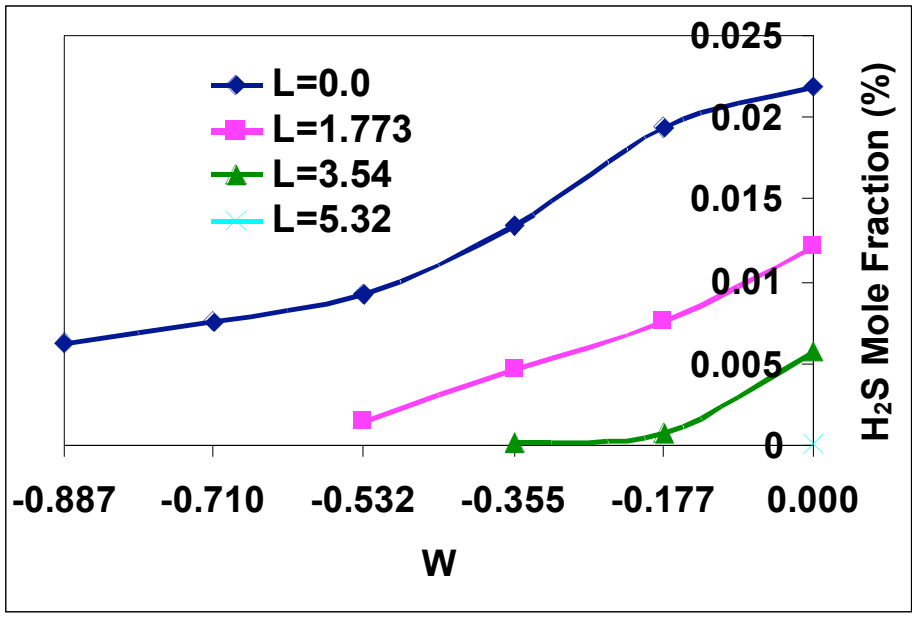


**Figure 9. Axial and radial distribution of $H_2S$ mole fraction within the inner blue cone.**

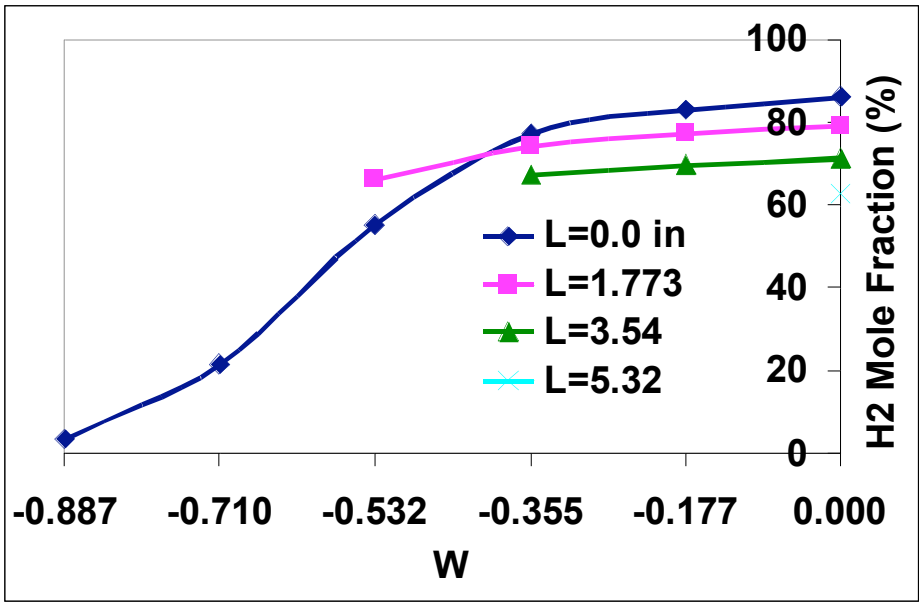


**Figure 10. Axial and radial distribution of $H_2$ mole fraction within the inner blue cone.**

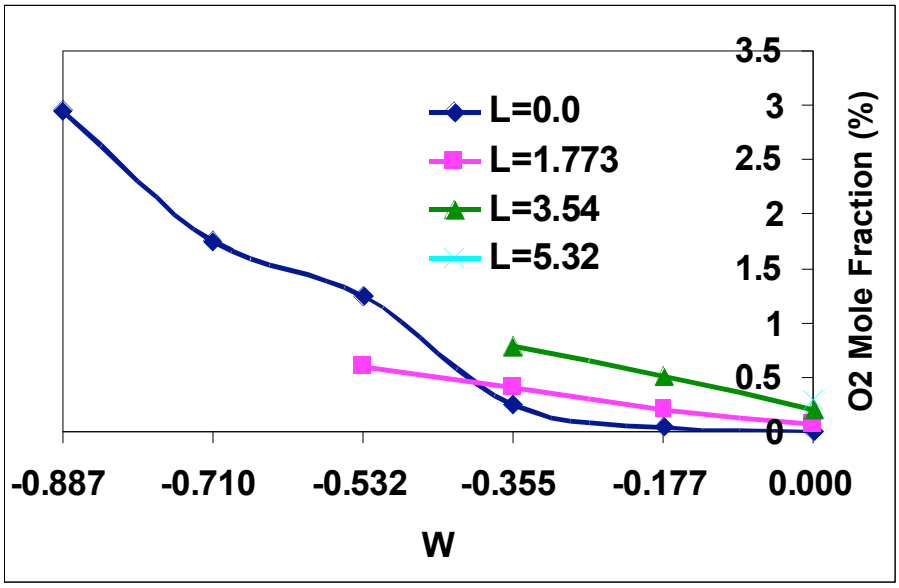


**Figure 11. Axial and radial distribution of $O_2$ mole fraction within the inner blue cone.**

### 4.2 $H_2S/O_2$ optical emission spectroscopy

Experiments were conducted to investigate the emission spectrum of hydrogen/oxygen flame under lean conditions (Φ=0.5). It is also important to note that we tried to repeat the same approach applied here on hydrogen/air flame, but the spectrum did not show any significant emission bands. This flame had a relatively low temperature and had a faint white color.

*Experimental conditions*

$H_2S$ flow rate: 0.3 lit/min

Oxygen flow rate: 0.9 lit/min

Figures 12, 13, 14, and 15 show the emission spectrum of $H_2S/O_2$ under lean conditions (Φ=0.5) using the fine grating of the spectrometer. It was not possible to use the coarse grating because of the wide variation in peak intensity, which hindered showing all the spectrum details in one figure. Unlike the previous case, this spectrum shows a large continuum band within 280-460nm, which is attributed to $SO_2$ afterglow. However, the spectrum also shows groups of distinct peaks superimposed on the continuum band between 280-310nm, and 360-480nm. The first group of peaks is attributed to the absorption bands of $SO_2$ in the range of 280-315nm. Although SO is considered an important intermediate species for $SO_2$ production, the presence of distinct SO* peaks is uncertain because they are, if they exist, masked by $SO_2$ strong afterglow continuum. Similar to the previous case, the second group of peaks is attributed to $SO_3$* and H*. Sulfur dioxide afterglow is a strong chemiluminescence continuum band reported in the literature to be between 250-500nm. The obtained continuum starts at ~280nm, reaches its maximum at ~365nm, and then decays until 460nm. Several investigators in the literature suggested that the afterglow continuum is formed by excited singlet and triplet states of $SO_2$*. They also suggested that the singlet emission of $SO_2$* is in the region around 350nm while the triplet emission of $SO_2$* is around 425nm. This agrees with the findings presented here, in which the continuum peaks at ~365 due to singlet $SO_2$* emission and the continuum beyond 400nm is much weaker, which is attributed to triplet emission of $SO_2$*. It is worthy to note that singlet emission is stronger than triplet emission. The group of chemiluminescent reactions responsible for this continuum is as follows:

$$SO + O \Leftrightarrow SO_2^* \quad (6)$$

$$SO_2 + O + O \Leftrightarrow O_2 + SO_2^* \quad (7)$$

Reaction (6) contributes significantly in $SO_2$ afterglow in case of high Oxygen concentrations (which is our case) and it was found to produce triplet $SO_2$ emission. Reaction (7) occurs in two steps as follows:

$$SO_2 + O + M \Leftrightarrow SO_3^* + M \quad (8)$$

$$SO_3^* + O \Leftrightarrow {}^1SO_2^* + O_2 \quad (9a)$$

$$SO_3^* + O \Leftrightarrow {}^3SO_2^* + O_2 \quad (9b)$$

In case of oxygen depletion chemiluminescent reactions will not progress to reaction (9), which indicates the absence of $SO_2$ afterglow in the blue cone spectrum. However, in the current case reaction (9) occurs in both its forms (9a and 9b) to produce singlet and triplet $SO_2$ afterglow emissions respectively. Reaction (8) was found to produce triplet excited $SO_3$*. Table 2 shows the wavelength of all peaks observed in the spectrum of $H_2S/O_2$ flame.

**Table 2. $H_2S/O_2$ emission peaks**

| Wavelength (nm) | Species | | Wavelength (nm) | Species | | Wavelength (nm) | Species | |
|---|---|---|---|---|---|---|---|---|
| 281.65 | $SO_2$ absorption bands | $SO_2$ afterglow | 300.22 | $SO_2$ absorption bands | $SO_2$ afterglow | 384.68 | $SO_3$ and H* bands | $SO_2$ afterglow |
| 283.04 | | | 302.24 | | | 386.56 | | |
| 284.75 | | | 304.29 | | | 394.74 | | |
| 286.45 | | | 306.26 | | | 397.23 | | |
| 287.94 | | | 308.75 | | | 405.11 | | |
| 289.64 | | | 311.05 | | | 411.58 | | |
| 291.23 | | | 313.67 | | | 417.03 | | |
| 292.94 | | | 360.07 | $SO_3$ and H* bands | | 421.61 | | |
| 294.65 | | | 366.09 | | | 427.99 | | |
| 296.49 | | | 369.68 | | | 432.68 | | |
| 298.35 | | | 375.7 | | | 459.17 | | |

## 4.3 Chemical speciation of $H_2S$/air flame

The chemical speciation of hydrogen sulfide/air flame was examined under Claus conditions. The gas sampling took place at two radial sections (R=0.0, R=0.5in) where two traverse mechanisms were installed and had the ability to move independently in both the radial and axial directions. However, we could not repeat the same experiment for $H_2S/O_2$ flame due to the high instability of the flame at such rich conditions.

*Experimental conditions*

$H_2S$ flow rate: 0.4 lit/min

Air flow rate: 0.95 lit/min

Figure 12 shows the axial distribution of $H_2S$ mole fraction at two radial sections. The results show lower variation in $H_2S$ mole fraction at R=0.5in compared to the results at R=0.0. This is attributed to the low axial velocity near the walls and the relatively low temperatures, which make the reaction rate very slow near the walls if it exists. Figure 13 shows the axial distribution of $SO_2$ mole fraction at two radial sections. Similarly, the results show less variation in $SO_2$ mole fraction at R=0.5in, which is attribute to the same abovementioned reasons. One can see that the $SO_2$ mole fraction almost did not change downstream beyond three inches of the reactor axial distance. The same explanation is valid for $H_2S$ mole fraction (shown in Figure 14). Figure 15 shows the axial distribution of oxygen mole fraction at two radial sections. The results show that higher oxygen mole fraction values are obtained at R=0.5in. This is attributed to the low temperatures near the reactor walls, which lessen the reaction rate and oxygen consumption.

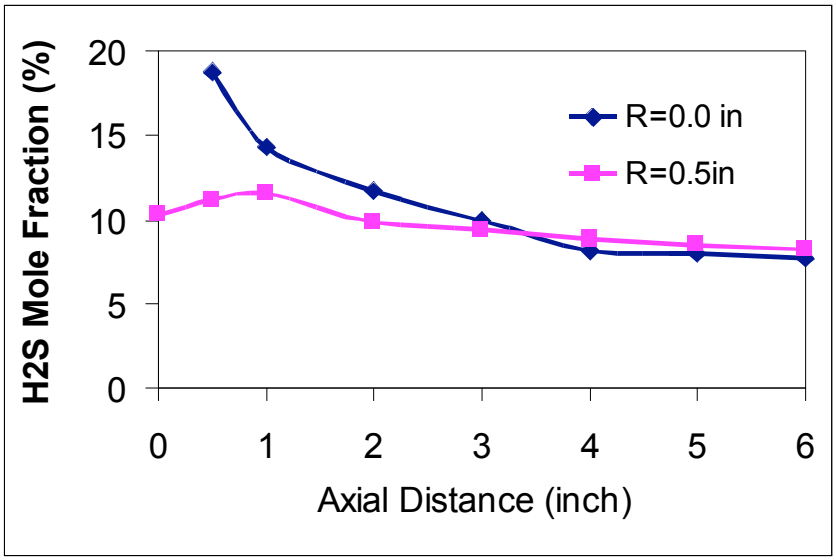


**Figure 12. Axial distribution of hydrogen sulfide mole fraction at two radial sections.**

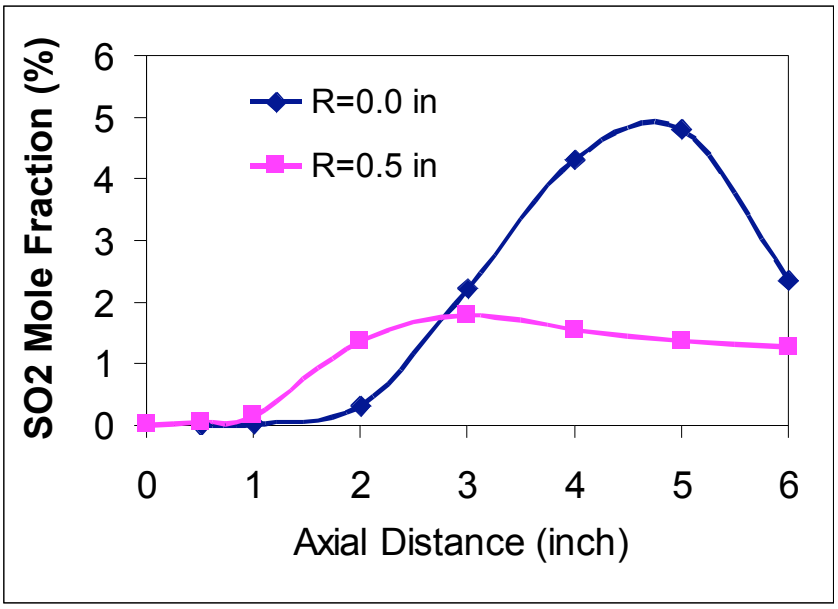


**Figure 13. Axial distribution of sulfur dioxide mole fraction at two radial sections.**

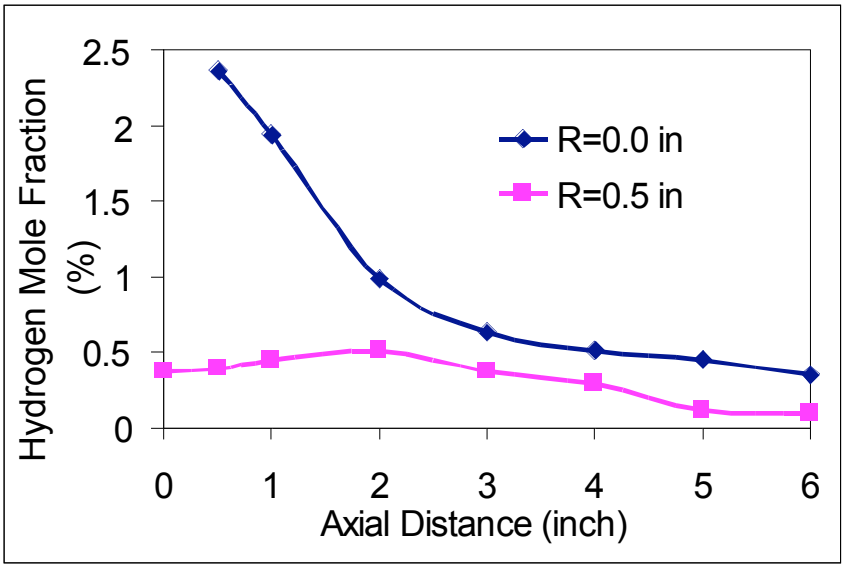


**Figure 14. Axial distribution of hydrogen mole fraction at two radial sections.**

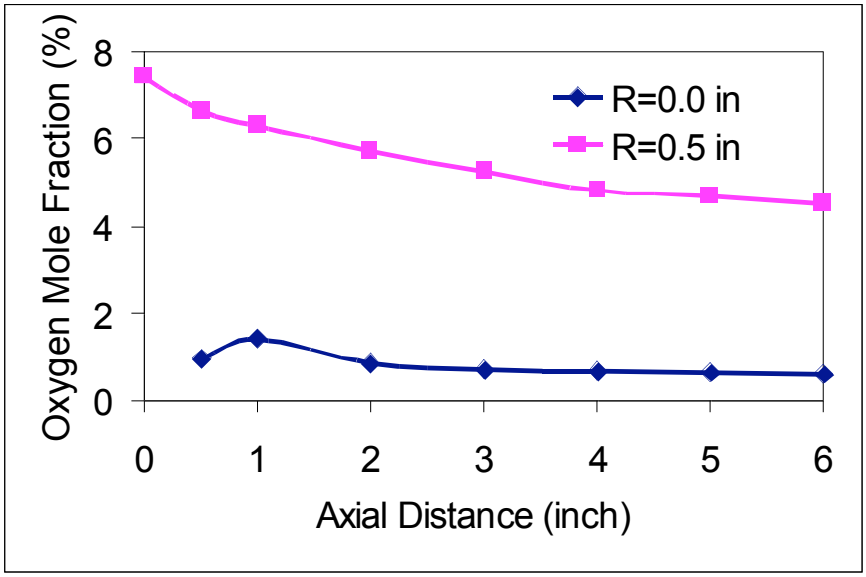


**Figure 15. Axial distribution of oxygen mole fraction at two radial sections.**

### 4.4 Analysis of sulfur-deposit crystal structure

Sulfur deposits were observed under Claus conditions at cold regions of the reactor and also inside the sampling line. The deposits have a greenish yellow color and they are formed as small fragments randomly distributed on the quartz tube reactor and inside the sampling probe. A characteristic sample of these deposits was skimmed off of the reactor in order to identify its crystal structure using the x-ray powder diffraction technique. The measurements were conducted with a Bruker D8 advance powder diffractometer using CuK-alpha radiation from sealed tube, 2.5mm Soller slits, Ni beta-filter and PSD (position sensitive detector) LynxEye with 3 degree window. The analysis revealed that the deposits were cyclo-$S_8$ (α-sulfur) with orthorhombic crystal structure. Note that sulfur formation during Claus reaction yields elemental sulfur $S_2$, but at low temperatures sulfur tends to agglomerate to form α-sulfur, which is puckered crown-shaped

rings consisting of eight sulfur atoms in each. Figure 16 shows the diffractogram of our sample (black curve) compared with two other diffractograms from the literature (red curve[1]) and (blue curve[2]). Both reported diffractograms represent $S_8$ with slightly different lattice parameters. The results qualitatively show good matching with the reported diffractograms of $S_8$.

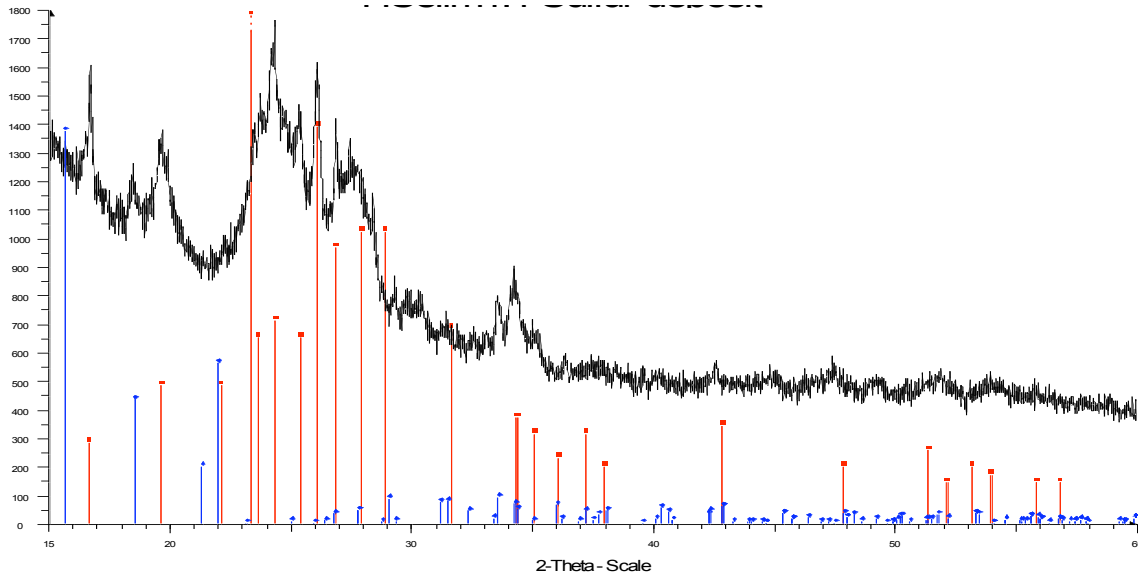


**Figure 16. The diffractogram of sulfur deposits (black) compared with the available data on $S_8$ diffractogram. $S_8$ diffractogram with a= 10.41, b= 12.84, c=24.37 lattice parameters (red); S8 diffractogram with a= 10.437, b= 12.845, c=24.369 lattice parameters (blue). All dimensions are in Angstrom.**

## 5. Conclusion

Further investigation of the inner blue cone formed in $H_2/O_2$ flame upon the injection of trace amount of hydrogen sulfide has been conducted. The global spectrum of hydrogen/air flame showed one distinct global peak of OH* at 309nm. However, higher resolution spectrum analysis proved that OH* is responsible for three major peaks at 306.13, 309.09, and 312.9nm. Addition of a trace amount of hydrogen sulfide into hydrogen/air flame caused the formation of a strong bluish inner cone near the flame base. The spectrum of the blue cone showed a very strong group of peaks within 350-470nm. On the other hand, the addition of $H_2S$ significantly weakened OH* peaks, which is attributed to the extensive consumption of OH during $H_2S$ combustion.

The group of peaks formed inside the blue cone is divided into three major bands. The first band is caused by SO* within 320-350nm, the second band is attributed to $SO_3$* within 350-400nm, and the third band is due to H* within 400-470nm. However, the distinction between the $SO_3$* band and H* band around 400nm still needs future investigation. Absorption bands of SH were observed at 324.03nm and 328.62nm. Sulfur dioxide was not proved to have significant bands in this spectrum because it reacts with elemental oxygen to produce excited sulfur trioxide. Gas chromatograph gas analysis proved that combustion products did not contain $SO_2$.

In addition, an investigation of spectra of $H_2S/O_2$ flame under lean conditions ($\Phi$=0.5) took place. The spectra showed strong absorption bands of $SO_2$ within 280-310nm. A strong continuum was observed between 280-460nm where distinct group of peaks are superimposed on it. The

continuum is attributed to singlet and triplet $SO_2$ afterglow. Singlet excited $SO_2$ afterglow is around 365nm region, while the triplet excited $SO_2$ afterglow is beyond 400nm. The superimposed peaks are attributed to $SO_3$* and H*. We tried to implement the same approach on $H_2S$/air flame but the flame was too faint-colored and did not have detectable emissions.

Furthermore, $H_2S$/air flame chemical speciation under Claus conditions was examined along the reactor axis at two different radial locations (R=0.0 and R=0.5in). A lower variation in combustion products was observed at R=0.5in compared to results at R=0.5in. This is attributed to the low axial velocities near the walls along with the relatively low temperatures which suppress the chemical reaction significantly. The same approach was attempted on $H_2S/O_2$ flame under Claus conditions but the flame was extremely unstable and persistently extinct during gas sampling.

Finally, sulfur deposits formed at cold regions of the reactor and inside the sampling line were analyzed using X-Ray powder diffractometer. These results revealed that the deposits are cyclo-$S_8$ (α-sulfur) with orthorhombic crystal structure. The formation of α-sulfur is mainly due to the agglomeration of elemental sulfur ($S_2$) at low temperatures.

## 6. Difficulties Encountered/Overcome

None

## 7. Deliverables for the Next Quarter

- Further examination of sulfur deposits collected at different axial locations using 7-channel spectrometer.
- Investigate the conditions that trigger formation of COS, $CS_2$ during methane/$H_2S$ oxidation
- Calculate sulfur mole fraction and conversion efficiency using different flames in a plug flow reactor with perfectly premixed reactants

## 8. Publications


1. Gupta, A. K. and Sassi, M. “Sulfur Recovery from Acid Gas Using the Claus Process and High Temperature Air Combustion Technology,” American J. of Environmental Sciences, Vol. 4, No. 5, 2008, pp. 502-511.
2. Selim, H., Gupta, A. K. and Sassi, M. “Variation of Optimum Claus Reactor temperature with Acid Gas Composition,” IECEC Conference, Cleveland, OH, July 28-30, 2008, Paper No. AIAA-2008-5797.
3. Selim, H., Gupta, A. K. and Sassi, M. “Reduced Mechanism for Hydrogen Sulfide Oxidation,” 47th AIAA Aerospace Sciences Conference, Orlando, FL, January 5-8, 2009, Paper No. AIAA-2009-1392.
4. Selim, H. and Gupta, A. K. “Nonreactive Study for the Reactants Mixing in Claus Reactions,” 7th Intl. Energy Conversion Engineering Conference (7th IECEC), Denver, CO, August 2-5, 2009, Paper No. AIAA-2009-4506.
5. Selim, H, Gupta, A. K. and Sassi, M. “Reduction and Validation of Detailed Kinetic Reactions in Thermal Stage of Claus Process,” 48th AIAA Aerospace Sciences Conference, Orlando, FL, (accepted for presentation and Publication), January 3-7, 2010, Paper AIAA-2010-1356.
6. Al Amoodi, N., Selim, H., Gupta, A. K., Sassi, M. and Al Shoaibi, A. “Numerical Simulations of the Thermal Stage in Claus Process: Equilibrium and Kinetic Investigation,” 48th AIAA Aerospace Sciences Conference, Orlando, FL, (accepted for presentation and publication), January 3-7, 2010, AIAA-2010-1355.
7. Selim, H. Vijayan, V., Al Shoaibi, A., and Gupta, A. K., “Numerical and Experimental Studies on Mixing and Product Species Distribution in a Claus Reactor,” 8th Intl. Energy Conversion Engineering Conference (8th IECEC), Nashville, TN, August 2-5, 2009, Paper

No. AIAA-2010-7183.
8. Selim, H, Al Shoaibi, A., and Gupta, A. K., “Effect of $H_2S$ in Methane/Air Flames on Sulfur Chemistry and Products Speciation,” To be submitted
9. Selim, H, Al Shoaibi, A., and Gupta, A. K., “Emission Spectra of Hydrogen Sulfide Flames,” To be submitted

## Appendix

### Justification and Background

Hydrogen sulfide is present in numerous gaseous waste streams from natural gas plants, oil refineries, and wastewater treatment plants, among other processes. These streams usually also contain carbon dioxide, water vapor, trace quantities of hydrocarbons, sulfur, and ammonia. Waste gases with ammonia are called sour gases, while those without ammonia are called acid gases. Sulfur must be recovered from these waste streams before flaring them. Sulfur recovery from sour or acid gas typically involves application of the well-known Claus process, using the reaction between hydrogen sulfide and sulfur dioxide (produced at the Claus process furnace from the combustion of $H_2S$ with air and/or oxygen), yielding elemental sulfur and water vapor: $2H_2S(g) + SO_2(g) = (3/n)\ S_n(g) + 2H_2O(g)$ with $\Delta H_r$= -108 kJ/mol. Therefore, higher conversions for this exothermic, equilibrium-limited reaction call for low temperatures, which lead to low reaction rates that dictate the use of a catalyst. The catalytic conversion is usually carried out in a multistage, fixed-bed, adsorptive reactor process, which counteracts the severe equilibrium limitations at high conversions. This technology process can convert about 96% to 97% of the influent sulfur in $H_2S$ to S. However, higher removal requires critical examination of the process and use of a near isothermal reactor, since the conversion is critically dependent upon the exothermic and endothermic conditions of the reactions.

Flameless combustion has been shown to provide uniform thermal field in the reactor so that the reactor temperature is near uniform. Reactor size can also be reduced and combustion-generated pollutants emissions can be reduced by up to 50%. Energy efficiency can be increased by up to 30%. The application of this technology appears to offer great advantages for the processes under consideration. The UAE, which pumps about 2.4 million bpd of crude oil, is also home to the world's fifth biggest gas reserves at about 200 trillion cubic feet. Abu Dhabi Gas Industries (GASCO), an operating company of the Abu Dhabi National Oil Company (ADNOC), is leading a drive to boost gas production in the UAE from five to seven billion cubic feet per day. This calls for sulfur recovery capacity of over 3,000 metric tons per day with the associated SOx and NOx emissions. Therefore, the adoption and further development of flameless combustion technology for sulfur recovery among other commercial and industrial heating processes is expected to be crucial and beneficial, both economically and environmentally.

The conventional sulfur recovery process is based upon the withdrawal of sulfur by in situ condensation within the reactor. The selective removal of water should, however, be a far more effective technique, as its effect on the equilibrium composition in the mass action equation is much greater. The in situ combination of the heterogeneously catalyzed Claus reaction and an adsorptive water separation seems especially promising, as both reaction and adsorption exhibit similar kinetics, and pressure can be adapted to the needs of the adsorptive separation. Such an adsorptive reactor will lead to almost complete conversion as long as the adsorption capacity is not exhausted. There are numerous possibilities for implementing these two functions, ranging from fixed-beds with homogeneous catalyst/adsorbent mixtures to spatially structured distributions or even fluidized beds. Most of the previous studies have concentrated on the Claus catalytic conversion reactors and the TGTU. However, some previous studies have identified the Claus furnace as one of the most important yet least understood parts of the modified Claus process. The furnace is where the combustion reaction and the initial sulfur conversion (through an endothermic gaseous reaction) take place. It is also where the $SO_2$ required by the downstream catalytic stages is produced and the contaminants (such as ammonia and BTX (benzene, toluene, xylene) are supposedly destroyed. The main two reactions in the Claus furnace are: $H_2S + 3/2\ O_2 = SO_2 + H_2O$, with $\Delta H_r$= -518 kJ/mol, and $2H_2S + SO_2 = 3/2\ S_2 + 2H_2O$, with $\Delta H_r$= +47 kJ/mol. This last endothermic reaction is responsible for up to 67% conversion of the sulfur at about 1200 °C. Moreover, many side reactions take place in the furnace; these side reactions reduce sulfur recovery and/or produce unwanted components that end up as ambient pollutant emissions. Therefore, it would be useful to combine the endothermic and exothermic process using an isothermal reactor offered by flameless oxidation combustion.

## Approach

***Critical review***

We propose to conduct a critical review of the various approaches used for sulfur removal from the sour gas. The emphasis here will be on sulfur chemistry with due consideration to the fate of ammonia. Following the review, an experimental and a CFD numerical study of the flameless oxidation of the fuel will be conducted as follows:

***CFD simulation***

A numerical simulation study of the flame under normal and flameless oxidation of fuels in the furnace will be conducted using the available codes. Global features of the flow and thermal behavior will be obtained using the Fluent CFD and Chemkin computer codes. These codes provide detailed simulation of the flow, thermal and chemical behaviors (i.e., detailed chemistry) in the reactor flow using gas-phase reactants. The sulfur in the fuel is in gas phase, so we will be able to simulate and monitor the fate of sulfur during various stages of endothermic and exothermic reactions and over a range of temperature regimes, including those covered in the Claus furnace process. The simulation results will also guide the final design of the flameless furnace. The simulations will also help assist in the experimental program for data validation with the eventual goal of implementing the process for sulfur removal.

***Experimental study***

An experimental study of the flameless vs. normal flame combustion process for the conditions examined in the theoretical study, including that of Claus furnace, will be conducted. We will explore the operating conditions and the exhaust gas analysis under conditions of both flame and flameless modes to determine the extent of sulfur conversion under the two conditions over the temperatures that can simulate endothermic and exothermic conditions in the Claus furnace. The goal is to seek conditions that yield the highest sulfur recovery from a process. To some extent, these conditions will be based on the composition of the acid/sour gas, from sulfur-rich (> 50% $H_2S$) to lean (< 20% $H_2S$). It is expected that our fundamental information will contribute to the eventual design guidelines of an advanced sulfur recovery process furnace operating under flameless combustion mode.

## 6. References


[1] Markov, V. T., Inorganic Matter, (English Translation), Vol. 26, p. 64, 1980.

[2] Abrahamas, S. C., "The crystal and molecular structure of orthorhombic sulfur," Acta Crystallography, Vol. 8, p. 661, 1955.

# Separate Sensible and Latent Cooling with Solar Energy

**UMD Investigators: Reinhard Radermacher, Yunho Hwang**
**GRA: Ali Al-Alili**
**PI Investigator: Isoroku Kubo**
**Start Date: August 2007**

## 1. Objective/Abstract

The main objective of this project is to design, fabricate and test a solar cooling system with the highest possible cooling COP measured to date. The approach involves combining a very efficient concentrating PV-T collector with a separate sensible and latent cooling approach developed at CEEE. This solar cooling system is expected to operate under the UAE's harsh climate conditions.

## 2. Deliverables for the Completed Quarter

These are the accomplished tasks:

- Finished the construction of the ducts
- Finished connecting the separate ducts to each other
- Finished sealing the ducts from inside
- Installed the equipment into the ducts
- Finished the installation of fans
- Prepared insulation boards for the ducts

## 3. Summary of Project Activities for the Completed Quarter

The focus of this quarter was to construct the experiment setup. The construction of the main ducts was completed including the corners and connection pieces. The ducts were connected and sealed from the inside. The equipment and instruments were also mounted into the duct based on ASHRAE standards. In addition, the supply and exhaust fans were tested and installed.

### 3.1 Construction of the experimental setup

The supply, exhaust and conditioned space ducts were constructed during the last quarter. The construction was completed by constructing the corner pieces that connect the main three ducts. Once the ducts were connected together, the various equipment was assembled outside the chamber and then mounted inside the ducts. This equipment includes meshes, air mixers, heat exchangers, and vanes, as shown in Figures 1-4.

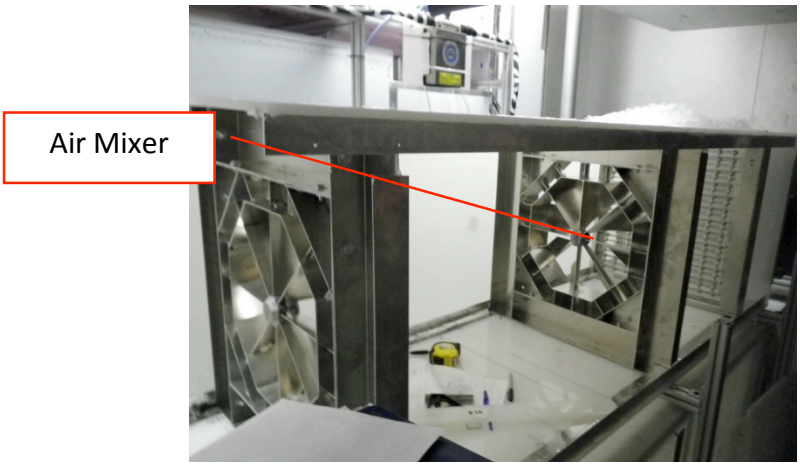


**Figure 1. Air mixers.**

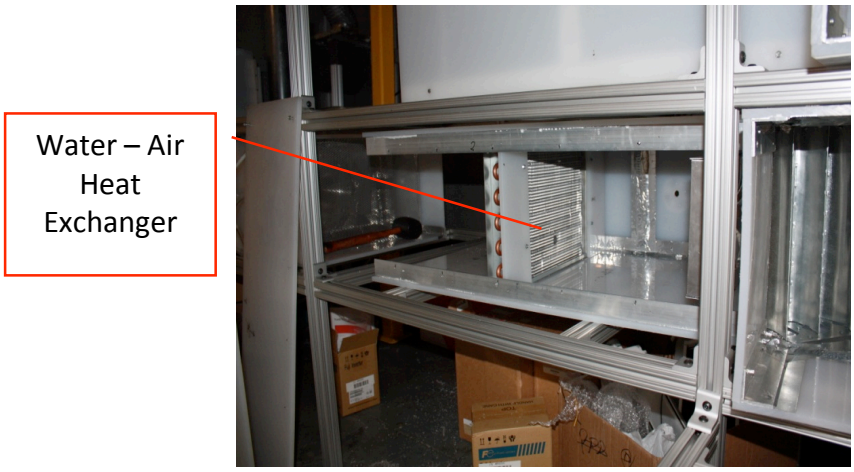


**Figure 2. Water-air heat exchanger.**

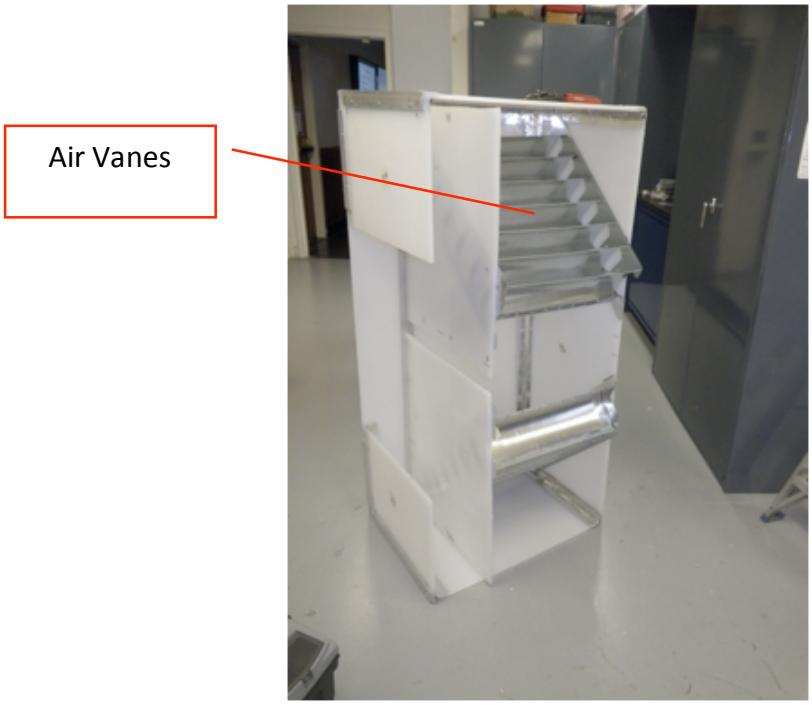


**Figure 3. Air vanes.**

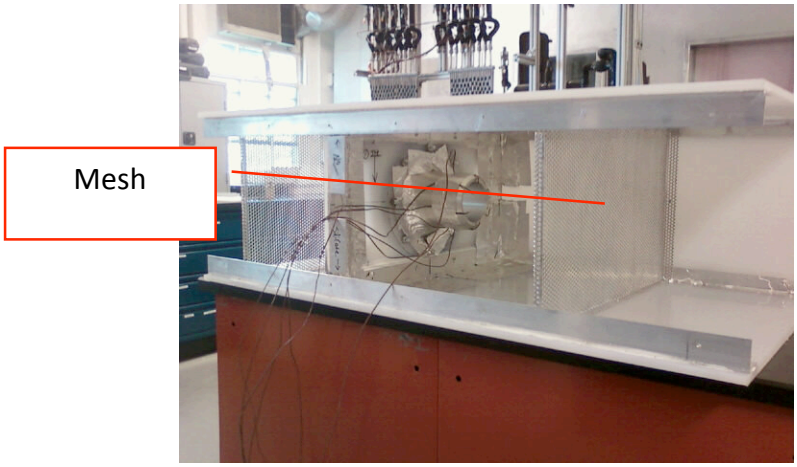


**Figure 4. Mesh.**

In addition, the instrumentation for mass, temperature and pressure measurements was prepared and mounted into the ducts. The instrumentation includes thermocouples, relative humidity sensors, nozzles and pressure transducers, as shown in Figures 6-9.

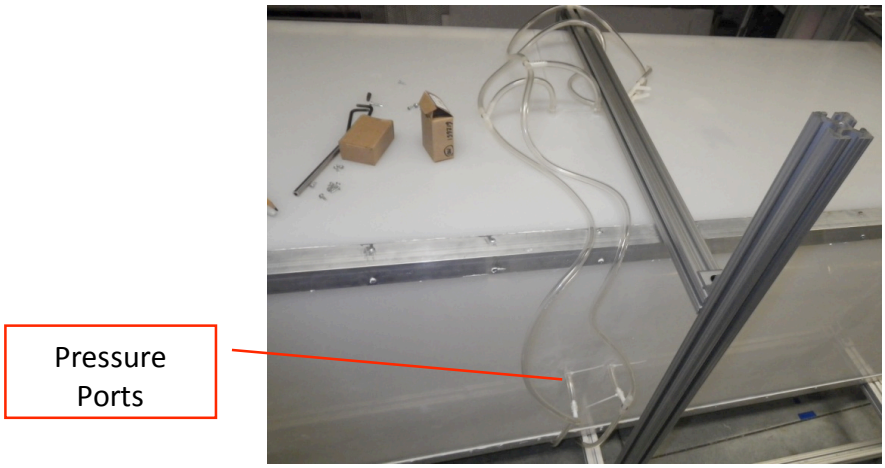


**Figure 6. Pressure ports.**

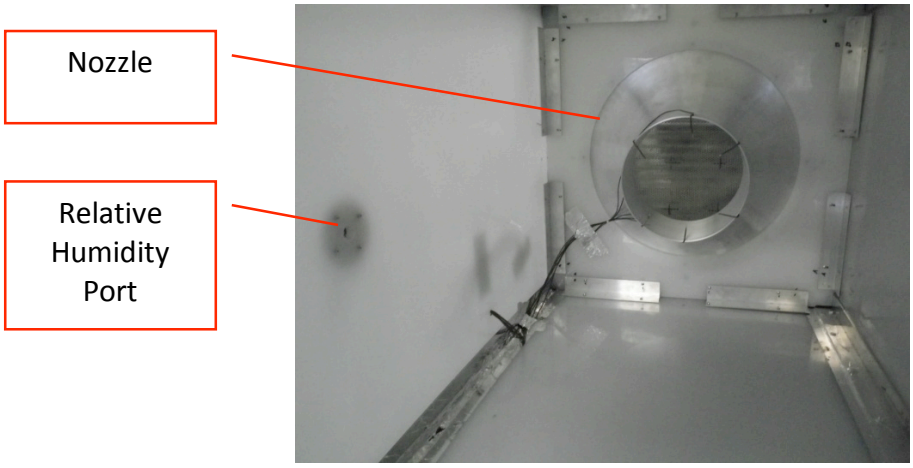


**Figure 7. Nozzle and relative humidity port.**

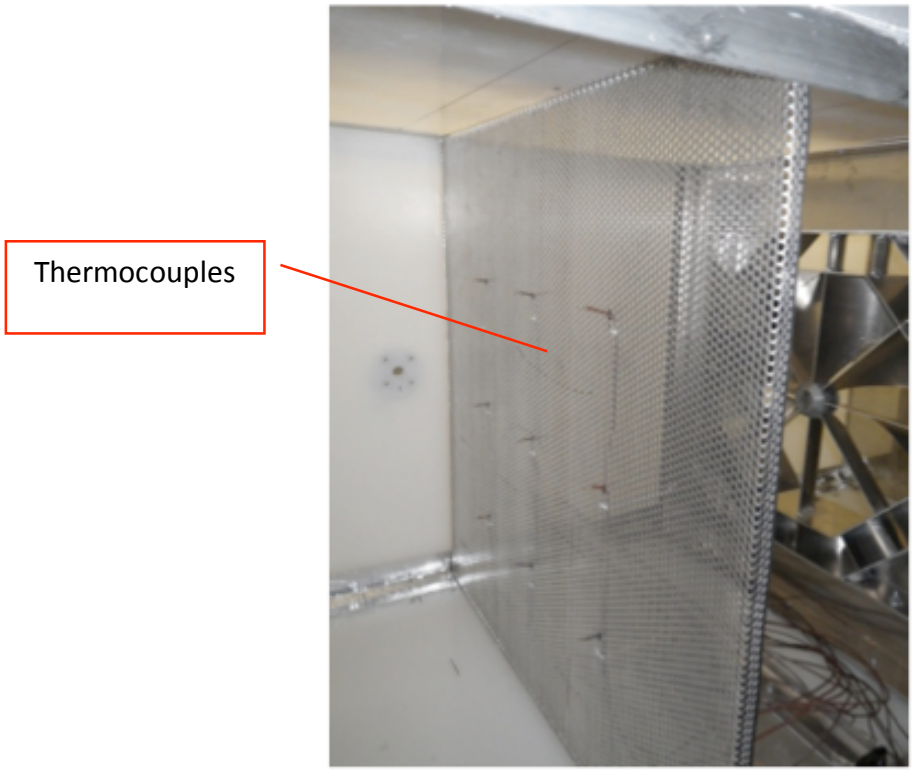


**Figure 7. Thermocouples.**

Figure 8 shows how the ducts are connected together.

**Figure 8. Ducts connected together.**

## 3.2 Fan installation

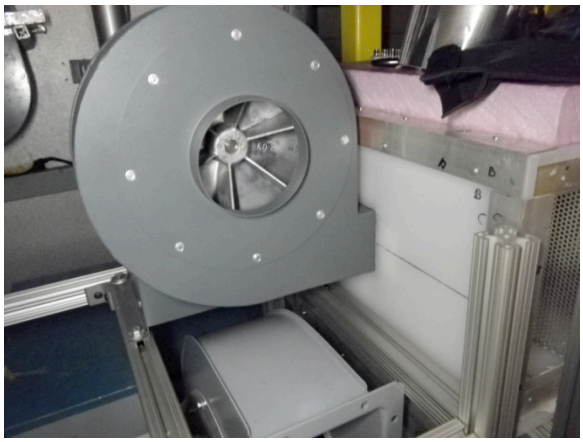

**Figure 9. Supply fan.**

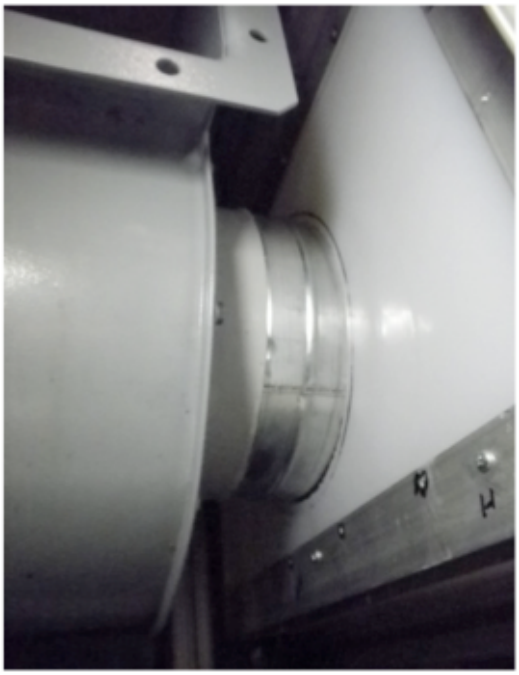

**Figure 10. Exhaust fan.**


**Figure 11. Conditioned space fan.**

## 4. Difficulties Encountered/Overcome

- Moving the ducts around the aluminum frame
- Available space inside the chamber
- Following ASHRAE standards was not simple due to the limited space available

## 5. Planned Project Activities for the Next Quarter

The following activities are to be conducted in the next quarter:

- Connect the experiment to the data acquisition card
- Finish the water loop
- Finish the refrigerant loop

## Appendix

### References


[1] Stine, W.B., Geyer, W.B., 2001, Power from the sun, www.powerfromthesun.net.
[2] Threlkeld,.J, Kuehn, T., Ramsy, J.,1998, Thermal Environmental Engineering, Prentice-Hall, Inc, USA
[3] http://www.nrel.gov/rredc/solar_data.html
[4] http://rredc.nrel.gov/solar/old_data/nsrdb/tmy2/State.html
[5] Notton , G. , Poggi, P. , Cristofari, C., 2006, Predicting hourly solar irradiations on inclined surfaces based on the horizontal measurements: Performances of the association of well-known mathematical models, *Energy Conversion and Management*, 47 1816–1829
[6] http://rredc.nrel.gov/solar/old_data/nsrdb/1991-2005/siteonthefly.cgi?id=724060
[7] ASHRAE, 1999, Applications Handbook, CH.32
[8] Kreith, F. and Kreider, J.F., 1978, Principles of solar engineering, *Hemisphere publishing corporation* Washington USA
[9] Kalogirou, S., 2004, Solar thermal collectors and applications, *Progress in Energy and Combustion Science* 30 pp. 231–295
[10] Goswami, Y., Kreith, F. and Kreider, J.F., 2000, Principles of solar engineering, *Taylor and Francis,* PA, USA,
[11] Duffie, J.A., Beckman, W.A., 1991, *Solar engineering of thermal processes*, Second edition, John Wiley & Sons, Inc., New York, ISBN: 0-471-51056-4.
[12] Pasupathy, A., Velraj, R., Seeniraj, R.V., 2008, Phase change material-based building architecture for thermal management in residential and commercial establishments, *Renewable and Sustainable Energy Reviews*, pp.39–64
[13] Dieng, A., Wang, R. , 2001 Literature Review on Solar Adsorption Technologies of Ice-making and Air Conditioning Purposes and Recent Developments in Solar Technology, *Renewable and Sustainable Energy Reviews* 5 pp.313–342
[14] Sumathy, K., Yeug, K, Yong, L., 2003, Technology Development in the Solar Adsorption Refrigeration Systems, *Progress in Energy and Combustion Science* 29 pp 301–327
[15] Roger, A. Messenger, J. V., 2005, Photovoltaic Systems Engineering, 2nd ed. Taylor & Francis
[16] http://www.nfpa.org/
[17] http://ieeexplore.ieee.org/iel5/7946/21930/01019771.pdf?arnumber=1019771
[18] TRANE, "Product Data: 4DCZ6036A through 4DCZ6060A" (2008), 22-1815-03
[19] METEONORM, "Global Meteorological Database for Engineers, Planners and Education,"(2007)

# Waste Heat Utilization in the Petroleum Industry

**UMD Investigators: Reinhard Radermacher, Yunho Hwang**
**GRAs: Amir Mortazavi, Abdullah Alabdulkarem**
**PI Investigators: Saleh Al Hashimi, Peter Rodgers**
**Start Date: October 2006**

## 1. Objective/Abstract

The main objective of this project is to minimize overall energy consumption of gas or oil processing plants with $CO_2$ capture and sequestration by utilizing waste heat and/or improving cycle design. Consideration will include the use of absorption chillers and steam cycles, among other options.

## 2. Deliverables for the Completed Quarter

The following were modeled using HYSYS software:

- Validated cascade $CO_2$ liquefaction cycle model
- Investigated the savings from cold $CO_2$ energy recovery in the APCI LNG plant and the $CO_2$ liquefaction cycle
- Compared this work optimized MCR refrigerant mixture versus optimized MCR refrigerant mixture in literature
- Optimized of all the configurations of gas turbine triple combined cycle with single pressure steam cycle configurations.

## 3. Summary of Project Activities for the Completed Quarter

HYSYS was used to model $CO_2$ liquefaction cycles captured from a flue gas of a gas-turbine based power plant. The developed model was validated against experimental data. The liquefied and pressurized $CO_2$ has cold energy in it. The recovery of this energy in the APCI LNG plant cycle and the $CO_2$ liquefaction cycle were investigated and the power savings were found to be of 3.02% and 5.12%, respectively. Further, the optimized MCR refrigerant mixture using HYSYS coupled by Matlab was compared with published literature on MCR refrigerant mixtures, which showed that the optimized mixture consumes less power than those in the literature.

Triple combined cycle with single pressure steam cycle configurations were optimized as an APCI LNG plant driver cycle. The best option, according to our models, consumes 36% less fuel than the baseline cycle.

### 3.1 $CO_2$ liquefaction and cycle validation

There is no $CO_2$ liquefaction cycle design available in the open literature. Thus, new designs were explored that are based on single-refrigerant as well as cascade configuration for liquefying the $CO_2$. Four common refrigerants were investigated. The refrigerants are $NH_3$, $CO_2$, propane and R134a.

An HYSYS model for cascade refrigeration system using $CO_2$ and $NH_3$ refrigerants was developed and validated against experimental data from Dopazo *et al* [1]. Dopazo *et al.*'s experiment is on 9 kW refrigeration capacity system at -50°C evaporation temperature. The $NH_3$ is the top vapor compression cycle (VCC) refrigerant, whereas the $CO_2$ is the bottom VCC refrigerant. Their experimental prototype and experiment schematic diagram are shown in Figures 1 and 2, respectively.

**Figure 1. Photograph of the experimental prototype of the cascade refrigeration system with $CO_2$ and $NH_3$ refrigerant [1].**

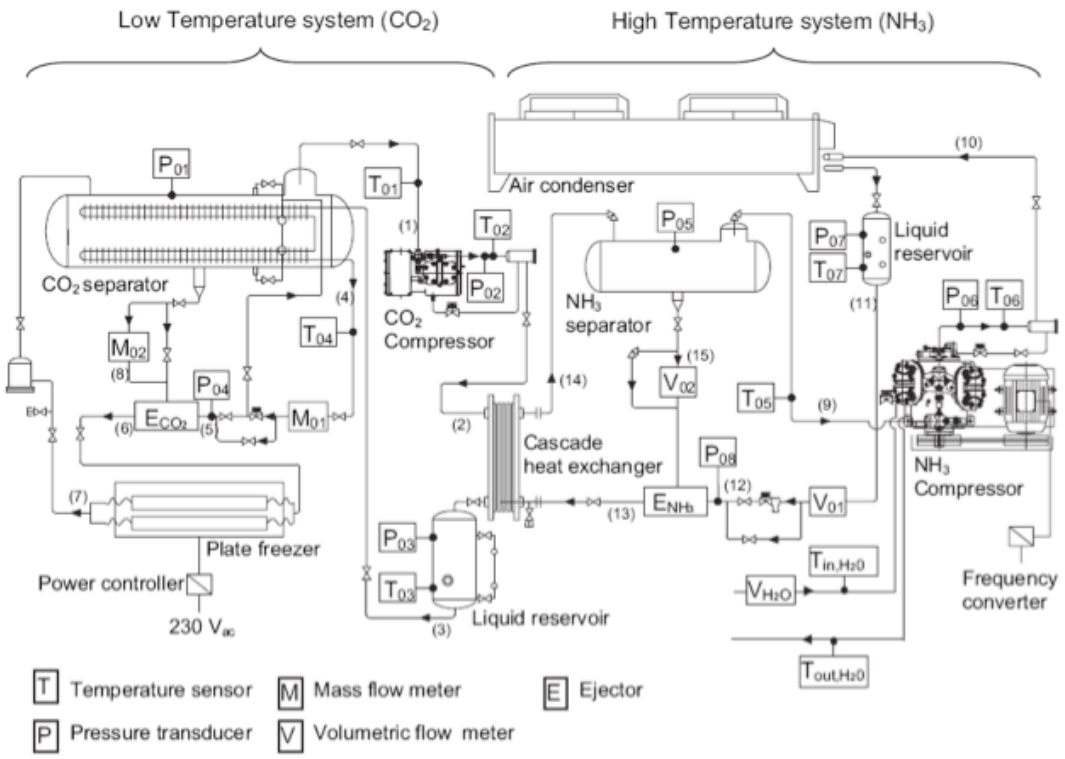


**Figure 2. Schematic diagram of the $CO_2/NH_3$ cascade refrigeration system [1].**

The developed HYSYS model that depicts Dopazo *et al.*'s prototype is shown in Figure 3. The model uses same operating parameters as the experiments. The equation of state used in this model is also the Peng-Robhinson equation of state that is used in all models in this work. The model has a cooling capacity of 9.45 kW at a cooling temperature of -50 C. The validation results, shown in Table 1, matched the experimental data pretty well for the top cycle ($NH_3$ VCC) as well as the bottom cycle ($CO_2$ VCC). The input parameters for the HYSYS model are the ones without discrepancy values in Table 1. The maximum discrepancy is in the calculated $NH_3$ refrigerant volume flow rate. This could be due to the accuracy of the equation of state in predicting the specific volume of the $NH_3$. However, the power consumption and the overall COP were predicted pretty well.

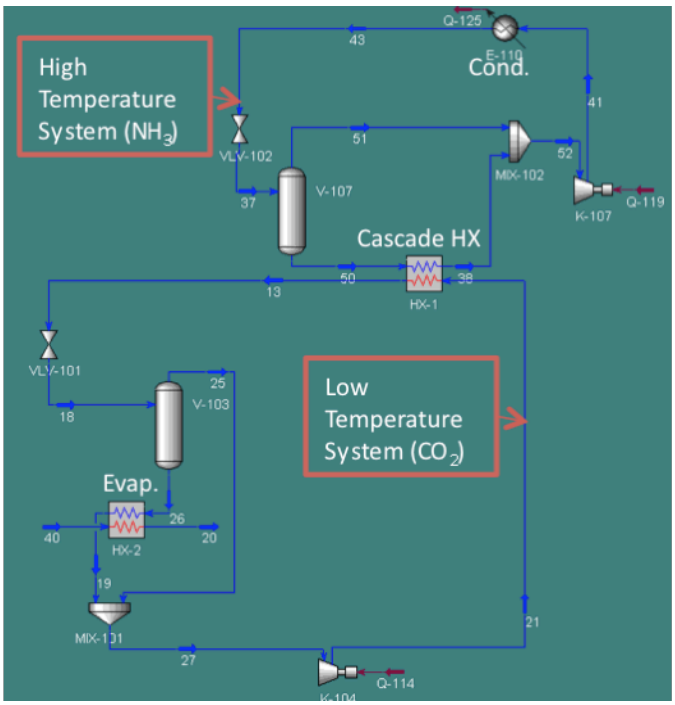


**Figure 3. HYSYS model for $CO_2/NH_3$ cascade refrigeration system that depicts Dopazo *et al.*'s experiment.**

**Table 1. Validation results from the Dopazo *et al.*'s experiment and HYSYS model for $CO_2/NH_3$ cascade refrigeration**

| VCC | Bottom ($CO_2$) | | | Top ($NH_3$) | | |
|---|---|---|---|---|---|---|
| Parameter | Measurement | HYSYS Model | Discrepancy | Measurement | HYSYS Model | Discrepancy |
| $T_{evap}$ (°C) | -50 | -50 | - | -20.96 | -20.96 | - |
| $T_{cond}$ (°C) | -17.48 | -17.48 | - | 29.72 | 29.72 | - |
| $P_{evap}$ (kPa) | 682 | 658.6 | 3.4 % | 182 | 179.5 | 1.4 % |
| $P_{cond}$ (kPa) | 2127 | 2127 | - | 1158 | 1158 | - |
| $\Delta T_{sh}$ | 15 | 14.94 | 0.4 (°C) | 15 | 15.02 | -0.02 (°C) |
| $\Delta T_{sc}$ | 0.34 | 0.54 | 0.2 (°C) | 4.74 | 0.29 | -4.5 (°C) |
| $Q_{evap}$ (kW) | 9.45 | 9.45 | - | 13.5 | 12.55 | 7 % |
| $Q_{cond}$ (kW) | 13.2 | 12.55 | 4.9 % | 17.2 | 18.03 | -4.8 % |
| $W_{ele}$ (kW) | 3.93 | 3.67 | 6.6 % | 6.32 | 6.68 | -5.8 % |
| Comp. isen. eff. (%) | 57.9 | 57.9 | - | 58.8 | 58.8 | - |
| Ref. flow | 124.4 (kg/h) | 118.1 (kg/h) | 5.1 % | 1.28 L/m | 1.12 L/m | 12.5 % |
| COP | 2.4 | 2.57 | -7.3 % | 2.14 | 1.87 | 12.3 % |
| Total | $CO_2/NH_3$ | | | | | |
| $\Delta T_{cascade}$ (C) | 3.48 | 3.48 | - | | | |
| COP $CO_2/NH_3$ | 0.92 | 0.91 | 0.83 % | | | |

### 3.2 Modeling with waste heat recovery

In this section, some of the waste heat sources and uses that were proposed in Figure 3 are modeled.

#### 3.2.1 Single-refrigerant $CO_2$ liquefaction cycles with cold $CO_2$ recovery in APCI cycle

The propane cycle in the APCI LNG plant precools the natural gas and subcools the MCR from 40 C to -30 ºC in five heat exchangers. Each heat exchanger has a propane evaporation temperature. The proposed idea of using the cold $CO_2$ in natural gas liquefaction and MCR subcooling was investigated and modeled using HYSYS software as shown in Figure 4.

The basic idea is that the cold $CO_2$ (at -48 C) will reduce the cooling load of the propane cycle. The resulting reduction in power consumption is 1.32 MW, or 3.02%. The reason this reduction is not big is because the flow rate of the $CO_2$ is very small compared to the mass flow rate of the propane (mass flow ratio is 7.32%).

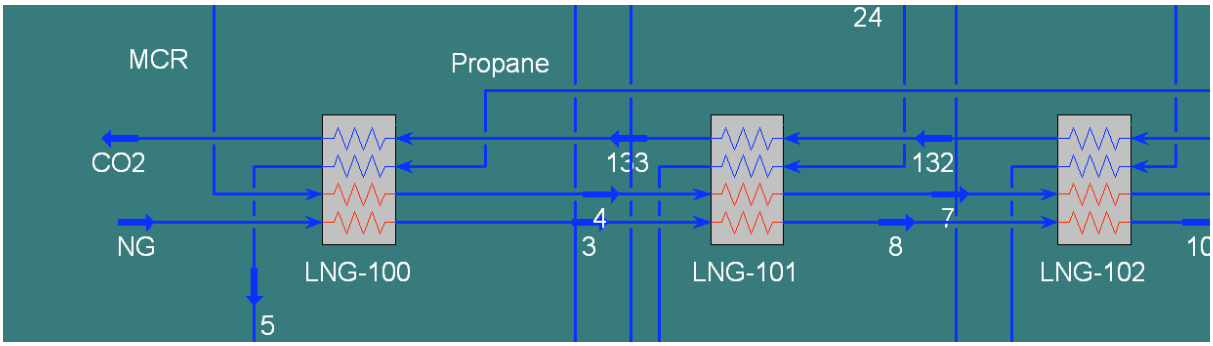


**Figure 4. APCI LNG plant integration with the cold $CO_2$. Three out of five heat exchangers are in the APCI LNG plant.**

### 3.2.2 Using cold $CO_2$ for cooling the $CO_2$ and refrigerant

#### 3.2.2.1 Single-refrigerant $CO_2$ liquefaction cycles with cold $CO_2$ recovery in $CO_2$ liquefaction cycle

The proposed idea of using the cold $CO_2$ to subcool the refrigerant after the condenser and to precool the $CO_2$ before liquefaction was also investigated and modeled using HYSYS software as shown in Figure 5. As stated earlier, the available cooling capacity in the liquefied $CO_2$ at 6 bar liquefaction pressure is 3.69 MW. Subcooling the refrigerant using the cold $CO_2$ will make the refrigerant cooler than 40 C after the refrigerant condenser and before its expansion valve. Therefore, lower refrigerant quality or more cooling capacity is available for liquefying the $CO_2$.

A precooling heat exchanger for the $CO_2/H_2O$ stream using the cold $CO_2$ is introduced as shown in Figure 5. Thus, lower cooling load is required from the VCC.

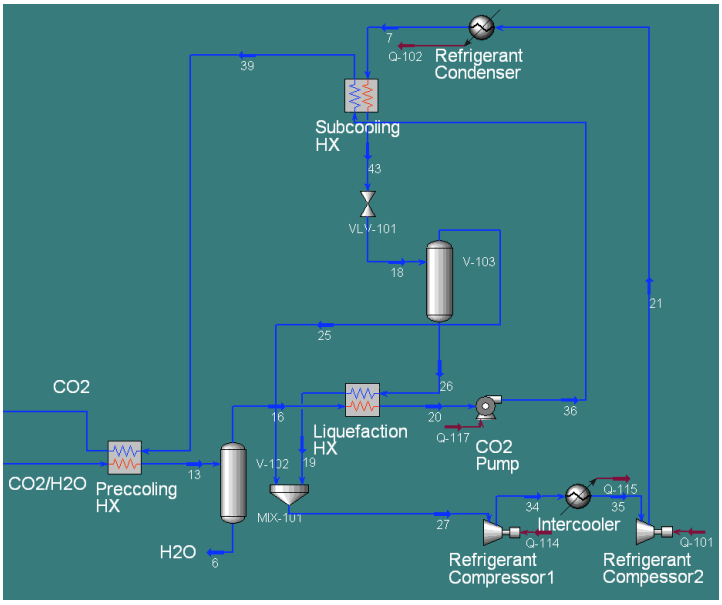


**Figure 5. Single-refrigerant $CO_2$ liquefaction cycle with cold $CO_2$ recovery.**

The P-h diagram for ammonia refrigerant with cold $CO_2$ recovery at 6 bar liquefaction pressure is shown in Figure 6. In comparison to the cycle without cold $CO_2$ recovery, the subcooling temperature is -10°C instead of 40°C. Further, the VCC cooling load is 7.23 MW instead of 9.01

MW. The resulting VCC power consumption is 4.39 MW, which is 30.75% less than the cycle without cold $CO_2$ recovery.

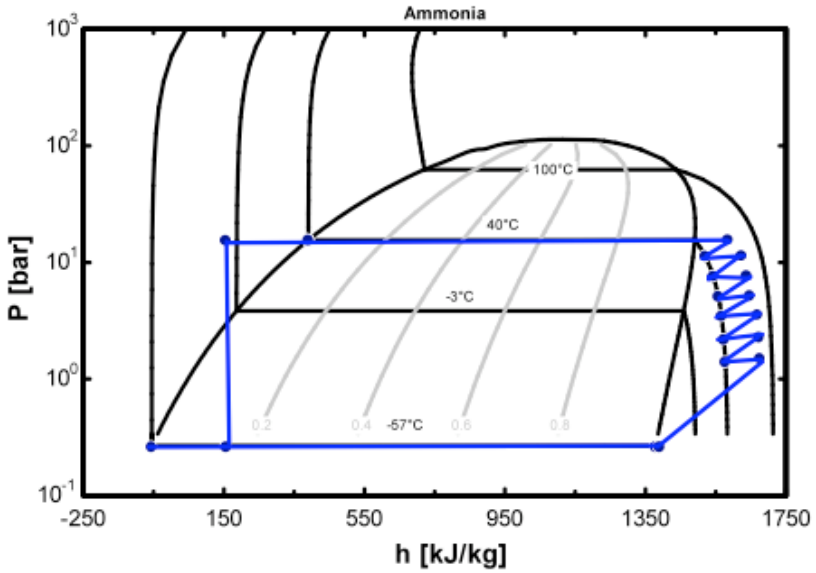


**Figure 6. P-h diagram for ammonia in single-refrigerant $CO_2$ liquefaction cycle at 6 bar with cold $CO_2$ recovery.**

Since liquefaction pressure affects liquefaction load and $CO_2$ compressor power, eight liquefaction cycles with cold $CO_2$ recovery with different refrigerants at randomly chosen liquefaction pressure were modeled using HYSYS software. The results, Table 2, show that the least total power consumption is at 50 bar liquefaction pressure using ammonia refrigerant. Moreover, Table 2 shows that at different liquefaction pressures, different refrigerants other than ammonia can be used with close power consumption.

In comparison to $CO_2$ compression only (conventional configuration), the savings in power consumption for the ammonia cycle at 50 bar is 5.12%. On the other hand, the savings against ammonia liquefaction cycle at 6 bar liquefaction pressure without cold $CO_2$ energy recovery is 31.44%.

**Table 2. Results from HYSYS models for different $CO_2$ liquefaction cycles**

| Refrigerant | R134a | $NH_3$ | $NH_3$ | $NH_3$ | R134a | $CO_2$ | Propane | $NH_3$ |
|---|---|---|---|---|---|---|---|---|
| Liquefaction Press. (bar) | 30 | 30 | 6 | 70 | 70 | 70 | 70 | 50 |
| Pump (MW) | 0.34 | 0.34 | 0.34 | 0.38 | 0.38 | 0.38 | 0.38 | 0.33 |
| VCC Power ( MW) | 1.43 | 1.37 | 4.39 | 0.15 | 0.15 | 0.6 | 0.16 | 0.59 |
| $CO_2$ Comp. Power (MW) | 4.36 | 4.36 | 1.98 | 5.44 | 5.44 | 5.44 | 5.44 | 5.01 |
| Total Power (MW) | 6.13 | 6.06 | 6.72 | 5.97 | 5.98 | 6.42 | 5.99 | 5.93 |

### 3.3 Optimized MCR refrigerant mixture versus optimized MCR refrigerant mixture in literature

Venkatarathnam [2] and Paradowski *et al.* [3] have published their optimized refrigerant mixtures for an MCR cycle in an APCI LNG plant. They did not use GA methods to obtain their refrigerant mixtures compositions. Venkatarathnam and Paradowski used similar NG feed, shown in Table 3, which is different than this work NG gas feed.

**Table 3. Gas composition used in Venkatarathnam [2] and Paradowski *et al.* [3] models**

| Component | Mole Fraction (%) |
|---|---|
| Nitrogen | 4 |
| Methane | 87.5 |
| Ethane | 5.5 |
| Propane | 2.1 |
| i-Butane | 0.3 |
| n- Butane | 0.5 |
| i-Pentane | 0.1 |

In order to compare our optimization approach against the optimization approach of Venkatarathnam and Paradowski *et al.*, the MCR optimization was done with NG feed, pre-cooling temperature and liquefaction temperature similar to what Venkatarathnam and Paradowski *et al.* used. The resulting optimized MCR cycle is shown in Table 4.

Two models were developed in HYSYS that use refrigerant mixtures discussed by Venkatarathnam and Paradowski *et al.*, which are then optimized for the same objective function, variables (except the refrigerant mixture composition), and constraints. The optimized power consumption for the models in HYSYS that used refrigerant mixtures discussed by Venkatarathnam and Paradowski *et al.* was 6.98% and 13.6% higher than the optimized power consumption of this work, as shown in Figure 7. Their LMTDs for the two sections in SWHX are also higher than the optimized cycle LMTDs, as shown in Table 4. This shows the superiority of the refrigerant mixture composition obtained with GA over the mixtures obtained by other methods.

**Table 4. Comparison between this work results and results from the optimized HYSYS models that use refrigerant mixtures optimized by Venkatarathnam and Paradowski *et al.***

| Cycle | Variables | | | | | | | | Objective function | LMTDs (K) |
|---|---|---|---|---|---|---|---|---|---|---|
| | , □. (kg/s) | $x_{N2}$ | $x_{C1}$ | $x_{C2}$ | $x_{C3}$ | $P_i$ (kPa) | $P_H$ (kPa) | $P_{Ex}$ (kPa) | MCR Power Cons. (MW) | |
| This work optimized, TP≥3 K | 232.8 | 0.0731 | 0.2506 | 0.5291 | 0.1472 | 2259 | 3967 | 511 | 51.67 | 5.55/5.9 |
| Venkatarathnam Optimized, TP≥3 K | 217.97 | 0.0725 | 0.2479 | 0.3324 | 0.3472 | 2900 | 4665 | 337 | 58.7 (13.6% More power consumption) | 6.14/12.24 |
| Paradowski *et al.* Optimized, TP≥3 K | 222.11 | 0.0488 | 0.2701 | 0.4422 | 0.2389 | 2284 | 4446 | 420 | 55.28 (6.98% More power consumption) | 7.99/6.04 |

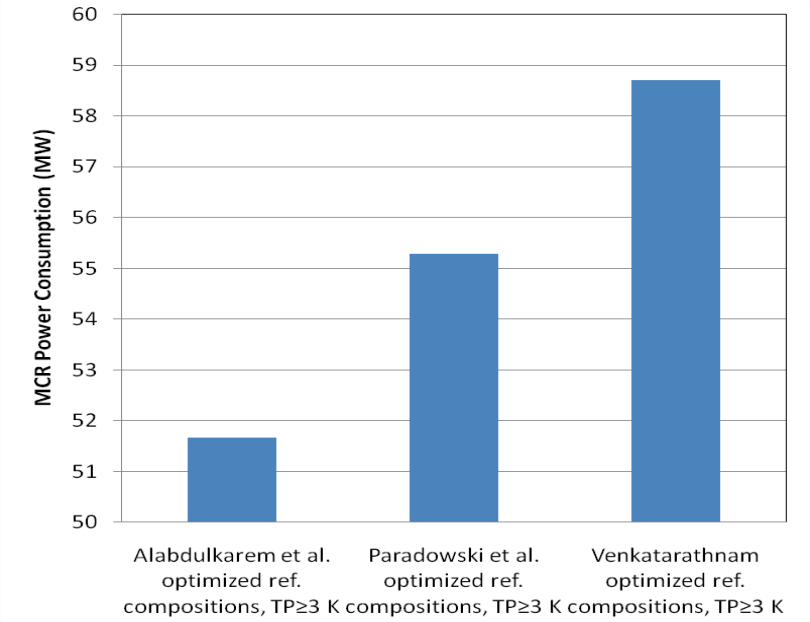


**Figure 7. Optimized MCR power consumption that this work optimized refrigerant mixtures against the optimized refrigerant mixtures of Venkatarathnam and Paradowski, *et al.***

## 3.2 Optimization of different gas turbine triple combined cycle configurations:

In order to investigate the potential of gas turbine, steam and absorption chiller combined cycles as an APCI LNG plant driver, the performance of the driver system should be optimized. Moreover, to fully appreciate the benefits of this system it should be compared to the optimized conventional technologies. Matlab software was used as an optimization tool. It was connected to HYSYS, which was used to model the driver cycles. Six different configurations of the triple combined cycle were considered:

1. Triple cycle gas turbine single pressure steam with double effect absorption chiller combined cycle
2. Triple cycle gas turbine single pressure steam with single effect absorption chiller combined cycle
3. Split design triple cycle gas turbine single pressure steam with double effect absorption chiller combined cycle
4. Split design triple cycle gas turbine single pressure steam with single effect absorption chiller combined cycle
5. Triple cycle with double effect absorption chiller with auxiliary burner
6. Triple cycle with single effect absorption chiller auxiliary burner.

The HYSYS model of the normal triple cycle, the split design and triple cycle with auxiliary burner are shown in Figures 8, 9 and 10 respectively. The comparison of different driver technologies is shown in Table 5. As is shown in Table 5, the most efficient driver configuration was the gas turbine single pressure steam and single effect water Li/Br absorption chiller triple combined cycle, which has the least fuel consumption. Moreover, this driver configuration maintained its advantages by varying the steam turbine efficiency and minimum exhaust temperature. Its efficiency was 36% and 3% higher than convention gas turbines and gas turbine and steam combined cycle drivers, respectively. Moreover as shown in Table 3, the cycles with auxiliary burner were not more efficient than the normal cycles, since optimization results showed zero fuel mess flow rate to the burner. Hence, at best they have the same efficiency as the corresponding normal triple cycle.

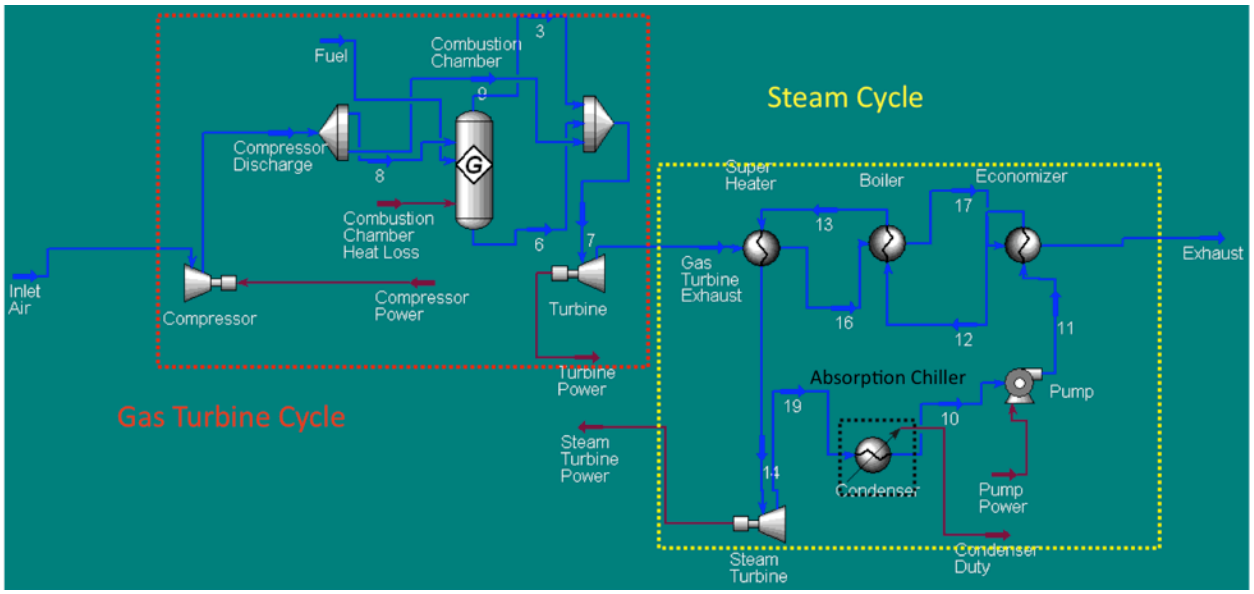


**Figure 8. Hysys model of triple combined cycle.**

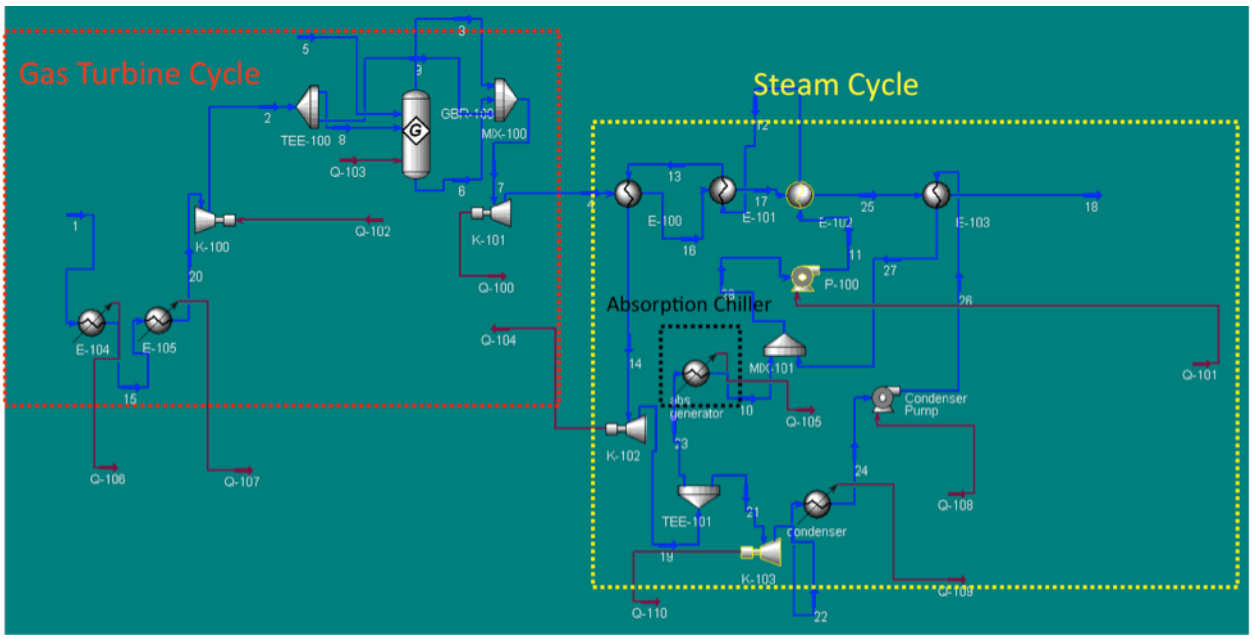


**Figure 9. Hysys model of split design triple combined cycle.**

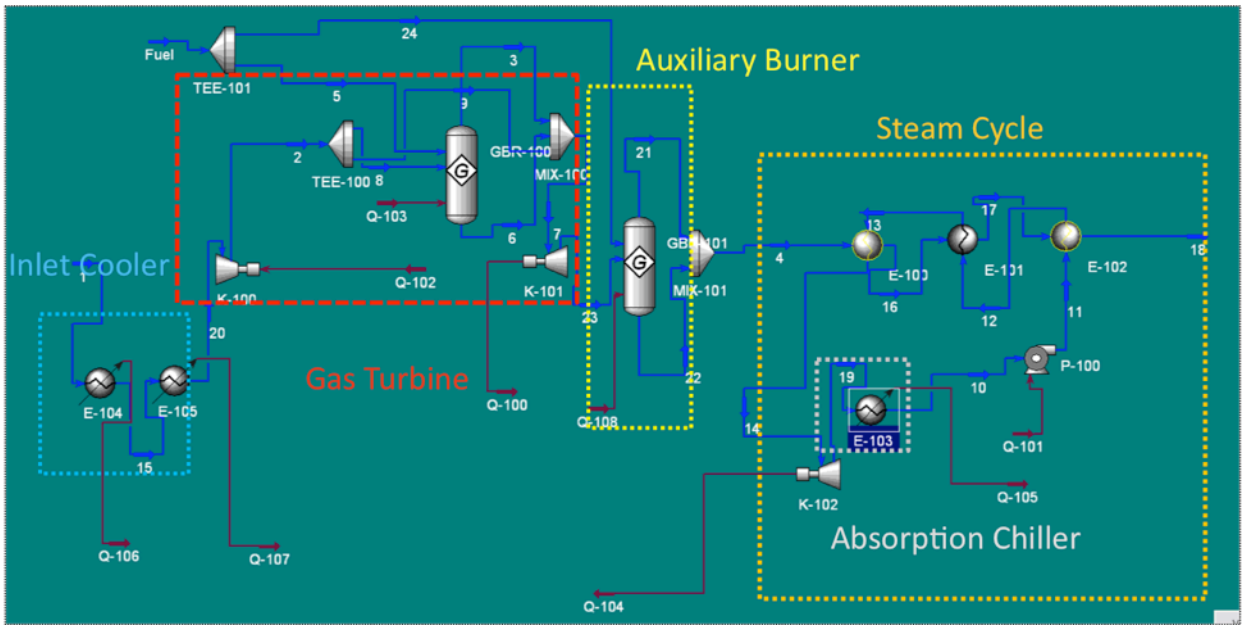


**Figure 10. Hysys model of triple combined cycle with auxiliary burner.**

**Table 5. Comparison of different driver cycle technologies**

| | | | | | | | | | |
|---|---|---|---|---|---|---|---|---|---|
| Steam Turbine Efficiency (%) | 86 | 90 | 90 | 86 | 90 | 90 | 86 | 90 | 90 |
| Exhaust Temperature ( °C ) | 180 | 180 | 110 | 180 | 180 | 110 | 180 | 180 | 110 |
| **Cycle** | **Fuel Consumption (kg/s)** | | | **Efficiency (%)** | | | **Efficiency Enhancement (%)** | | |
| Base Cycle With Gas Turbine as a Driver | 6.575 | 6.575 | 6.575 | 33.52 | 33.52 | 33.52 | --- | --- | --- |
| Combined Gas turbine and Double effect Absorption Chiller | 5.174 | 5.174 | 5.174 | 42.59 | 42.59 | 42.59 | 21.31 | 21.31 | 21.31 |
| Combined Gas Turbine and Single Pressure Steam Cycle | 4.571 | 4.541 | 4.407 | 48.21 | 48.53 | 50.00 | 30.48 | 30.93 | 32.98 |
| Triple Cycle with Double Effect Absorption Chiller | 4.704 | 4.641 | 4.641 | 46.85 | 47.48 | 47.48 | 28.46 | 29.41 | 29.41 |
| Triple Cycle with Single Effect Absorption Chiller | 4.251 | 4.235 | 4.219 | 51.84 | 52.03 | 52.23 | 35.35 | 35.59 | 35.84 |
| Split Design Triple Cycle with Double Effect Absorption Chiller | 4.581 | 4.556 | 4.556 | 48.10 | 48.37 | 48.37 | 30.33 | 30.71 | 30.71 |
| Split Design Triple Cycle with Single Effect Absorption Chiller | 4.594 | 4.585 | 4.556 | 47.97 | 48.06 | 48.37 | 30.13 | 30.27 | 30.71 |
| Triple Cycle with Double Effect Absorption Chiller with auxiliary burner | 4.704 | 4.641 | 4.641 | 46.85 | 47.48 | 47.48 | 28.46 | 29.41 | 29.41 |
| Triple Cycle with Single Effect Absorption Chiller auxiliary burner | 4.251 | 4.235 | 4.219 | 51.84 | 52.03 | 52.23 | 35.35 | 35.59 | 35.84 |

## 4. Difficulties Encountered/Overcome

None.

## 5. Planned Project Activities for the Next Quarter

The following activities are to be conducted in the next quarter:

- Validate cascade cycle
- Evaluate the overall system performance
- Optimize the gas turbine, dual pressure steam and absorption chiller triple combined cycle as a driver of the APCI LNG plant.

## Appendix

### Justification and Background

Waste heat utilization opportunities are abundant in the oil and gas industry. Proper use of waste heat could result in improved cycle efficiency, reduced energy usage, reduction in $CO_2$ emissions, and increased production capacity.

CEEE at the University of Maryland has extensive experience in the design and implementation of integrated combined cooling, heating, and power (CCHP) projects. The faculty at PI has experience in the design and operation of petroleum processing plants. Jointly the team is well equipped to address the challenge posed by this project.

### References


[1] Dopazo J. A., and Fernández-Seara J., 2010, "Experimental evaluation of a cascade refrigeration system prototype with $CO_2$ and $NH_3$ for freezing process applications," International Journal of Refrigeration, pp. 1-11.

[2] Venkatarathnam G., 2008, Cryogenic Mixed Refrigerant Processes, Springer-Verlag New York, LLC,.

[3] Paradowski H., Bamba M. O., and Bladanet C., 2004, "Propane Precooling Cycles for Increased LNG Train Capacity," 14th International Conference and Exhibition on Liquefied Natural Gas, pp. 1-18.

[4] Alefeld, G., Radermacher, R., 1994, "Heat conversion systems", CRC Press, Boca Raton.

[5] Al-Hamdan, Q.Z., Ebaid, M.S.Y., 2006, "Modeling and simulation of a gas turbine engine for power generation", ASME Journal of Engineering for Gas Turbines and Power, Vol. 128, pp. 302-311.

[6] LNG technology selection, http://www.fwc.com/publications/tech_papers/files/TariqLNG.pdf, Last access, June, 2008

[7] Haring, H., 2008, " Industrial Gas Processing", Wiley-VCH, Weinheim

[8] ASHRAE, 2002, "ASHRAE Refrigeration Handbook", American Society of Heating, Refrigeration and Air-Conditioning Engineers, Atlanta, GA, USA.

[9] ASHRAE, 2005, "ASHRAE Fundamentals Handbook", American Society of Heating, Refrigeration and Air-Conditioning Engineers, Atlanta, GA, USA.

[10] Brant, B., Brueske, S., Erickson, D.C., Papar, R., 1998, "New waste-heat refrigeration unit cuts flaring, reduces pollution", Oil & Gas Journal, May 18, pp.61-64.

[11] Brooks, F.,J., 2000 "GE gas turbine performance characteristics", GE Power Systems Schenectady, NY, GER-3567H.

[12] Cohen, H., Rogers, G.F.C., Saravanamuttoo, H.I.H., 1996, "Gas turbine theory", 4th edition, Longman Scientific & Technical, Singapore.

[13] Erickson, D.C., 2000 "LPG recovery from reformer treat gas", US Patent 6,158,241.

[14] Erickson, D.C., Anand, G., Papar, R.A., Tang, J., 1998, "Refinery waste heat powered absorption refrigeration – cycle specification and design", Proceeding of the ASME Advanced Energy System Division, AES-Vol. 38, pp.391-402.

[15] Erickson, D.C., Kelly, F., 1998, "LPG recovery from refinery by waste heat powered absorption refrigeration", IECEC-98-079, 33rd Intersociety Engineering Conference on Energy Conversion, Colorado Springs, CO.

[16] Giampaolo, T., 2003, "The gas turbine handbook: principles and practices", 2nd edition, The Fairmont Press, Lilburn, GA.

[17] Herold, K.E.; Radermacher, R., Klein, S, 1996, "Absorption chillers and heat pumps", CRC Press, Boca Raton.

[18] Kim, T.S., Hwang, S.H., 2006, "Part load performance analysis of recuperated gas turbine considering engine configuration and operation strategy", Energy, Vol. 31, pp., 260-277.

[19] Klein, S.A., 2005, "Engineering Equation Solver" F-Chart Software.

[20] Kurz, R., 2005, “Gas turbine performance”, 44th Turbomachinery Symposium, pp.131-146.
[21] Kurzke, J., 2003, “Model based gas turbine parameter corrections”, GT2003-38234, Proceedings of 2003 ASME TURBO EXPO: Power for Land, Sea, & Air, Atlanta, GA, USA.
[22] Li, Y.G., Pilidis, P., Newby, M.A., 2006, “An adaptation approach for gas turbine design-point performance simulation”, Journal of Engineering for Gas Turbines and Power, Vol. 128, pp. 789-795.
[23] Orlando, J. A., 1996, “Cogeneration design guide”, American Society of Heating, Refrigeration and Air-Conditioning Engineers, Atlanta, GA.
[24] Pande, M., 1996, “Tools for fractionator design in ammonia-water absorption machines”, Master Thesis, University of Maryland, College Park.
[25] Walsh, P.P., Fletcher, P., 1998, “Gas turbine performance”, Blackwell Science, Oxford.

# Thrust 2
# Energy-Efficient Transport Processes

# Multidisciplinary Design and Characterization of Polymer Composite Seawater Heat Exchanger Module

**PI Investigator: Peter Rodgers**
**UMD Investigators: Avram Bar-Cohen, Satyandra K. Gupta, David Bigio, H.A. Bruck**
**GRAs: Juan Cevallos, F. Robinson, T. Hall, W. Pappas, P.K. Hadfield**
**Start Date: Oct 2006**

## 1. Introduction

Heat exchangers are extensively used in all oil and gas processing operations with seawater as the preferred coolant in near-shore operations. The performance and cost effectiveness of conventional metallic heat exchangers in such environments are severely constrained by corrosion and scale deposits. Polymer heat exchangers, currently under investigation by the EERC team, offer a promising alternative to metallic heat exchangers for the fossil fuel industry. Recent advances in carbon-fiber polymer composites, yielding polymer materials with thermal conductivities equal to or higher than titanium, can be applied to the development of low-cost and low-weight compact heat exchangers for corrosive fluids. These attributes, combined with the low energy investment in the formation and fabrication of these polymer heat exchangers and their ease of manufacturing, appear to make near-term applications of seawater polymer heat exchangers viable. Numerical simulations and laboratory experiments, performed by the UMD/PI EERC team in the first phase of this research, strongly support these conclusions.

## 2. Deliverables

I. Investigate the effective thermal conductivity of a PA12-carbon fiber composite used in an injection-molded prototype heat exchanger (Task A2)
II. Develop a discretized, mapped-meshed finite element model using hygrothermally aged mechanical properties to assess feasibility of replacing metallic heat exchangers at the Das Island liquefied natural gas facility with polymer composite heat exchangers (Task A2)
III. Assess feasibility of modeling orthotropic heat exchanger module as an isotropic model with averaged properties (Task A2)
IV. Two technical poster presentations entitled, “Saltwater Hygrothermal Aging Studies of Short Carbon Fiber Reinforced Polyamide 12,” given at the 2010 ASME International Mechanical Engineering Congress & Exposition [1] (Task A5)
V. Refine model simplification guidelines and techniques for mold filling metamodel of Plate-Fin polymer heat exchangers (Task B1)
VI. Develop new datapoint selection methodology for improving the accuracy of the mold-filling statistical metamodel (Task B1)
VII. Develop a technique for characterizing mixing of polymer composites in a Twin Screw Extruder (Task C1)

## 3. Summary of Project Activities for the Completed Quarter

### *I. Investigate the effective thermal conductivity of a PA12-carbon fiber composite used in an injection-molded prototype heat exchanger*

- Experimental results of a prototype polymer heat exchanger were used for an inverse determination of the effective thermal conductivity of the polymer composite. The listed in-plane thermal conductivity of the PA12 composite is 10 W/m·K. However, due to processing-induced anisotropy, the effective thermal conductivity can be up to an order-of-magnitude lower than the in-plane conductivity.
- Data was collected using the experimental apparatus described in previous reports for a crossflow thermally enhanced polymer heat exchanger. Bulk inlet and outlet temperatures were measured for both fluids, as well as their corresponding mass flow rates.
- The inlet air temperature was 50 °C, while the inlet water temperature was 15 °C. The air flow rate was varied between 1000 and 3000 $cm^3/s$, while the water temperature was held at a constant 60 $cm^3/s$.
- For these conditions, the air temperature drop ranged from ~6 °C when the flow rate was 1000 $cm^3/s$, down to ~4 °C when the flow rate was 3000 $cm^3/s$. Meanwhile, the temperature rise in the water was negligible due to the relatively low heat transfer rate.
- The heat transfer rate of this crossflow PHX is shown in Figure 1. The experimental results were calculated using the air-side energy balance equation $q = mC_p\Delta T$, assuming steady state. The analytical results were calculated using the e-NTU equations with three assumed values of thermal conductivity ($k$ = 0.25, 1, 4 W/m·K). The measurement uncertainty was calculated to be 16%, and comparison of experimental and analytical results revealed than an effective thermal conductivity could be between 1 and 4 W/m·K, given the uncertainty shown by error bars in the graph.

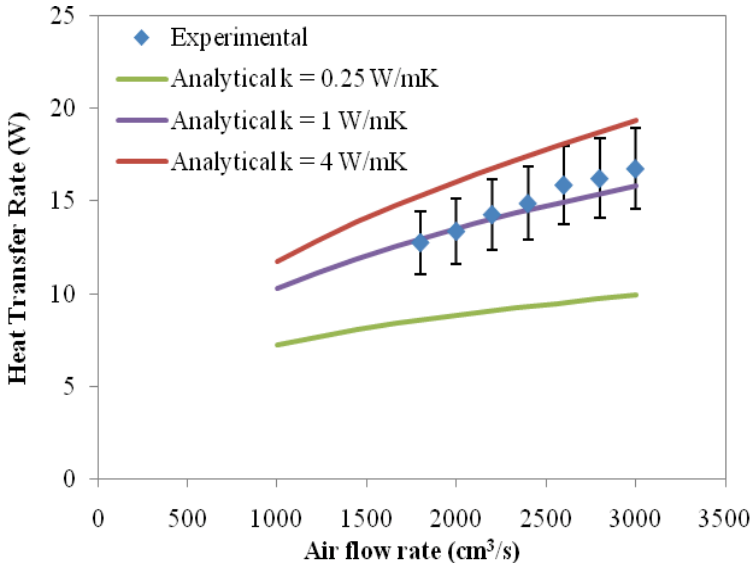


**Figure 1. Heat transfer rate as a function of air flow rate.**

**($T_{air,i}$ = 50 °C, $DT_{air}$ = 5 - 6 ° C, $\dot{V}_{water}$ = 60 $cm^3/s$, $T_{water,i}$ = 15 ° C)**

- Using the calculated heat transfer rate, the thermal conductance UA of the heat exchanger was calculated using the equation $q = UA \cdot \Delta T_{lm}$. The measurement uncertainty was propagated further due to the additional uncertainty in the log-mean

temperature difference $\Delta T_{lm}$. The resulting relative uncertainty in the overall thermal conductance was 29%.

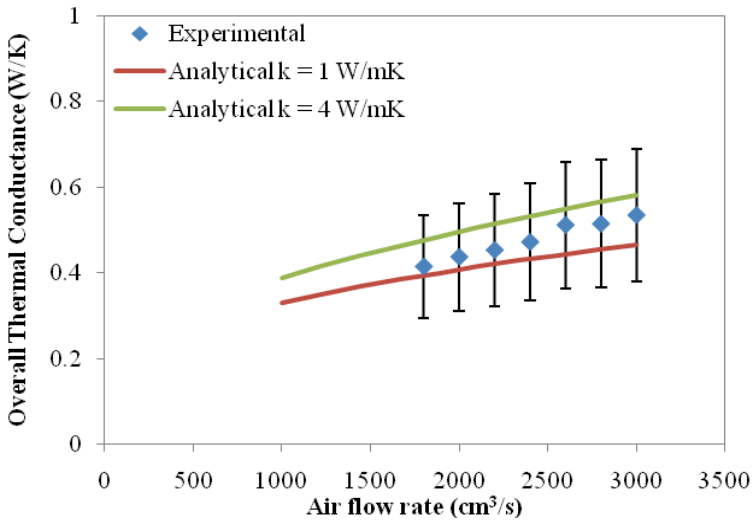


**Figure 2. Overall thermal conductance as a function of air flow rate.**

**($T_{air,i}$ = 50 °C, $DT_{air}$ = 5 - 6 ° C, $\dot{V}_{water}$ = 60 cm³/s, $T_{water,i}$ = 15 ° C)**

- Due to the large uncertainty in UA, an accurate inverse determination of an effective thermal conductivity is difficult to accomplish. The error bars in Figure 2 prove that a wide range of values of thermal conductivity can provide a good fit between analytical and experimental results, given the large relative uncertainty.
- Careful observation of the analytical model for the overall HX thermal conductance, shown below, reveals that the relatively low heat transfer coefficient makes the air-side convective thermal resistance the dominant resistance. For an inverse determination of thermal conductivity, ideally the convective resistances are negligible when compared to the wall thermal resistance.

$$UA = \frac{1}{\frac{1}{(\eta_o h A)_h} + \frac{t}{k_w A_w} + \frac{1}{(hA)_c}}$$

- Further experiments with higher inlet temperatures (120 °C) and flow rates (13,000 cm³/s) will increase the heat transfer rate and reduce the relative uncertainty. A lower relative uncertainty is possible due to higher temperature drops. Additionally, with higher heat transfer coefficients, an inverse determination of *k* will become feasible. Finally, higher heat transfer rates will cause the temperature rise in the water to become appreciable, allowing for a heat balance on the HX.

***II. Develop discretized, mapped-meshed finite element model using hygrothermally aged mechanical properties to assess feasibility of replacing metallic heat exchangers at the Das Island liquefied natural gas facility with polymer composite heat exchangers***

***Purpose***

- Modeling of fiber reinforced polymers is more challenging than modeling metals due to the inherit anisotropy that results from fiber orientation in the matrix. Elastic modulus, yield strength and thermal conductivity are as much as an order of magnitude higher in the direction of fiber alignment. Thus, finite element models must be very refined to capture the effects of the anisotropy.
- Previous finite element models completed for this task utilized free meshing and tetrahedral elements due to their simplicity and acceptable accuracy. However, new models must incorporate thermal effects in addition to structural effects. The coupled model reduced symmetry from quarter-symmetry to half-symmetry, resulting in significantly higher element counts and longer computation time. Mapped meshing with brick elements helps minimize computation time while maintaining or improving accuracy relative to the previous tetrahedral mesh. Figure 3 provides a comparison of the appearance of a free mesh of tetrahedral elements and mapped mesh of brick elements.

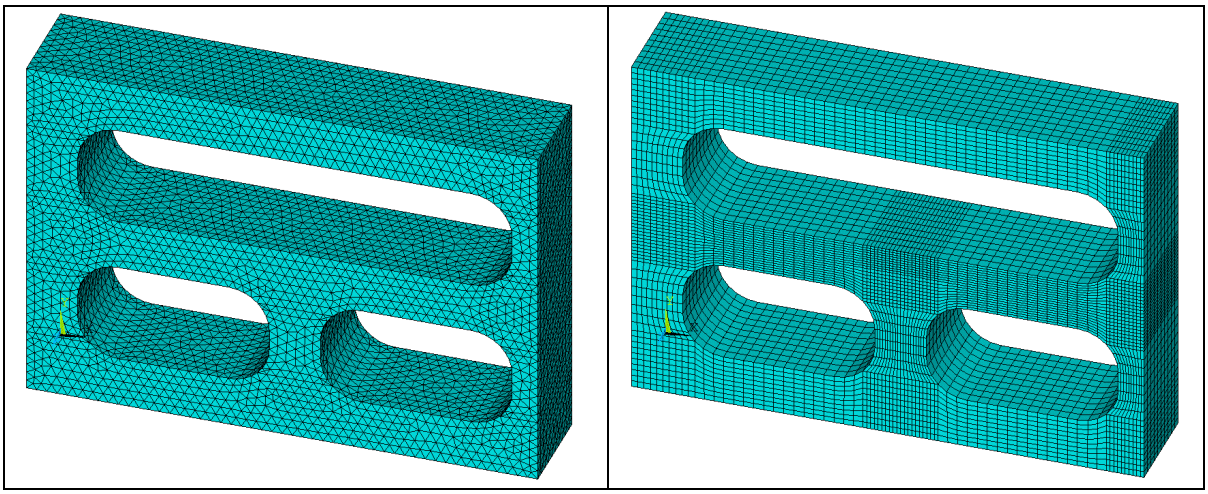

**Figure 3. Free mesh of tetrahedral elements (left) and mapped mesh of brick elements (right).**

- While developing the mapped mesh, the geometric flexibility of the model was enhanced to allow the user to input the following geometric parameters: number of gas-side fins, number of water-side fins, fin height, fin thickness, plate thickness, overall heat exchanger width and overall heat exchanger depth. Variation of these geometric parameters will allow for the study of geometric effects on stress and temperature distributions of orthotropic heat exchanger models. Furthermore, the geometry can be optimized for each application to ensure safety and maximize heat transfer performance.

***Mapped Mesh Comparison with Free Mesh***

- Mapped mesh refinement utilized the following mesh parameters: XY-spacing, spacing ratio, number of division and Z-spacing to determine the optimum mesh that maintained or exceeded accuracy of the previous tetrahedral mesh while minimizing

element count. Table 1 provides the range of parameters used for the refinement study.

**Table 1. Mapped mesh refinement parameters**

| Parameter | No. of Divisions | Spacing Ratio | X and Y Size (mm) | Z Size (mm) |
|---|---|---|---|---|
| Low Value | 5 | 2 | 1.0 | 1.00 |
| Middle Value | 10 | 10 | 0.5 | 0.50 |
| High Value | 20 | 20 | 0.1 | 0.25 |

- The maximum stress values of the mapped mesh were compared with those from the previously accepted free mesh using a metric called the sum of squares error. Several of the mapped meshes studied had lower sum of squares errors and shorter runtimes relative to the previously accepted free mesh. From these mapped meshes, the one with the lowest element count was chosen for additional studying. The element count was reduced (via appropriate changes to the mesh refinement parameters) while maintaining the accuracy of the mesh.

- The final, optimized mesh had 183,500 elements, which was 64% fewer than the initial brick mesh, which had 507,400 elements. The reduction in elements significantly reduced computation time. Figure 4 shows the finalized brick mesh, which will serve as the starting point for the thermal studies.

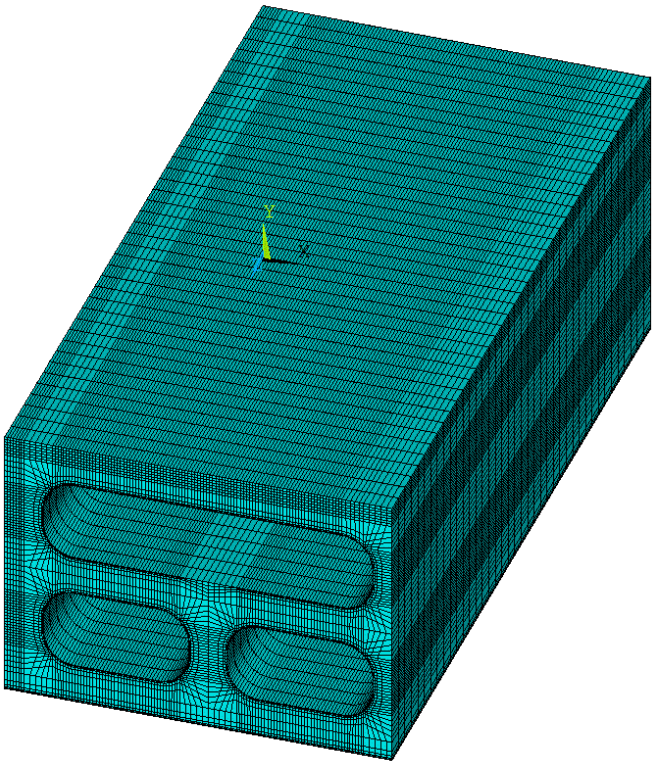

**Figure 4. Finalized brick mesh.**

### *III. Assess feasibility of modeling orthotropic heat exchanger module as an isotropic model with averaged properties*

- Isotropic models are much simpler than orthotropic and anisotropic heat exchanger models and their simplicity results in significantly reduced computation time. Thus, it would be very favorable from a modeling standpoint if the mechanical behavior of an anisotropic model could be replicated using an isotropic model.
- In the isotropic model, a range of elastic moduli (2 to 6 GPa) and range of Poisson's ratios (0.24 to 0.44) served as the input mechanical properties because these values cover most of the range of the orthotropic mechanical properties previously used for modeling. The maximum stress magnitude results over the studied range of isotropic properties are shown in Table 2. The results indicate that, over the range of isotropic properties studied, the stress distributions of isotropic models do not replicate the stress distributions of an orthotropic property. As such, the orthotropic model cannot be simplified to an isotropic material with averaged properties.

**Table 2. Maximum stress magnitude results from isotropic and orthotropic results**

| Elastic Modulus (GPa) | Poisson's Ratio | Maximum X-Stress (MPa) | Maximum Y-Stress (MPa) | Maximum Z-Stress (MPa) | Maximum XY-Stress (MPa) | Maximum YZ-Stress (MPa) | Maximum XZ-Stress (MPa) |
|---|---|---|---|---|---|---|---|
| 2 | 0.24 | 33.5 | 42.5 | 8.3 | 23.4 | 1.7 | 3.4 |
| | 0.34 | 33.7 | 43.0 | 11.9 | 23.4 | 2.4 | 4.9 |
| | 0.44 | 34.7 | 43.9 | 15.9 | 23.5 | 3.1 | 6.3 |
| 4 | 0.24 | 33.5 | 42.4 | 8.3 | 23.4 | 1.7 | 3.4 |
| | 0.34 | 33.8 | 43.0 | 11.9 | 23.4 | 2.4 | 4.9 |
| | 0.44 | 34.6 | 44.3 | 15.9 | 23.5 | 3.1 | 6.3 |
| 6 | 0.24 | 33.6 | 42.5 | 8.3 | 23.4 | 1.7 | 3.4 |
| | 0.34 | 33.8 | 43.0 | 11.9 | 23.4 | 2.4 | 4.9 |
| | 0.44 | 34.7 | 44.3 | 15.9 | 23.5 | 3.1 | 6.3 |
| Orthotropic | | 53.7 | 73.7 | 10.0 | 14.7 | 3.0 | 3.1 |

*IV.* ***Refine model simplification guidelines and techniques for mold filling metamodel of plate-fin polymer heat exchangers***

***Motivation:*** Previous work demonstrated the viability of model simplification techniques for a portion of the PHX design space. Further refinement of the guidelines for applicability and the techniques to be employed is necessary for precise utilization of model simplification methods for mold filling metamodeling

***Action Plan:*** Using basic finned geometries, we examined the effects of fundamental properties such as fin volume and location on mold filling and refine model simplification technique to reduce error across the design space

***Findings:*** In order to reduce the filling behavior of a finned plate to its most fundamental properties, a single ring fin was placed around the injection point, as shown in Figure 5, and the size of the fin and distance from the injection point was varied

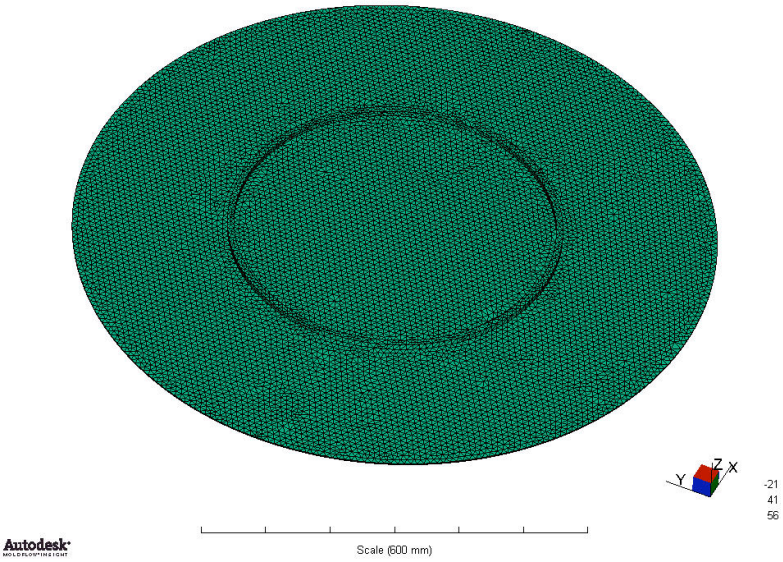


**Figure 5. Disc with single ring fin geometry.**

- Utilized model simplification to reduce the complex geometry to a scaled-thickness base plate
  - Filling-based model simplification: Based on the filling behavior of the original finned geometry, the base thickness was scaled according to Equation 1. By maintaining the filled radius and adjusting the thickness to match the filled volume, this method provided an approximation of the filling behavior as the flow progressed evenly away from the injection point. The scaled thickness value was tuned to reduce error by adjusting k based on simulation findings

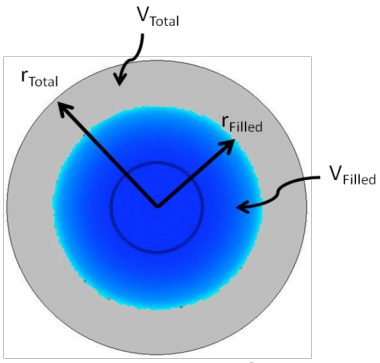


**Figure 6. Important dimensions for model simplification.**

$$t_{scaled} = k\frac{V_{Filled}}{\pi r_{Filled}^{2}}$$

**Equation 1. Filling-based model simplification**

- Developed a range of case studies to analyze the effects of fin location and fin size
  - Varied fin location by changing the inner diameter of the ring fin: 150mm, 300mm, and 500mm
  - Varied fin size by changing the percent fin volume relative to total volume: 2%, 5%, 10%, 20%, 30%
  - Varied fin height with generally short and tall fins
- Moldflow® simulations were performed for the specified case studies
  - There was little difference in accuracy between the mold filling of generally short and tall fins of equal volume.
  - If the fin was located a sufficient distance before the flow front reached the velocity/pressure switchover point, there was relatively little change in accuracy based on fin distance from the injection point.
  - The selected model simplification technique developed severe accuracy error as relative fin volume increased, as shown in Figure 7.

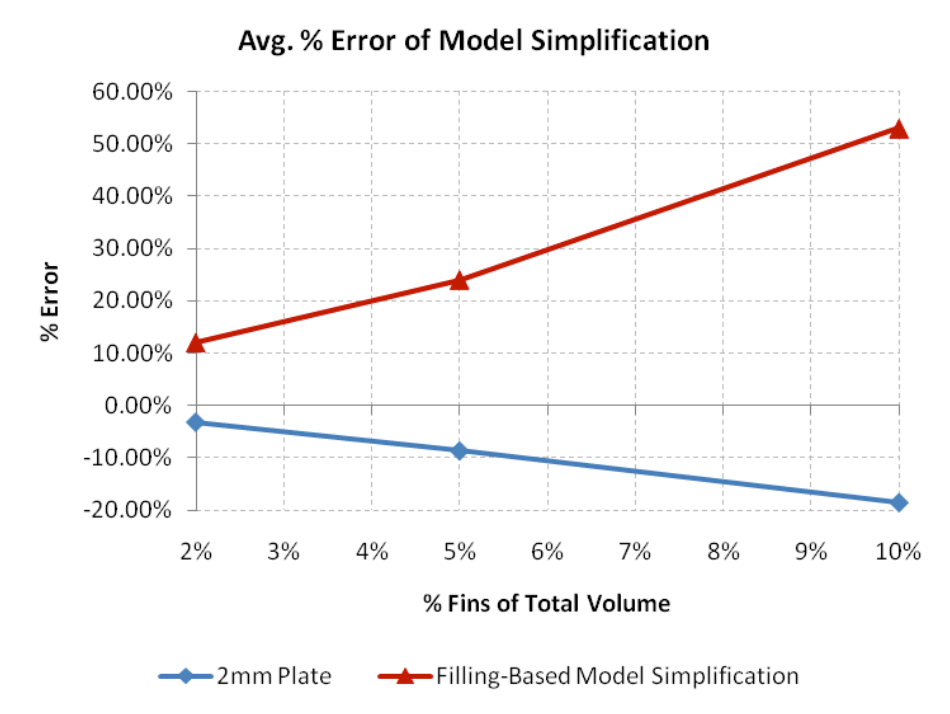


**Figure 7. Model simplification error vs. % fin volume.**

- To account for over-estimation of mold filling by the filling-based model simplification technique, a scaling factor was applied to the calculated thickness values. This successfully removed biasing in the error and dramatically improved the accuracy of the method. Using optimization methods, the best scaling factor for the employed method was 0.293 with an average error of 0.02% for the test cases examined.

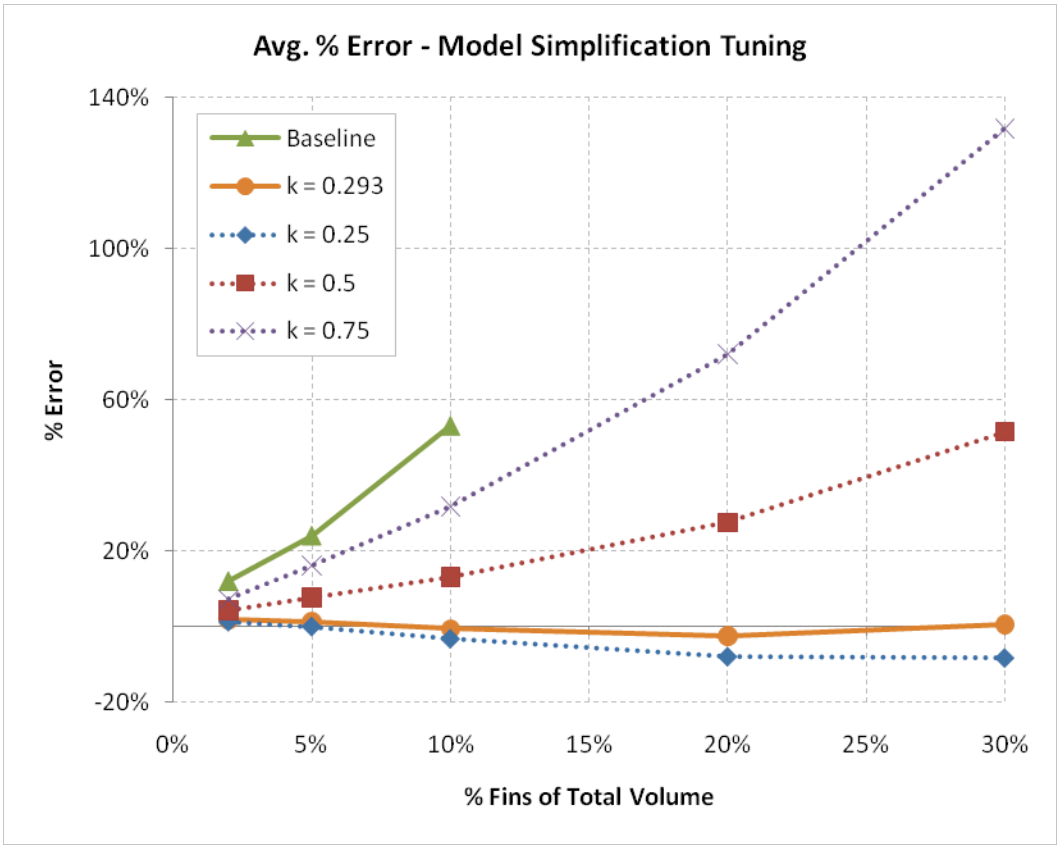


**Figure 8. Effects of scaling model simplification Method B.**

***V. Develop new datapoint selection methodology for improving the accuracy of the mold-filling statistical metamodel***

***Motivation:*** While model simplification techniques are useful for reducing the complexity of mold filling simulation, they are only applicable for certain design regions. A statistical metamodel of the overall design space is required in cases where model simplification techniques are unsuccessful. A statistical metamodel has been pursued previously but the accuracy was not satisfactory, generally due to a limited dataset and specifically due to a lack of information on the switching behavior from complete to incomplete filling. Additionally, it is computationally expensive to expand the dataset due to modeling and simulation requirements.

***Action Plan:*** We investigated methods to improve the accuracy of the statistical metamodel, specifically around the switching point from complete to incomplete filling, while reducing the amount the dataset that must be expanded.

***Findings:***

- The spatial partitioning method was chosen to partition the design space into completely filled, incompletely filled, and transition regions. The completely and incompletely filled regions are well defined and understood while the transition region defines the area that needs significant investigation in order to accurately determine whether a candidate design in this region would be completely or partially filled.
- The boundary growing method was selected to investigate the boundary of the spatial partition. This method utilizes a seed design in the transition region and searches with an expanding boundary from this point for other points in the transition region using multidimensional interpolation. As more points are found the definition of transition region improves and therefore the accuracy of the statistical metamodel improves.
- The recommended techniques ensure that any computationally expensive expansions to the dataset are utilized to search the areas of the statistical metamodel that are the sources of most accuracy error.

***VI. Develop a technique for characterizing mixing of polymer composites in a TSE***

- During mixing processes for creating polymer composites by combining fiber fillers in polymers, like Twin Screw Extrusion (TSE), the distribution of fiber fillers depends on the shear forces associated with the mixing process
- In this task, we used Calibrated Microencapsulated Sensors (CAMES) beads to trace the shear forces generated in the mixing process. CAMES beads are designed to measure shear stress during mixing by breaking at a specific critical stress level, which is dependent on the bead diameter, and releasing a dye (Red B Disazo) that can be optically measured. The selected range of diameters for the experiment was 53 - 63µm.
- Using the same dye that is encapsulated by the CAMES beads (Red B Disazo), "reference" dye shots were produced. The shots were prepared by dissolving polystyrene pellets in xylene and adding concentrated amounts of dye until the batch was solidified. The batch was then cut and weighed. The dye shots were used to produce reference RTD curves that represented 100% breakup of the CAMES beads.
- As a model polymer for the polymer composites being used for PHXs, a high-density polyethylene (HDPE) Alathon H6018 in pellet form from Equistar Chemicals was used in this investigation to calibrate the technique. The HDPE used in this study had a density of 0.960 g/cc and a melt index of 18.0 g/10 min.
- To measure the CAMES output after mixing, a reflective optical probe was placed at the die of the extruder. The probe consists of a split fiber-optic bundle, where light is transmitted from one fiber bundle. The light enters the melted polymer, reflects off the polymer and screw elements, and is collected by the other fiber bundle, where it is converted into a voltage signal. This signal is then filtered and recorded by a computer based data-acquisition system with a sampling frequency of 120 Hz.
- Residence time and stress distribution curves were generated from the data acquisition program and plotted together for each condition. Figure 9 below displays the RTD and RSD curves for one of the operating conditions.

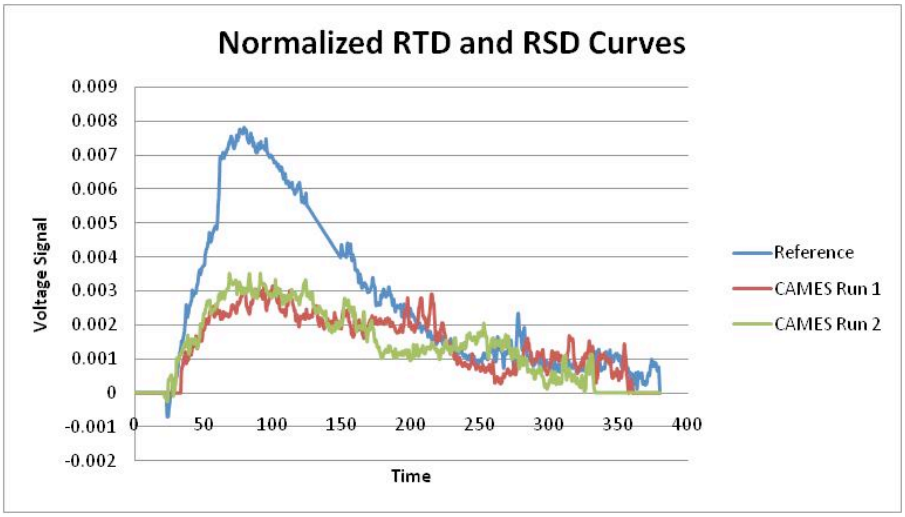


**Figure 9. Normalized RTD and RSD curves for 1.8lb/110rpm condition.**

- The results in Figure 9 show that the CAMES beads followed identical paths in the extruder, again validating that the beads were dropped in the same channel for each experimental run for this condition. Upon inspection, it is clear that the RTD curve has higher amplitude than the RSD curves, which indicates that 100% breakup of the CAMES beads was not achieved. However, the figure does indicate that at the tail

end of the curves the majority of CAMES beads broke during this segment as the RTD and RSD curves overlap.

- To calculate the percent breakup of CAMES beads, the areas under the RTD and RSD curves were determined, and the following equation was used to calculate the percentage of beads broken:

$$\text{Percent Breakup} = \frac{A_c}{A_r} \text{ x } 100\%$$

where $A_c$ is the area under the CAMES RSD curve and $A_r$ is the area under the ink RTD curve.

- The average percent break up for all nine experimental conditions was calculated and the results inserted into the central composite design grid for analysis, as seen in Figure 10.

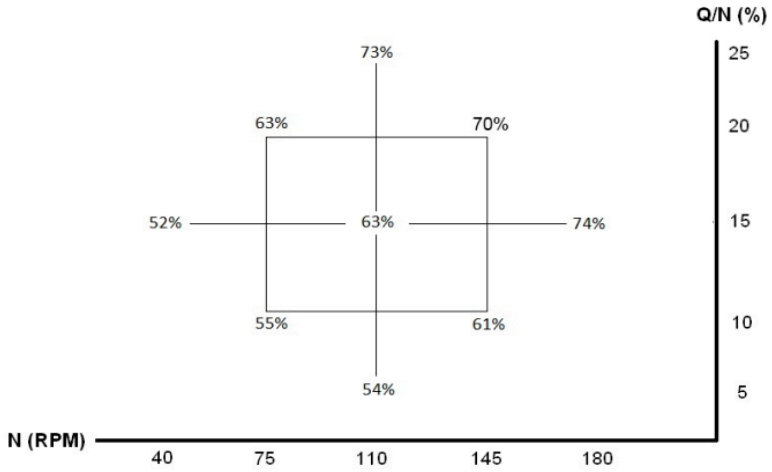


**Figure 10. Average percent breakup per condition.**

- The figure above indicates that there are some trends with the operating conditions and percent breakup. As the screw speed of the extruder is increased, the percent breakup of CAMES beads also increases for a given Q/N. This is expected as shear rate increases as screw speed increases as given by:

$$\dot{\gamma} = \frac{\pi DN}{h}$$

where D is the diameter of the extruder screws, N is screw speed, and h is the height of the screw channels.

- Another trend that is apparent is percent breakup increases as Q/N increases for a given screw speed. As the volume in the channels increases, the pressure on the melt while inside the kneading blocks also goes up, inducing higher levels of stress on the beads.
- To confirm that the range of obtained breakup was outside of experimental noise, an error analysis was performed and was found that there was an error of 2.3%. This provided validation that the range of percent breakup is independent of experimental error and that there is in fact a significant increase in percent breakup as N and Q/N are increased.

## 4. Difficulties Encountered/Overcome

- Not enough fiber-filled nylon can be obtained quickly enough
- Looking at obtaining fiber-filled PPS for better thermal properties

## 5. Planned Project Activities for the Next Quarter

- Design a cross-flow heat exchanger to be molded with thermally enhanced polymer, for use in new HX test rig
- Continue evaluation of thermal performance of candidate polymer heat exchanger designs
- Apply spatial partitioning and boundary growth techniques to develop improved mold-filling metamodel.
- Complete model simplification characterization using additional fundamental geometries and case studies.
- Utilize mold filling software to approximate full anisotropic structural and thermal material properties and compare the results of this anisotropic model with those of the orthotropic model to ensure similitude.
- Incorporate convection heat transfer from water and methane and verify results with those of current experimental polymer composite heat exchanger.
- Determine thermal stresses and deformation resulting from inclusion of convection loads.
- Conduct CAMES characterization on mixing of fiber-filled nylon in TSE.

## Appendix

### Goals

The goal of the proposed 3-year EERC II polymer composite heat exchanger (PCHX) project is to develop the science and technology needed to underpin the systematic design of polymer-fiber composite heat exchanger modules that address the needs of the fossil fuel industry. The project team, lead by A. Bar-Cohen, brings together expertise in thermal science and technology (Bar-Cohen, Rodgers) with polymer composite molding and manufacturing (Gupta, Bigio). Design studies and molding simulations, as well as fabrication and testing of laboratory-scale polymer composite heat exchangers, during the first phase of this project, have provided the foundation for aggressive pursuit of such polymer composite heat exchangers.

Successful development of cost-effective, high-performance PCHX's will require a detailed understanding of the limitations imposed on the thermal performance, mechanical integrity, and cost of such heat exchange devices by the candidate polymer material; carbon fiber geometry, orientation, and concentration; thermal and mechanical anisotropy of the polymer-fiber composite; molding processes; thermal and structural failure mechanisms in the molded heat exchanger; and the energy investment in the fabrication and formation of the heat exchangers. The development and experimental as well as numerical validation of a multi-disciplinary computerized design methodology, along with the fabrication and testing of scaled polymer heat exchanger modules, would provide a unique knowledge-base from which low-life-cycle-cost heat exchange systems for the petroleum and gas industries could be developed.

### Project Tasks

**A. Thermal Design and Characterization of Polymer Composite Heat Exchanger Module** (Prof. Avram Bar-Cohen - UMD, Prof. Hugh Bruck- UMD, Prof. Peter Rodgers – PI)

1. ***Design and thermofluid evaluation of PHX concepts for LNG applications***, including sensitivity of thermal performance to key parameters, quantification of primary thermal and exergy figures-of-merit (metrics), comparison to conventional heat exchangers, and identification of least-mass/least-energy designs;

2. ***Detailed design, fabrication, and thermal characterization of least-energy PCHX module***, including mold fabrication for most promising design, assembly and instrumentation of laboratory prototype, analysis of thermal and structural performance under simulated LNG processing conditions;

3. ***Development of predictive models for anisotropic heat exchanger modules***, including use of molding CFD software for prediction of fiber orientation and effective thermal/ structural properties, numerical and analytical models for molded anisotropic fins, derivation of least-material anisotropic fin equations, determination of heat flow sensitivity to fiber geometry/concentration/orientation;

4. ***Evaluation of convective enhancement features in molded channels***, including identification of "best practices" in conventional heat exchangers, manufacturability analysis of candidate features with attention to mold complexity, part ejection, and warpage, polymer composite molding of 3-5 candidate enhanced channels; thermofluid characterization of candidate enhanced channels under simulated LNG processing conditions; and

5. ***Determination of seawater effects on polymer composite finned plates***, including design and molding of test samples, immersion in saltwater tanks at different temperatures and concentrations for pre-determined periods, surface/bulk imaging and mechanical characterization before and after immersion, analysis and correlation of effects.

**B. Manufacturability Analysis and Mold Design for Polymer Composite Heat Exchanger Module** (Prof. SK Gupta – UMD, Prof. HA Bruck - UMD)

**1. *Development of an improved meta-model for mold filling predictions***: We plan to develop an improved meta-model for predicting mold filling for typical heat exchanger geometries. This meta-model will account for multiple gates with adjustable spacing. The data for developing this meta-model will be generated using mold flow simulations. We plan to utilize radial basis function based meta-models to provide the right balance of accuracy and computational speed.

**2 *Creation of a computational framework for gate placement to optimize fiber orientation***: We plan to develop a computational framework for placing gates to optimize the fiber orientation, utilizing simulated fiber orientations to select the gates. The sensitivity of the gate locations on fiber orientation will be developed. Gradient-based optimization techniques will be used to optimize the fiber orientation. The optimization problem will incorporate the constraint satisfaction formulation of the weld-line locations to ensure that the fiber orientation formulation produces acceptable weld-lines.

**3. *Generation of insert molding process models to incorporate connectors at the weld-lines*:** In order to ensure that the weld lines do not compromise the structural integrity, we plan to embed metal connectors at the expected weld-lines locations. In order to accurately place these metal connectors in the structures, we plan to develop process models of the insert molding process and mold design templates for performing insert molding.

4. ***Develop key relationships for the dependence of fiber orientation on the flow geometry of the finned-plate PCHX module,*** in commercially available polymer composites, including the effect of carbon fiber length and diameter, for high and low fiber concentrations, for both base plate and fin passages in the mold, and the effect of fiber orientation/distribution on thermo-mechanical properties, verify relationships with suitable small scale experiments;

**C. Polymer-Fiber Interactions in Polymer Composite Heat Exchanger Modules** (Prof. David Bigio – UMD)

1. ***Determine achievable thermo-mechanical property enhancement*** through control of carbon fiber orientation, in the commercially available polymer composites, with attention to flow regimes, mixing processes in the flow of the melt, and heat exchanger module design, and verify experimentally;

2. ***Explore optimization of PCHX polymer composite properties through the creation of novel polymer composite compositions***, including multi-scale filler geometries, develop the molding methods for the desired geometries, create the novel composites and experimentally verify improved thermo-mechanical polymer composite properties.

## References


[1] Bar-Cohen, A., Luckow, P., Cevallos, J.G., Gupta, S.K., 2010, Thermal Anisotropy in Injection Molded Polymer Composite Fins, International Heat Transfer Conference 14 at Washington DC

[2] Cevallos, J.G., Gupta, S.K., Bar-Cohen, A., Incorporating Moldability Considerations during the Design of Thermally Enhanced Polymer Heat Exchangers (under revisions)

[3] Cevallos, J.G., Bar-Cohen, A., Bergles, A.E., Gupta, S.K., Rodgers, P., Polymer Heat Exchangers – History, Opportunities, and Challenges (in progress)

[4] Luckow, P., A. Bar-Cohen, P. Rodgers, 2009, "Minimum Mass Polymer Seawater Heat Exchanger for LNG Applications," accepted for publication, ASME TSEA, January 2010

[5] Cox, H.L., 1951, "The elasticity and strength of paper and other fibrous materials," Brit. J. Appl. Phys., 3(3), pp. 72-79.

[6] Amado-Becker, A., Ramos-Grez, J., Yanez, M.J., Vargas, Y., and Gaete, L., 2008, "Elastic tensor stiffness coefficients for SLS Nylon 12 under different degrees of desensification as measured by ultrasonic technique," Rapid Proto. J., 14(5), pp. 260-270.

[7] Halpin, J.C., and Kardos, J.L., 1976, "The Halpin-Tsai Equations: A Review," J. Poly. Eng. and Sci., 16(5), pp. 344-352.

[8] Hahn, H.T., and Tsai, S.W., 1980, Introduction to Composite Materials, Technomic Publishing Co., Lancaster, PA.

[9] Pegoretti, A., Fambri, L., Zappini, G., and Bianchetti, M., 2001, "Finite element analysis of a glass fibre reinforced composite endodontic post," Biomaterials, 23, pp. 2667-2682.

[10] Fu, S., and Lauke, B., 1997, "The elastic modulus of misaligned short-fiber-reinforced polymers," Comp. Sci. and Tech., 58, pp. 389-400.

[11] Foye, R.L., 1972, "The Transverse Poisson's Ratio of Composites," J. Comp. Mater., 6(2), pp. 293-295.

[12] "Thermal Graph DKD," Cytec Industries, Accessed 26 May 2010, http://www.cytec.com/engineered-materials/products/cfThermalGraphDKDX.htm.

[13] Robinson, F., Bruck, H., Gupta, S.K., and Bar-Cohen, A., 2010, "Saltwater Hygrothermal Aging Studies of Short Carbon Fiber Reinforced Polyamide 12," ASME International Mechanical Engineering Congress & Exposition, Vancouver, British Columbia, Canada, November 12-18, 2010.

# Microchannel-Based Absorber/Stripper and Electrostatic Precipitators for $CO_2$ Separation from Flue Gas

**UMD Investigators: Serguei Dessiatoun, Amir Shooshtari, Michael Ohadi**
**GRA: Radoslaw Kuzmicki**
**PI Investigators: Afshin Goharzadeh, M. Alshehhi**
**Start Date: Oct 2006**

## 1. Objective/Abstract

This project is focused on research leading to the development of a high-efficiency $CO_2$ separation mechanism with application to a diverse range of processes in the oil and gas industry, including $CO_2$ separation separation/injection in petrochemical and refining processes, gas sweetening, and $CO_2$ capture for enhanced oil recovery applications.

The removal of acidic gases such as carbon dioxide from gas streams is an important process in the natural gas industry. In gas sweetening at least 4% by volume of raw natural gas consists of $CO_2$ which needs to be lowered to 2% to prevent pipeline corrosion, to avoid excess energy for transport, and to increase heating value. The separation of $CO_2$ from flue gases and its use for enhanced oil recovery and $CO_2$ sequestration applications is an increasing area of importance, as evidenced by the large investments in this area by ADNOC and its group companies, as well as affiliated government agencies in Abu Dhabi. A typical $CO_2$ separation process involves three stages: cooling down the flue gas; separating the solid particles and condensed water droplets; and finally capturing the $CO_2$ using the absorption process. The microchannel-based $CO_2$ separator being developed in this project will significantly increase controllability of the thermal state of the reaction and the efficiency of the separation process while decreasing the reaction time and energy consumption, as well as potentially substantially reduce of equipment footprint and the associated capital investment.

Flue gas also usually contains many contaminants in solid and liquid forms, the bulk of which are separated in gravity and inertia-driven feed gas separators. However, fine particles are carried on with the flow and can damage compressors, contaminate the gas absorption process, and reduce the quality of gas products. Electrostatic separation is one of the most effective techniques for separation of such particles and will be used in this project. The present project will address separation of droplets and particles using an EHD gas-liquid separation technique to remove liquid particles suspended in a moving gaseous medium, followed by the proposed microchannel-based separation of the $CO_2$ from the stream once the fine particles in the flow have been removed.

The project is being conducted jointly by the team at UMD and at PI. The team at PI is focusing on the EHD separation process and absorption modeling, while the team at UMD has focused on the experimental work utilizing microchannel-based $CO_2$ separation and the absorption solution.

## 2. Milestones/Deliverables Scheduled for the Completed Quarter

- Improvement of experimental setup
- Experimental study of absorption of $CO_2$ in a single microchannel reactor

## 3. Executive Summary of Accomplishments in the Current Reporting Period

During this reporting period additional in-depth study of the processes and analysis of our experimental results contributed to our collective enhanced understanding of the physics and reaction kinetics. The team effort advanced in two fronts: mathematical modeling and experimental study. The main focus of the collaborators in the Petroleum Institute has been in mathematical modeling of the absorption process in microchannels, and during this period, they achieved considerable success in the development of the model. The team currently is focusing on improving the modeling capabilities and implementing the complicated absorption physics and the chemical reaction more in-depth.

Meanwhile, the focus of the collaborators at UMD has been on experimental study of the process and visualization study of the absorption of $CO_2$ in microchannels. During this period, the experimental setup was revised and a new set of data was collected. The phenomenon was also successfully demonstrated in a test channel and the performance was quantified. Some of the major results collected in this period and the outline of the future work are presented in the current report.

In this reporting period, the collaborators from the PI and UMD continued on a joint review of the project and shared ideas through biweekly video conferences and exchange of emails. The project has been strengthened also from addition of Dr. Kyu Yong Choi, a professor in chemical engineering, with extensive background and expertise in chemical reactions. Finally, an important accomplishment in this period was developing project milestones and delivery of a timetable, which were approved and committed to by both sides.

## 4. Summary of Project Activities for the Completed Quarter

### Modification in Experimental Setup

As explained in fifth quarterly report, the electrical conductivity (or resistivity) measurement was used to determine the amount of the absorbed $CO_2$ in a single-channel test section. However, it was noticed that the measurement method is susceptible to presence of gas bubbles. When unabsorbed gas bubbles travel between two electrodes of the measurement cell, the apparent conductivity of the medium between two electrodes decreases, leading to an underestimation of the amount of absorbed gas. To rectify this problem, a gas separator was added to the setup (Figure 1). The separator was position at the immediate exit of the microchannel.

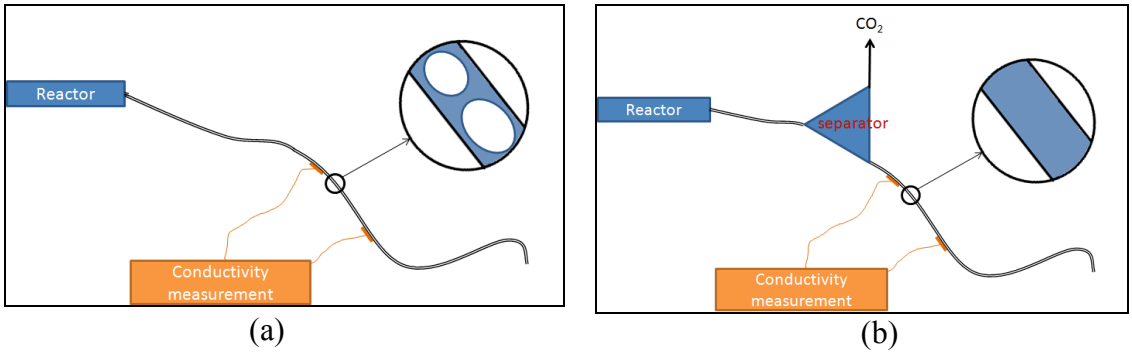


**Figure 1. a) Initial experimental setup; b) Modified experimental setup.**

A schematics drawing of the separator is presented in Figure 2. The mixture of DEA solution and unabsorbed $CO_2$ gas enters the separator, and as the result of the gravity, liquid moves downward while the gas releases from the top.

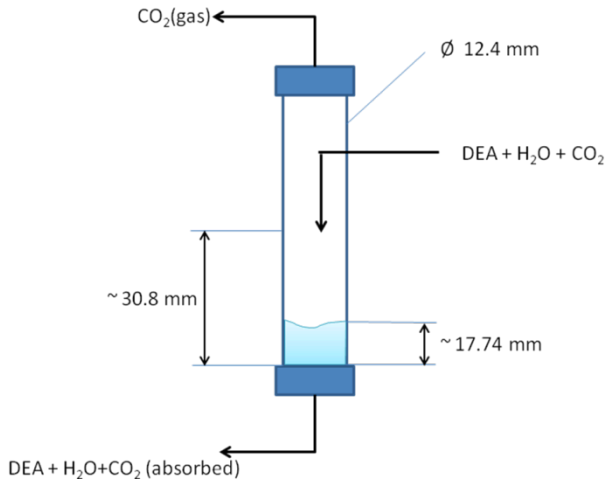


**Figure 2. Gas separator schematic design.**

During this reporting period the instrumentation used for the measurement of the gas flow rate was upgraded and the measurement accuracy was improved. For this purpose, instead of a rotameter, a laminar-based gas flow meter was used (Figure 3). This new instrument enabled us to measure in-line volume/mass flow rate, pressure and temperature of $CO_2$ gas entering the microchannel. The device also provides an output signal for direct reading by a data logger. The range of flow measurement by this device is 5ml/min to 500 ml/min with 1 ml/min or 0.8% of reading accuracy.


**Figure 3. Laminar-based gas flow meter.**

The entire modified experimental setup is presented in Figure 4. The syringe pump drives a precise amount of DEA solution to the microchannel reactor. The $CO_2$ gas is derived by pressurized gas cylinder. The flow rate, temperature and pressure of the flowing gas is measured by the laminar-based gas flow meter described above. The flow rate of the gas is adjusted manually via a needle valve (not shown in this figure).

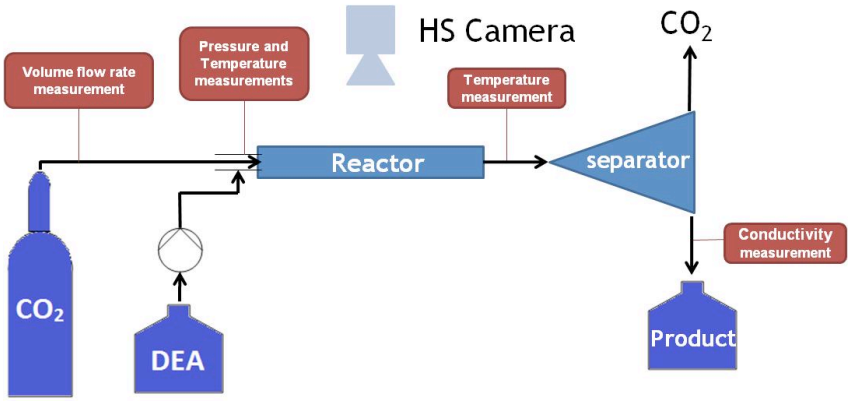


**Figure 4. Modified experimental setup.**

## New experimental setup for measurement of the electrical conductivity variation with the concentration of absorbed $CO_2$

As described in previous quarterly report, the electrical conductivity (resistivity) measurement was used to quantify the amount of $CO_2$ absorbed by DEA solution. This method consists of two stages. In the first stage, the electrical conductivity (or resistivity) of the amine solution after the microchannel is measured. In the second stage the measured conductivity is used to evaluate the amount or percentage of absorbed $CO_2$. The first stage can be conveniently achieved in the experimental setup as previously described. However, for the second stage, we need to know the relationship between the conductivity and the amount of $CO_2$ absorbed. With the current experimental setup only a two-point relationship could be obtained. For the first stage the conductivity of fresh DEA solution, when no $CO_2$ gas is injected in mirochannel, is measured to obtain the conductivity of the solution with 0% absorbed $CO_2$. For the second stage, first the DEA solution is saturated by the $CO_2$ bubbling method, and then the saturated solution is derived through the microchannel and conductivity meter to obtain the conductivity of the 100% saturated solution. Using the above method, the conductivity of two cases, one with 0% and the other with 100% absorbed $CO_2$, was determined.

In our previous calculations, since there was no information about the trend of conductivity versus absorbed $CO_2$, a linear relationship was assumed between these two extreme conditions. However, it was understood that a more accurate approach was needed. To overcome this problem, a new experimental setup for measurement of the electrical conductivity variation with the concentration of absorbed $CO_2$ was designed and fabricated. A schematic of this experimental setup is depicted in Figure 5. The Pyrex flask forms the reactor were the absorption of $CO_2$ in DEA aqueous solution takes place. The weight of solution must be accurately measured before the experiment. A three-way valve connects the gas storage bottle either to $CO_2$ tank for charging purpose or to the reactor for absorption process experiment. A gas pressure regulator maintains the system pressure of the reactor constant. However, unlike the pressure of reactor, the pressure of gas storage bottle varies gradually as $CO_2$ gas is absorbed by the DEA solution. A pressure transducer monitors this pressure. A magnetic stirrer promotes the absorption process in the reactor. A tubing pump circulates the liquid through the conductivity measurement cell and facilitates mixing of the $CO_2$ gas and the DEA solution. A cooling/heating circulating bath maintains a constant temperature of the solution during the experiment. Another pressure transducer measures the pressure of the gas after passing through the gas regulator. As the experiment proceeds, $CO_2$ gas flows from the storage bottle towards the reactor and gets absorbed by DEA solution. The conductivity cell measures the conductivity of the DEA solution as the concentration of absorbed $CO_2$ varies.

.

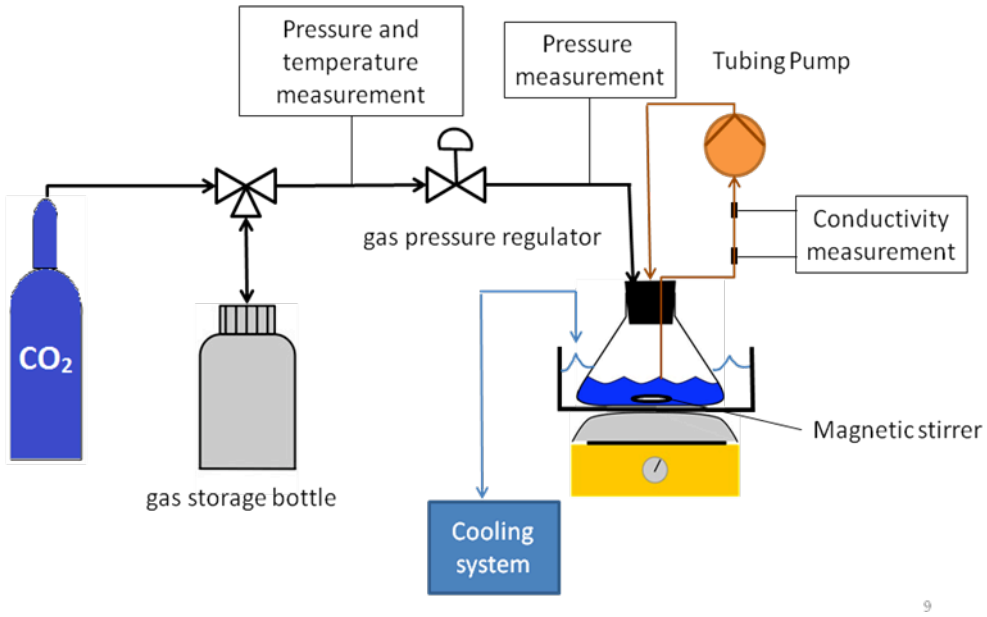


**Figure 5. Experimental setup for measurement of electrical conductivity as function of absorbed $CO_2$ concentration.**

In order to measure the amount of gas that leaves the storage bottle and is absorbed in DEA solution, the ideal gas equation can be used:

$$\Delta m = \frac{\Delta PV}{RT} \quad (1)$$

In this equation $\Delta P$ is the pressure variation of the gas storage bottle measured by the pressure transducer, $V$ is the total volume of the bottle and connecting tubes before the pressure regulator, $T$ is the temperature of the bottle measured by a temperature sensor, and $R$ is the gas constant for $CO_2$.

It is worth mentioning that this experiment is quite susceptible to the presence of any leakage in the setup. Therefore, special attention was given to locate the leaking spots and eliminate them.

## Experimental results

Using the experimental setup shown in Figure 5, a series of experiments was conducted to find the relationship between the electrical conductivity and the concentration of the $CO_2$ absorbed by the DEA solution. An aqueous solution of DEA with 20% mass basis concentration was prepared. A measured amount of mass of solution was poured in the Pyrex flask and the temperature of circulating water was set at 25°C. Using the gas regulator, the pressure was set at 5 psi and the variation of the liquid conductivity and the pressure of the gas storage bottle with time were recorded. This experiment was repeated nine times. The results of these nine runs are presented in Figure 6.

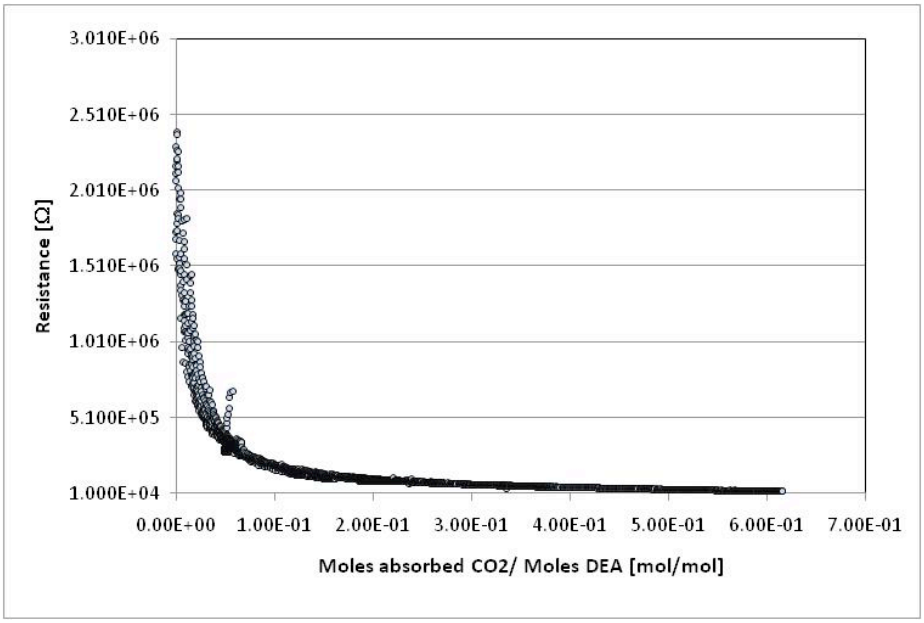


**Figure 6. Variation of electrical resistance versus $CO_2$ to DEA mole ratio.**

As shown, a nonlinear trend is obvious. Next, we need to derive a correlation to relate the electrical resistance of liquid to the concentration of absorbed $CO_2$.

According to the literature, the conductivity of a solution of a strong electrolyte at low concentration follows Kohlrausch's Law:

$$\Lambda = \Lambda^0 - K\sqrt{C} \quad (2)$$

where $\Lambda$ is the molar conductivity, i.e. the specific conductivity divided by concentration, $\Lambda^0$ is termed the molar conductivity at infinite dilution, $C$ is the concentration, and $K$ is a constant. If Kohlrausch's Law holds for DEA solution, one expects that the electrical conductivity must be a linear function of $C\sqrt{C}$. The variation of electric conductivity versus $(n_{CO_2}/n_{DEA})^{\frac{3}{2}}$ for the current set of data is shown in Figure 7.

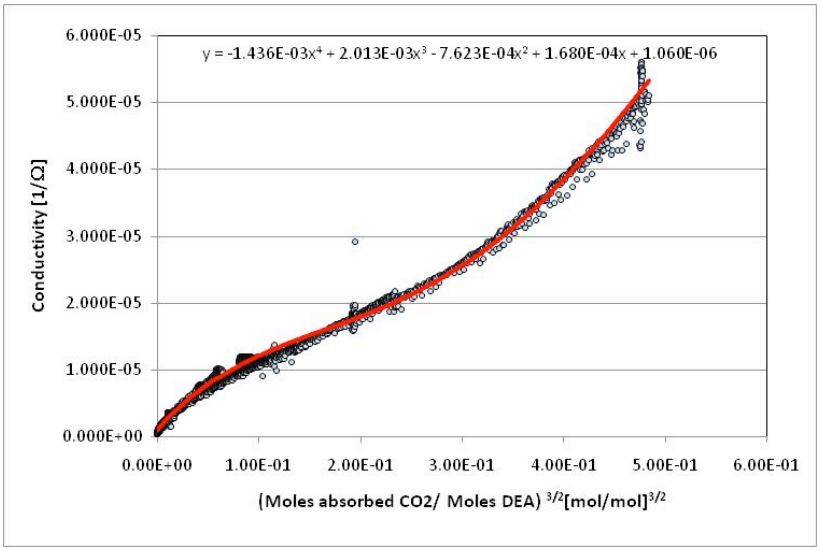


**Figure 7. The variation of electric conductivity versus $(n_{CO_2}/n_{DEA})^{\frac{3}{2}}$.**

A perfect linear trend was not observed. This perhaps is because the requirements for Kohlrausch's Law have not been satisfied in this experiment. Nevertheless, this graph helps us to determine the missing relationship between conductivity (or resistivity) and the amount of absorbed $CO_2$. This relationship can be written in the following form:

$$\sigma = (-1.436E-03)x^4 + (2.013E-03)x^3 - (7.623E-04)x^2 + (1.680E-04)x + (1.060E-06) \quad \textbf{(3)}$$

where $x = (\frac{n_{CO2}}{n_{DEA}})^{\frac{3}{2}}$ and $\sigma$ is the electrical conductivity. Therefore, if the electrical conductivity is given, using Equation (3), one can determine the amount of $CO_2$ absorbed by DEA solution. However, a few points must be noted. The above equation is derived when the $CO_2$ gas pressure and the temperature of solution are kept at 5 psi (34.5 kPa) and 25 °C, respectively. More experiments are needed to investigate the effect of these parameters on the coefficients of the above correlation. Moreover, the conductivity in Equation (3) is the total conductivity in 1/Ω. Therefore, using the area of the tube and the gap between the electrodes, the conductivity must be converted to specific conductivity.

The experiment described above can also be used to determine the maximum amount of $CO_2$ absorbed by DEA aqueous solution for the given pressure and temperature. From Figure 6, it can be seen that the maximum mole ratio achieved was about 0.6. However, the average overall for nine runs resulted in a lower value of about 0.4.

In Figure 8 from (Kohl and Nielsen 1985) the maximum concentration of $CO_2$ for various pressure and temperatures are presented. Note that in our experiments the aqueous solution contains 20% DEA by weight. Therefore, for the purpose of comparison, the data obtained by Mason and Dodge should be taken into consideration. From this figure, it can be seen that for a temperature of 77°F and a pressure of 5 psi, the mole ratio is about 0.7, which is higher than what was observed in our experiments. This difference could be due to number of reasons, such as presence of dissolved gases in the solution or impurity in DEA. Further experiments are needed to verify the results.

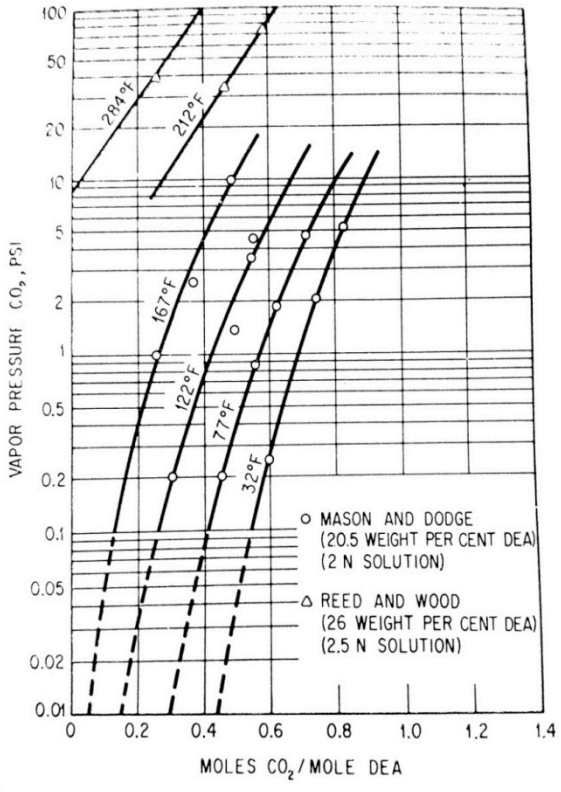


**Figure 8. Vapor pressure of $CO_2$ versus $CO_2$ concentration (Kohl and Nielsen 1985).**

Using the experimental setup shown in Figure 5, a number of tests were conducted. The results of these experiments are presented in Figure 9. The volume ratio was defined as $\frac{V_{CO2}}{V_{DEA\ Solution}}$, and the conductivity was measured by the conductivity measurement cell. The DEA solution flow rate was kept constant at 10 ml/min and 20 ml/min while the $CO_2$ flow rate was varied. As seen, the conductivity reaches a plateau when the volume ratio increases. This means the DEA solution becomes saturated with $CO_2$ and no more gas is absorbed. From the results it seems for the same gas to liquid volume ratio the conductivity for a liquid flow rate of 10ml/min is slightly higher than the one obtained for a flow rate of 20 ml/min. Therefore, it can be concluded that the amount of $CO_2$ absorbed would be proportionally higher. This could be because the residence time of liquid and gas flow in the microchannel is larger for lower flow rates. When the flow rate increases there is little time for absorption in the microchannel. Nevertheless, these results need further verification. The results can also be presented in terms of gas to liquid molar ratio (Figure 10). In order to calculate the number of moles of $CO_2$ flowing into the microchannel, the ideal gas relation must be used. For this purpose, the volume flow rate, the temperature, and pressure of the gas measured by the gas flow meter are used. In order to calculate the absorption efficiency and determine the amount of $CO_2$ absorbed in microchannel, the correlation between the electrical conductivity and the amount of absorbed $CO_2$ must be used. However, it must be noted that the correlation presented by Equation (3) is limited to a gas pressure of 5 psi. More experiments are needed to derive a similar correlation for higher pressures. Then, using these correlations and the results presented in Figure 9 and Figure 10, one can determine the absorption efficiency.

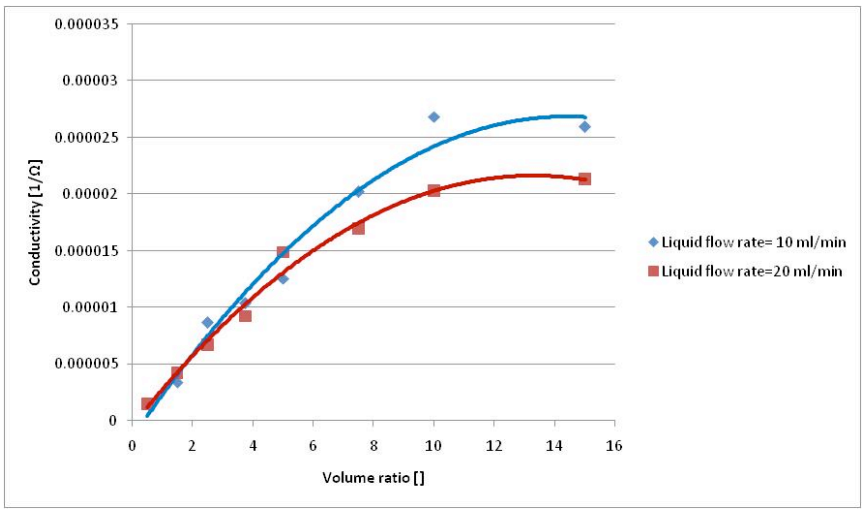


**Figure 9. Variation of conductivity versus gas to liquid volume ratio.**

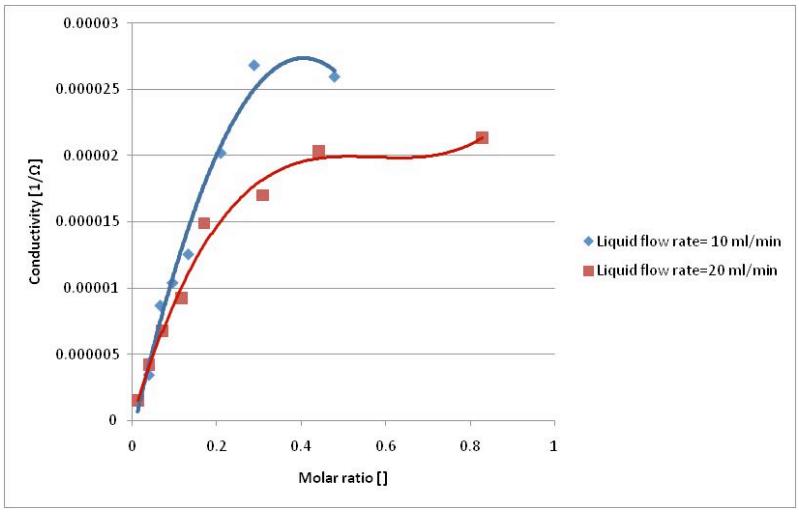


**Figure 10. Variation of conductivity versus gas to liquid molar ratio.**

The variation of temperature difference versus volume ratio is presented in Figure 11. Here $\Delta T$ is the temperature of the michrochannel outgoing mixture minus the temperature of the incoming $CO_2$ gas. This temperature increase is due to the heat of reaction generated in the exothermic absorption process. However, it should be noted that some of the heat can be lost from the microchanel wall. The variation of $CO_2$ absolute gas pressure at the microchannel inlet versus the volume ratio is presented in Figure 12. Since the pressure of the gas at the separator is atmospheric, this pressure can be used to estimate the pressure drop along the channel. As seen, the pressure varies almost linearly with $CO_2$ gas volume flow rate.

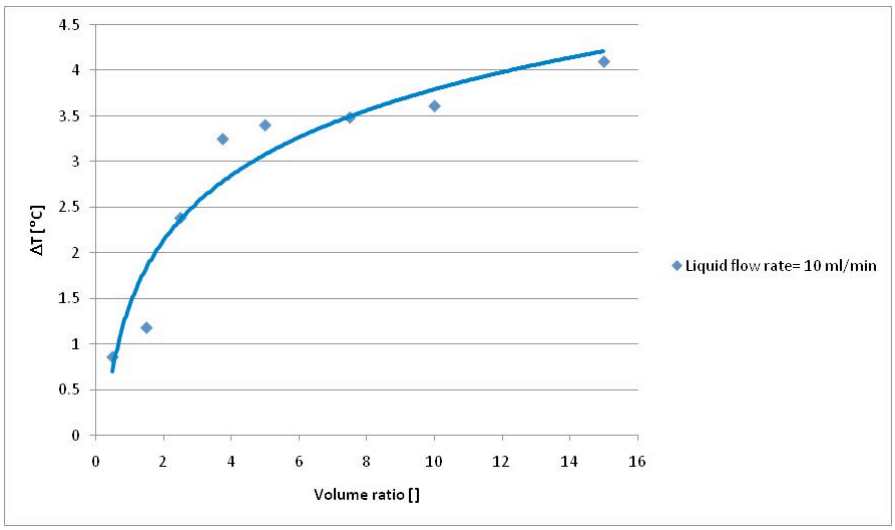


**Figure 11. Temperature difference variation with gas to liquid volume ratio.**

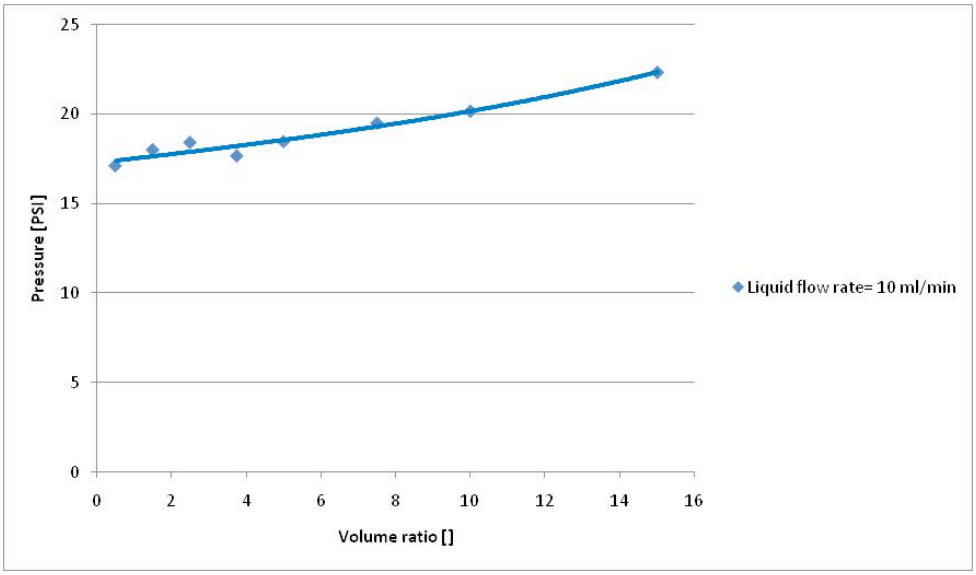


**Figure 12. $CO_2$ gas absolute pressure at the inlet of microchannel versus gas to liquid volume ratio.**

## Experimental summary of results

In this reporting period, a set of data from a recently fabricated stirred reactor was collected. The results showed a nonlinear trend between the electrical conductivity and the amount of $CO_2$ absorbed by the amine solution. This is especially important for assessing the efficiency of the microchannel reactor. Also, in this period a new set of data was collected for lower supply flow rate of DEA solution (i.e. 10 ml/min) into the microchannel. The results showed slightly better absorption performance compared to the results obtained for a twice higher flow rate of DEA solution. This could be due to a longer resident time of liquid travelling through the microchannel. More experiments are planned to confirm the trends observed in the collected data.

## 5. Difficulties Encountered/Overcome

None to report

## 6. Planned Project Activities for the Next Quarter

- Continue literature survey
- Conduct further experiments and collect data
- Conduct a parametric study
- Design/fabricate of a second-generation laboratory scale microchannel $CO_2$ separator
- Continue collaborative work with the PI partners to compare experimental results with numerical modeling results for the absorption process

## Appendix

### Justification and Background

The development of environmentally friendly process in industry is one of the major goals that have to be achieved. One way to approach cleaner environment is capturing or minimizing harmful gas components before emission to the atmosphere. One of the main gases which contribute significantly in global warming is $CO_2$. Due to a necessity to develop more efficient techniques for $CO_2$ capturing, scientific research in this area has been expanded rapidly. Since in the past very little R&D was devoted to $CO_2$ capture and separation technologies, opportunities for revolutionary improvements in $CO_2$ separation technologies is very high To maintain its competiveness and bring environmental friendly industry to the region, ADNOC has adopted various policies and approached it via many plans including "zero-flare" policy, acquiring more energy efficient process and the agreement signed with MASDAR to develop $CO_2$ capture technology. $CO_2$ separated from flue gases will be re-injected in oil wells, increasing oil production.

One of the promising concepts which can lead to major technology advancement is microchannel-based absorption units with enhanced kinetics. The objective of this study is to develop a full process of $CO_2$ separation from flue gas with incorporating micro-channel absorption technology at laboratory scale. The project addresses various stages of separation process: separation of solid particles and condensed water droplets and $CO_2$ separation using absorption process. Microchannel absorption $CO_2$ separator developed in this project will, significantly, increase the efficiency of separation process while decreasing energy consumption involved in such operation. Moreover, development of such technology will lead to reduction of equipment's size and, therefore, minimizing the footprint and cost of equipment. An electrostatic separator will be used prior to $CO_2$ separation to remove solid and liquid contaminants from flue gas. The ultimate objective is to design all separation stages such that the overall performance will be optimized.

### Approach

Detailed analysis and identification of the phenomena and the design challenges involved in effective implementation of the mechanism. Parametric study of existing and improved separators. Design iterations, including numerical flow and field simulations, fabrication, and testing. Creation of database and engineering design correlations.

### Three-Year Schedule

The schedule below reflects the revised scope approved by both sides

Year 1:

- Conduct literature review to understand the basic of mass transfer in micrreactor and separation of flue gas;
- Evaluate existing technologies and assess their applicability to $CO_2$ separation of flue gas;
- Repeat and implement some previous classical examples of microchannel separation to get familiarized with fundamentals and basic challenge;
- Analyze mixing in microchannels and possibility to use it in $CO_2$ separation;
- Continue improving efficiency of EHD separator for the fine liquid and solid particles;
- Conduct visualization study of liquid and solid particles migration in the electrical field.

Year 2:

- Continue on literature survey;
- Selection of the target alkanolamine;
- Simulate mixing and separation phenomena in microreactor via modeling and

analytical means;
- Develop laboratory scale microchannel absorber and desorber for $CO_2$ separation;
- Conduct Experimental study and design optimization study;
- Continue on visualization study of liquid and solid particles migration in the electrical field.
-

Year 3:
- Conduct visualization study on absorption and desorption in microchannels;
- Design iterations and implementation;
- Parametric study of $CO_2$ separation process and experiment on different designs;
- Continue on simulation of mixing and separation phenomena in microreactor via modeling and analytical means;
- Present the best design to ADNOC group of companies;
- Develop design correlation;
- Prepare report.

## References


[1] Aresta, Michael, ed. *Carbon Dioxide Recovery and Utilization.* Kluwer Academic Publishers, 2003.

[2] Kohl, Arthur L., and Richard B. Nielsen. *Gas purification.* Houston, Texas: Gulf Publishing Company, 1985.

[3] Rinker, Edward B., Sami S. Ashour, and Orville C. Sandall. "Kinetics and Modeling of Carbon Dioxide Absorption into Aqueous Solutions of Diethanolamine." *Ind. Eng. Chem. Res.* 35 , no. 4 (1996): 1107–1114.

# Microreactors for Oil and Gas Processes Using Microchannel Technologies

**UMD Investigators: Dr. S.V. Dessiatoun, Dr. K.Y. Choi, and Dr. M.M. Ohadi**
**Graduate research assistant: Meera Mahadevan**
**PI Investigators: Dr. Ebrahim Al-Hajri, Dr. Afshin Goharzadeh**
**Start Date: April 2009**

## 1. Objective/Abstract

Microfabrication techniques are increasingly used in gas and petrochemical engineering to realize structures with capabilities exceeding those of conventional systems. In addition to already demonstrated chemical analysis applications, microfabricated chemical systems have a number of advantages for chemical synthesis, chemical kinetics studies, and process development. Chemical processing advantages from substantially enhanced heat and mass transfer in optimally designed micro rector channels among other advantages promises much smaller equipment weight/volume, thus substantial potential saving in capital and operational costs of future reactor columns and systems.

Evaluation of different application of microreactors and their impact on applications of significance to the UAE petrochemical industry is one of the main objectives of the current project. Specifically, the application of microreactors in the polymerization of ethylene and propylene has been studied. Initial experimental results are very promising and may provide significant economical benefits.

## 2. Milestones/Deliverables Scheduled/delivered for the Completed Quarter

- Designed tubular polymerization microreactor
- Initiated study of ethylene absorption in the diluent

## 3. Summary of Major Project Achievements for the Completed Quarter

In this reporting period, the collaborators from the PI and UMD continued to review progress and share knowledge through biweekly video conferences and exchange of emails and other available media. Among major achievements, the project team was completed by addition of Dr. Kyu Yong Choi, a professor in chemical engineering with extensive background and expertise in chemical reactions, and Ms. Meera Mahadevan, a PhD student in chemical engineering who will be co-advised jointly by the departments of chemical and mechanical engineering. Another important accomplishment in this period was developing project milestones and a delivery timetable, which were approved and committed to by both PI and UMD. Specific technical tasks were accomplished, the results of which are presented below.

### Design of tubular polymerization microreactor

As described in the previous quarterly report, a typical catalyst used in the slurry loop reactor and in the gas-phase reactor is a Ziegler–Natta or metallocene catalyst deposited on highly porous 20-40 μm silica gel particles. During the polymerization process those particles are incorporated in a polymer, where polymer particles grow to 400-500 μm size. Our visualization study of particle flow in microchannels indicates that it is feasible to organize a stable polymer particle flow with

particle size as big as 500µm and at concentrations up to 20-30% by mass (Figure 1). The density of the polymer particles should be within ± 10% of the density of the diluent, and the minimum channel diameter should be at least 2800 µm (about 6 diameters of the particle). Such channel diameter would still lie in the microreactor range; however, our goal is to use much smaller channels in a range of 500 - 800 µm. This would allow much higher controllability of the reactor and a shorter reaction time.

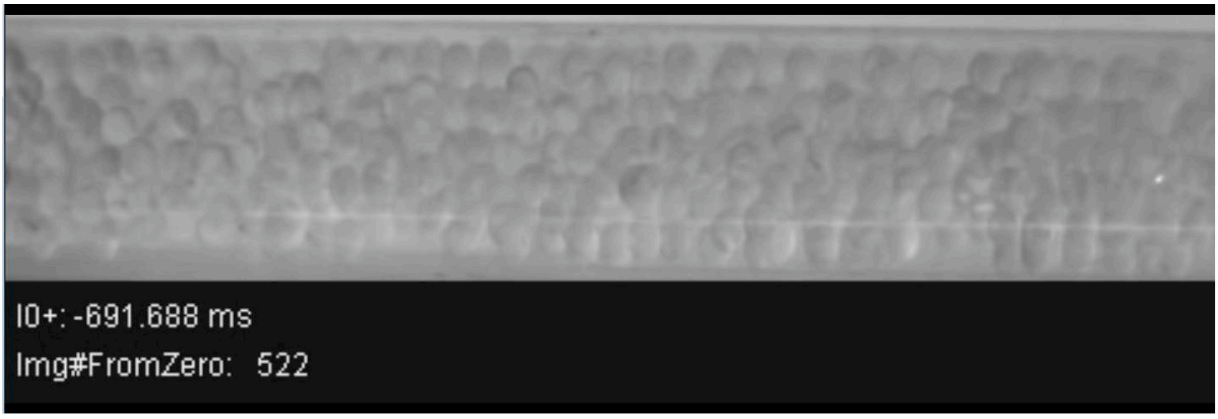


**Figure 1. Large polymer particle flow in microchannel.**

Typical diluents employed in alpha-monoolefin polymerizations include hydrocarbons having 3 to 12, preferably 3 to 8, carbon atoms per molecule, such as linear alkanes such as propane, n-butane, n-hexane and n-heptane, or branched alkanes such as isobutane, isopentane, toluene, isooctane and 2,2,-dimethylpropane, or cycloalkanes such as cyclopentane and cyclohexane or their mixtures. In the case of ethylene polymerization, the diluent is generally inert with respect to the catalyst, cocatalyst and polymer produced (such as liquid aliphatic, cycloaliphatic and aromatic hydrocarbons), at a temperature such that at least 50% (preferably at least 70%) of the polymer formed is insoluble therein. Isobutane is particularly preferred as the suspending medium for ethylene polymerization. For the initial experimentation stage we have selected a low-pressure diluent hexane. This simplifies fluid handling and experimentation.

We have conducted a flow visualization study of standard 20-40 µm catalyst support particle flow in the 800 µm microchannel (Figure 2). Despite more than triple density difference between silica particles and hexane (2.2 vs. 0.6548 g/mL), catalyst support particle flow was stable on all flow regimes studied. However initiating the dispersed particle flow in the microchannel required stirring the particle in the vessel with a magnetic stirrer. Particle flow is shown in Figure 2.

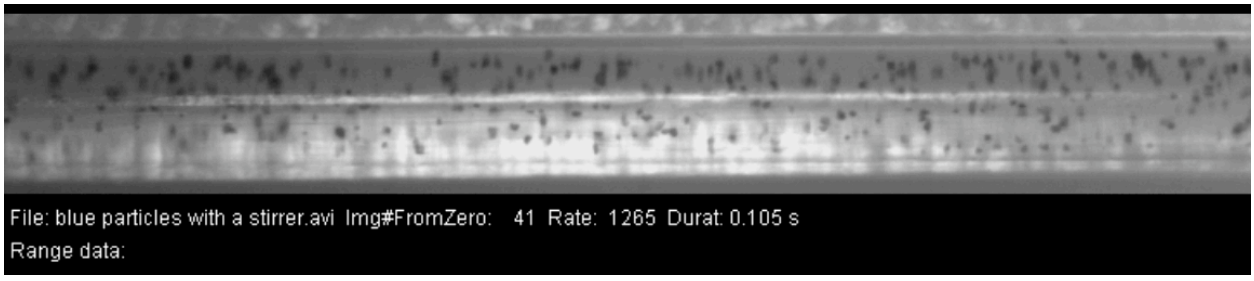


**Figure 2. Catalyst particle flow in microchannel.**

The example of conducting polymerization in the tubular microreactor is the work of Dow-Chemical [1]. The setup diagram is shown in Figure 3.

The polymerization experiments were carried out in a 1/16 in.(1.59 mm) OD, 0.050" ID reactor tubing. The reactor length, excluding the preheat section, was ca. 145 cm. The following procedure was used for the reactor startup:
– Set appropriate flow rates on the main solvent and injector pumps.
– Set the system pressure with the back-pressure control valve.
– Set the desired ethylene flow rate with the mass flow controller.
– Readjust PID parameters on the back-pressure valve to obtain a steady system pressure.
– Heat the reactor to desired temperature.
– Wait 20 min for system equilibration.
– Load the injector loops with activator and catalyst solutions.
– Inject these solutions with LC-injection valves.
– Collect the polymer solution.
– Repeat the injections and polymer collections to produce additional samples.

Polymerization experiments were carried out in single-phase (liquid) and two-phase (vapor-liquid) flow regimes. In single-phase polymerization, the ethylene concentration falls continuously along the length of the reactor. A key advantage of operating in the two-phase region is that an almost constant ethylene concentration is maintained along the length of the reactor. In effect, the vapor phase serves as a reservoir that replenishes ethylene consumed in the liquid-phase polymerization. In our microreactor also we will be using gas-liquid flow.

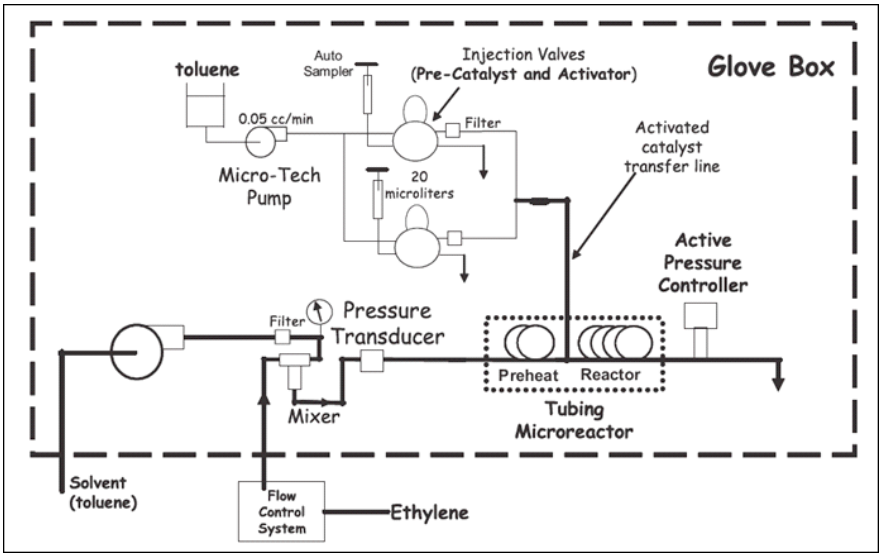


**Figure 3. Schematic of microreactor copying the conventional industrial process.**

Dow-Chemical researchers were intending to reproduce the conventional polymerization process in a microreactor. This process is complicated, requires control of several parameters and has to be conducted in the inert atmosphere of a glove box. The polymerization process and microreactor can be significantly simplified if the catalyst is pre-mixed to the desired concentration with the diluent that one or several monomers are added in the microreactor itself. A diagram of such microreactor is shown in Figure 4.

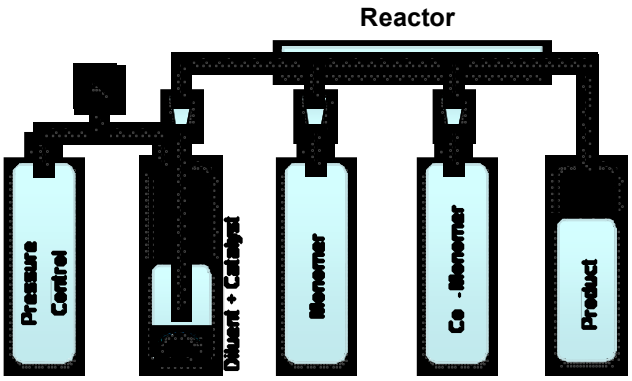


**Figure 4. Flow diagram of proposed microreactor.**

The proposed microreactor comprises of diluent reservoir that contains diluent with added catalyst, reservoirs with monomers and co-monomers that will be used in polymerization; flow initiating and measurement systems; the reactor itself and a product-collecting reservoir. Diluent will be dehydrated. Oxygen and other impurities that deactivate the catalyst will be removed using a process similar to Dow's process [2]. The monomer and co-monomer will be added to the diluent and catalyst particle flow, creating three-phase flow as shown in Figure 5. Three-phase flow will be created near constant concentration of monomer in the diluent, which, combined with constant temperature conditions that the microchannel heat exchanger can provide for the polymerization process, would create the possibility of complete control of the process. The visualization study of the three-phase flow in microchannel indicates an intense circular motion of the particles that would result in the intense gas-liquid heat transfer as well as mass transfer inside of the liquid plugs.

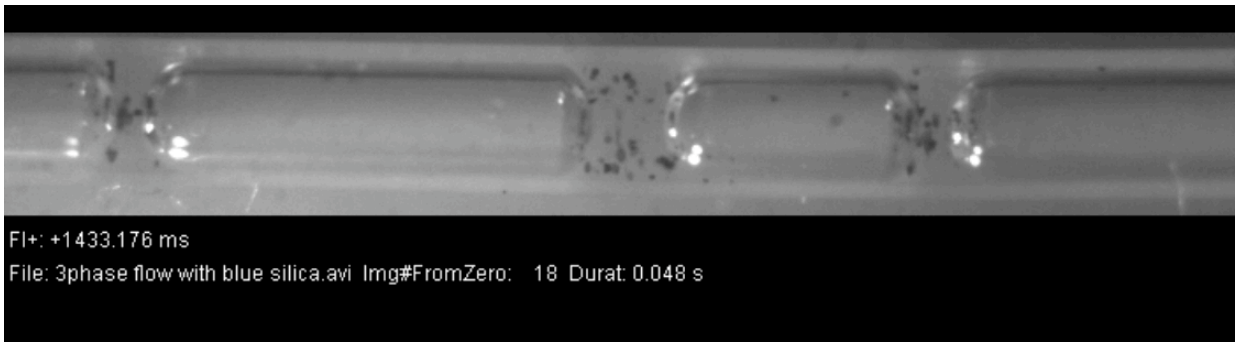


**Figure 5. Three-phase flow in microreactor.**

## Initiation of study of ethylene absorption in the diluent

Absorption of ethylene in the diluent flow in the microchannel will be crucial to the proposed polymerization process. Therefore, the closed look is taken to this process. An existing microchannel absorption experimental setup is used in this study. However, the gas mass flow meter was coupled with another flow meter that will be used in the microreactor setup for calibration (Figure 6). Both flow meters are calorimetric. However, their response times differ. At established flow readings, both flow meters are the same; however, the transition takes many seconds, as shown in Figure 7.


**Figure 6. Coupling of flow meters in the experimental setup.**

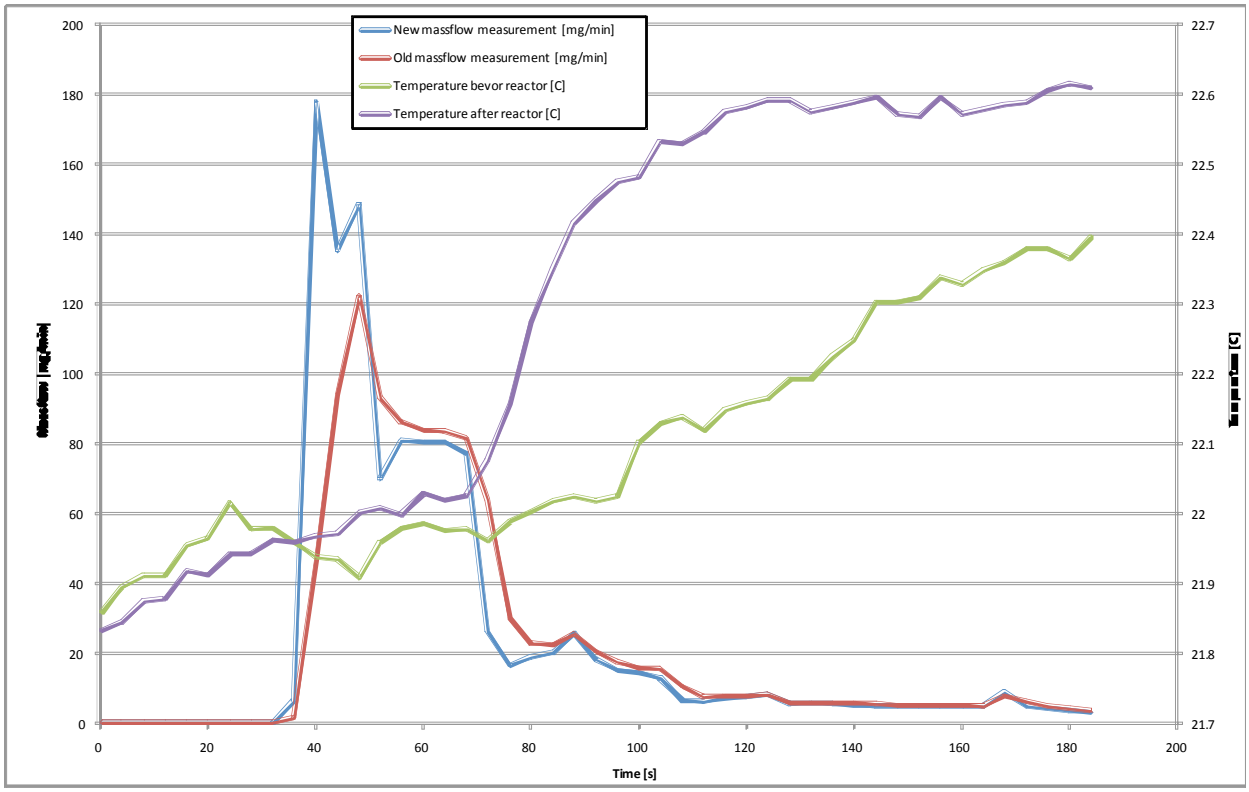


**Figure 7. Flow measurement with different flow meters.**

The Ethylene absorption flow is shown in Figure 8. Full absorption occurs in less than 200 mm long channel. However, concentration of absorbed ethylene was less than 1%. The absorption will increase with increased channel length and system pressure. Further investigation will be carried out to increase the absorption rate.

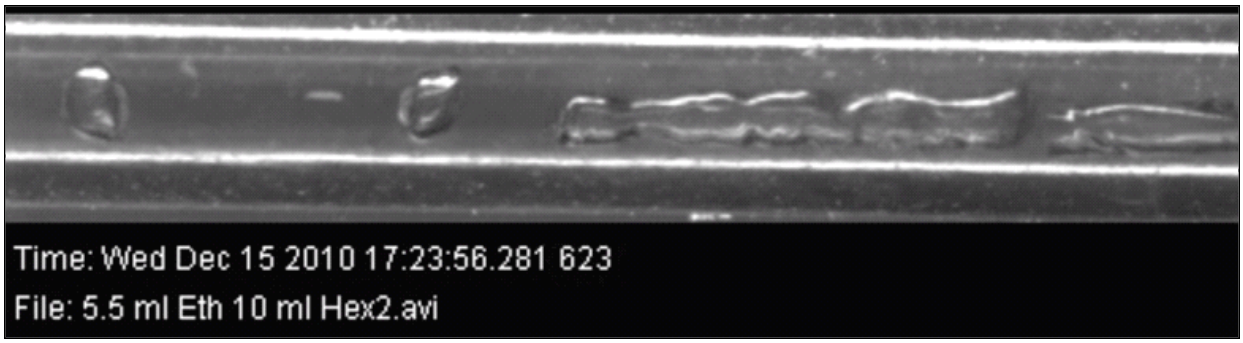


**Figure 8. Ethylene absorption in microchannel.**

## Modeling the reaction kinetics for a microreactor channel

To proceed further in this project it is important to have a theoretical basis for the design of the experiments we will be carrying out in the microchannel. A chemical reactor design involves two main aspects: a) the kinetics of the reaction and b) suitable reactor design suggesting its dimensions, including effects of flow, mass and heat transfer.

Objectives in modeling polymerization reactions are to compute

1. Polymerization rate
2. Polymer properties (molecular level and microscopic level) for various reaction conditions.
3. Dimensions and specifications of the microchannel to be used.

For example, an increase in reaction temperature in free radical polymerization results in increasing polymerization rate but decreasing polymer molecular weight. An increase in catalyst concentration raises polymerization rate but lowers polymer molecular weight. So there is a need for detailed understanding of the polymerization kinetics to devise a scheme to simultaneously achieve high productivity and desired polymer properties.

Some of the polymer properties that we are interested in are

Molecular weight distribution (MWD)
Molecular weight averages
Copolymer composition (CC)
Copolymer composition distribution (CCD),
Monomer sequence length distribution, short-chain and long-chain branching, crosslinking.
Stereoregularity

Polymer particle size,particle size distribution (PSD), and polymer morphology, etc., are not molecular properties but meso-scale properties that influence a polymer's physical, chemical, thermal, mechanical, and rheological properties.

There are 2 types of reaction mechanism we could consider for the polymerization reaction:

- Free radical chain polymerization
- Coordination polymerization

**Reaction kinetics—free radical mechanism**

1) Catalyst site activation $I \xrightarrow{k_d} 2R\bullet$
2) Initiation $R + M \xrightarrow{k_i} P_1$
3) Propagation $P_1 + M \xrightarrow{k_p} P_2$
4) Chain transfer to monomer $P_n + M \xrightarrow{k_p} P_{n+1} \quad (n \geq 1)$
5) Chain transfer to solvent $P_n + M \xrightarrow{k_{fm}} P_1 + M_n \quad (n \geq 2)$
6) Deactivation $P_n + S \xrightarrow{k_{fs}} M_n + P_1 \quad (n \geq 2)$
$P_n + P_m \xrightarrow{k_d} M_n + D^* \quad (n \geq 2)$

**Reaction kinetics—coordination mechanism**

1) Catalyst site activation $C_o + MAO \xrightarrow{k_a} C^*$
2) Initiation $C^* + M \xrightarrow{k_i} P_1$
3) Propagation $P_n + M \xrightarrow{k_p} P_{n+1}$
4) Chain transfer to monomer $P_n + M \xrightarrow{k_{fm}} P_1 + M_n$
5) Chain transfer to hydrogen $P_n + H_2 \xrightarrow{k_{fh}} M_n + C^*$
6) Deactivation $P_n \xrightarrow{k_d} M_n + D^*$
$C^* \xrightarrow{k_d} D^*$

Here,

$C^*$ – *Activated Catalyst*

$D^*$ – *Deactivated Catalyst*

$M$ – *Monomer*

$P$ – *Polymer*

$k$ – *Rate constants*

$M_n$ – *Dead polymer*

$n$ – *Chain length*

$P_n$ – *Live Polymer*

$I$ – *Initiator*

$R$ – *Radical*

We now represent the reaction rates with respect to each of the reactants and products by the following expressions:

| Free Radical | Coordination |
|---|---|
| $r_I = -k_d I$<br>$r_R = -2fk_d I - k_i RM$<br>$r_M = -k_i RM - k_p M\sum_{n=1}^{\infty} P_n - k_{fm} M\sum_{n=1}^{\infty} P_n$<br>$r_{P_1} = -k_i RM - k_p MP_1 + (k_{fm}M + k_{fs}S)\sum_{n=2}^{\infty} P_n - (k_{tc} + k_{td})P_1\sum_{n=2}^{\infty} P_n$<br>$r_{P_n} = k_p M(P_{n-1} - P_n) + (k_{fm}M + k_{fs}S)P_n - (k_{tc} + k_{td})P_n\sum_{n=2}^{\infty} P_n \quad (n \geq 2)$<br>$r_{M_n} = (k_{fm}M + k_{fs}S)P_n - k_{td}P_n\sum_{n=2}^{\infty} P_n + \frac{1}{2}k_{tc}\sum_{m=1}^{n-1} P_m P_{n-m} \quad (n \geq 2)$ | $r_M = -k_i C^* M - k_p PM - k_{fm} PM$<br>$r_{C^*} = -k_i C^* M - k_{fh} H_2^p \sum_{n=2}^{\infty} P_n - k_d C^*$<br>$r_{P_1} = k_i C^* M - k_p P_1 M + k_{fm}\sum_{n=2}^{\infty} P_n M$<br>$r_{P_n} = k_p(P_{n-1} - P_n)M - k_{fm} MP_n - k_{fh} H_2^p P_n - k_d P_n$<br>$r_{H_2} = -k_{fh} H_2^p \sum_{n=2}^{\infty} P_n$<br>$r_{M_n} = -k_{fm} MP_n + k_{fh} H_2^p P_n + k_d P_n$ |

**Molecular weight moments**

Polymers produced from a reaction are distributed over a wide length range, and usually a Gaussian distribution of molecular weights is assumed. Normalizing this weight distribution is an aspect that can be worked on. Weight moments are defined to get a polymer weight distribution based on the chain length:

- Live polymer moment

$$\lambda_k' = \sum_{n=1}^{\infty} n^k P_n$$

- Dead polymer moment

$$\lambda_k = \sum_{n=2}^{\infty} n^k M_n$$

- The number average and weight average polymer molecular weights are defined as

$$\bar{M}_n = M_0 \frac{\lambda_1^1 + \lambda_1}{\lambda_0^1 + \lambda_0} \quad \text{and} \quad \bar{M}_w = M_0 \frac{\lambda_2^1 + \lambda_2}{\lambda_1^1 + \lambda_1}$$

The instantaneous chain length distribution for olefin polymerization is given by a single-parameter equation, Flory's most probable distribution (Flory, 1953), where w(r) is the weight chain length distribution for polymer chains of length r, and τ is the ratio of all chain transfer rates to the propagation rate.

$$w(r) = r\tau^2 \exp(-r\tau),$$

The chain length distribution function is often combined with a reactor residence time distribution function to calculate the overall molecular weight distribution in a continuous process.

**Microreactor:**

The microchannel can be considered as a plug flow reactor of a few microns diameter. We consider an unsteady state flow and ignore axial and radial dispersions and assume isothermal behavior initially for simplicity.

A mass balance for a PFR results in the following equation where $C_I$ is the concentration of a component 'I' varying along the length of the reactor 'y'. 'v' is the velocity of flow, '$A_r$' is the crosssectional area of the reactor, and '$r_i$' is the reaction rate with respect to component i.

$$\frac{\partial C_i}{\partial t} = -\frac{v}{A_r}\frac{\partial C_i}{\partial y} + r_i$$

Using all the above equations we obtain a mass balance for the coordination mechanism in terms of moments:

$$\frac{\partial \lambda_\circ^{'}}{\partial t} = -u\frac{\partial \lambda_\circ^{'}}{\partial y} + k_p M\beta\lambda_\circ^{'} - (k_{fh}H_2^p + k_d)(1-\alpha^{1-n})\lambda_\circ^{'}$$

$$\frac{\partial \lambda_\circ}{\partial t} = -u\frac{\partial \lambda_\circ}{\partial y} + (k_{fh}H_2^p + k_d + k_{fm}M)(1-\alpha^{1-n})\lambda_\circ^{'}$$

$$\frac{\partial M}{\partial t} = -u\frac{\partial M}{\partial y} + (k_i\beta + k_p + k_{fm})\lambda_\circ^{'}M$$

$$\frac{\partial H_2}{\partial t} = -u\frac{\partial H_2}{\partial y} - k_{fh}(1-\alpha^{1-n})\lambda_\circ^{'}H_2^p$$

**Evaluation:**

- **Feasibility: high;**
- **Impact: high.**

## 4. Difficulties Encountered/Overcome

Visualization of actual polymerization process at high pressure and temperature in the microreactor.

## 5. Planned Project Activities for the Next Quarter

- Design and fabrication of a microreactor capable of realization of selected polymerization process.
- Continue the polymerization modeling

## Appendix

### Justification and Background

Microreactors form a basis for the potential future downscaling of existing chemical processes, allowing tremendous reductions in capital and operating cost. They provide finer control of conditions, allow for faster process times, and improve safety in operation. Also, they should not encounter a significant problem in scaling from laboratory-sized systems to commercial-sized systems, since their operating principle will simply allow them to be stacked together modularly.

Of critical importance to the microreactors' capability to make the jump into industrial applications is the mixing efficiency, which controls the reaction rates and the yield expected from a reactor. Due to the scale of the systems, laminar flow is almost always encountered, which means that the vortices typically associated with turbulent flow are often missing. Instilling vortices into the flows to encourage mixing is accordingly a matter of construction of mixer channels.

Correct design parameters of microreactor influence the process yield. Designing microreactor for appropriate reaction conditions is very important for the reactions to be fast. Microreactors can be energy efficient too by appropriately designing and visualizing heat transfer. The channel dimensions have direct impact on diffusive mixing of reactants.

### Approach

- Literature survey of the microreactor technologies as well as microchannel fabrication technologies.
- Selection of the target process for realization in microreactors with maximum benefit.
- Selection of microchannel fabrication technology suitable for microchannel mass production.
- Design and fabrication of a microreactor using microchannel fabricating technology suitable for mass production.
- Microreactor demonstration.
- Prepare experimental set-up and conduct the experiments.

### Two-Year Schedule

Year 1:

- Conduct literature review to study current technologies for micoreactors, micromixers, and incorporation of catalysts into microreaction technology.
- Evaluate existing microchannel formation techniques and their applications to microreactor construction.
- Selection of the target process for realization in microreactors with maximum benefit to ADNOC.
- Selection of microchannel manufacturing process most suitable for mass production.
- Preparation of a microreactor testing facility.
- Visualization study of mixing in microchannels.

Year 2:

- Literature survey of the olefin polymerization technologies focus on microchannels
- Selection of the target polymerization process for realization in microreactors with maximum benefit.
- Design and fabrication of a microreactor capable of realization of selected polymerization

process
- Select type and size of catalyst particles to be used in the process
- Investigate propagation of selected catalyst particles in microchannels
- Investigate polymerization and polymer particle behavior in microchannels
- Parametric study of polymerization process at different temperatures, catalyst and reactant concentration.
- Microreactor demonstration.
- PI-side participation:
- 1. Selection in cooperation with Borouge of the catalyst for the target polymerization process for realization in microreactors.
- 2. Prepare a microreactor testing facility.
- 3. Visualization study of mixing in microchannels
- 4. Combine PI/UMD testing of the microreactor
- 5. Microreactor demonstration to ADNOC representatives
- 6. Prepare final project report and recommendations.

## References

[1] Daryoosh Beigzadeh, Charles A. Nielsen, Study of Ethylene Polymerization Under Single Liquid Phase and Vapor-Liquid Phase Conditions in a Continuous-Flow Tubular Reactor, Chem. Eng. Technol. 2007, 30, No. 8, 1088–1093.

[2] A. B. Pangborn et al., J. Organomet. 1996, 15, 1518.

# Thrust 3
# Energy System Management

# Integration of Engineering and Business Decisions for Robust Optimization of Petrochemical Systems

**UMD Investigators: Shapour Azarm, P.K. Kannan**
**PI Investigators: Ali Almansoori, Saleh Al Hashimi**
**UMD GRA: Weiwei Hu**
**PI GRA: Adeel Butt**
**Start Date: Oct 2006**

## 1. Objective/Abstract

The overall objective of this project is to develop a framework for integrating engineering and business decisions. In view of this objective, a robust decision support system is being developed that can be used for multi-objective and multi-disciplinary optimization and sensitivity analysis under uncertainty of oil, gas and petrochemical systems. More specifically, in this quarter, we have extended the applicability of our previously developed Multi-Objective Robust Optimization (MORO) technique by considering both reducible and irreducible interval uncertainty. Since simulation of a chemical processing system can be computationally time consuming, we have also developed a method for integrating online approximation with MORO. Additionally, for our engineering-business decision support system, we are making a new extension: developing an agent based market simulation approach that will help a firm with its long and short term decisions. In this new addition and for demonstration purposes, we plan to simulate a simplified engineering-business decision model for a focal firm, e.g., an ADNOC company, as it competes with a few other firms in a market system. The overall objective is to determine long and short term decisions (e.g., plant settings, product price) that result in a maximum profit for the focal firm. In the next quarter, we plan to extend and integrate an engineering simulation model (previously developed in Aspen HYSYS) with the proposed agent based approach.

## 2. Deliverables for the Completed Quarter

- Conducted preliminary research on extending our recently developed optimization technique to consider both irreducible and reducible interval uncertainties:
  - Developed a preliminary and new MORO approach with both irreducible and reducible uncertainties.
  - Applied the newly developed MORO approach to a few numerical examples for its verification.

- Proposed a simulation model using an agent-based approach for modeling multiple competing petrochemical firms in a market system:
  - Adopted a multinomial logit model to represent customer choices.
  - Developed a preliminary framework for simulating a chemical process-based product in a market system using an agent based approach.

- Improved an engineering simulation model of a reactor-distillation process using Aspen HYSYS:
  - Revisiting the Aspen HYSYS model and ensuring that the reactor-distillation model is robust to process variables variations.
  - Integrating the reactor-distillation model with other process units.

  - Investigating the performance of the integrated reactor-distillation system.

- Progress on recent joint publications:
  - W. Hu, S. Azarm and A. Almansoori, 2010, "Approximation Assisted Multi-objective collaborative Robust Optimization (AA-McRO) under Interval Uncertainty" 13th AIAA/ISSMO Multidisciplinary Analysis and Optimization Conference, Forth worth, TX.
  - Hu, W., M. Li, S. Azarm, S. Al Hashimi, A. Almansoori, and N. Al Qasas, 2010, "On Improving Multi-Objective Robust Optimization Under Interval Uncertainty Using Worst Possible Point Constraint Cuts," *Journal of Mechanical Design* (under review/revision).
  - W. Hu, A. Almansoori, P.K. Kannan and S. Azarm, 2010, "Corporate Dashboards for Multi-Unit Firms: An Agent-Based Approach for Supply Chain Optimization" *Decision Support Systems* (under review).
  - W. Hu, S. Azarm and A. Almansoori, 2010, Approximation Assisted Multi-objective collaborative Robust Optimization (AA-McRO) under Interval Uncertainty (working paper).

## 3. Summary of Project Activities for the Completed Quarter

### Events and meetings of the sixth quarter of Phase II included the following:

A paper titled "Approximation Assisted Multi-objective collaborative Robust Optimization (AA-McRO) under Interval Uncertainty" was submitted and accepted for the 13th AIAA/ISSMO Multidisciplinary Analysis and Optimization Conference. The conference was held at Forth Worth, TX, during September 13-15, 2010. Weiwei Hu and Prof. Azarm attended the conference and presented their joint work on behalf of the PI-UMD research team.

Three teleconference meetings (via SKYPE) were held between PI and UMD project collaborators on September 29, November 4 and November 29. Some of the highlights of those meetings include: (i) review and discussion of research progress from last summer and plans for the fall semester 2010. One of the research plans was to improve the engineering and business simulation models. With respect to improving the engineering model, the focus was on improving the simulation of the reactor-distillation process using Aspen HYSYS. With respect to the business simulation, our previously adopted agent based model was revised by defining a learning behavior for each agent that was representing a market player. (ii) During this quarter the research team welcomed a new member, Mr. Adeel Butt, who is a graduate student working under supervision of Prof. Almansoori at PI. Plans for the next possible PI workshop were discussed. Plans for further investigations on extending a previously developed MORO approach were also considered.

### Research efforts in this quarter included the following:

**Multi-objective Robust Optimization (MORO) with irreducible and reducible interval uncertainties**

Numerical simulation models for a chemical process typically have many input parameters such as operational variables and engineering parameters. Such parameters generally may contain input uncertainties (e.g., variations in temperature, pressure, mixture, etc., in crude oil) which can propagate in the chemical process plant and result in uncertain variations in the outputs. To tackle such problems, we can use MORO to obtain operational variables that are not only optimized but also produce system outputs that are relatively insensitive (or robust) to input uncertainties. In the MORO technique that we developed previously, we assumed that input uncertainties were irreducible. However, the variation range for some uncertain input parameters

may be reducible, particularly when resources or investments are available to collect more information and insights about the uncertain parameters.

As an example, consider the problem of oil exploration in an oil field for the first time. Clearly, as the number of wells in the field is increased, the uncertainty of where the oil is concentrated in the field is decreased. In this regard, one can argue that uncertainty in the field parameters is in general reducible (at least to some degree) and the more we try to understand them by collecting additional information (e.g., additional wells in the field), the less that uncertainty becomes. However, in obtaining such information, there is an associated cost or investment. Specifically, for the purpose of making our point here, we use the following equation to describe the relation between investment and the degree of uncertainty reduction:

$$investment = \theta_1\left(1 - \frac{1}{K}\sum_{k=1}^{K}\alpha_k\right) + \theta_2\left(1 - \prod_{k=1}^{K}\alpha_k\right)$$

where $\theta_1$ and $\theta_2$ are weighing coefficients used for a perimeter measure (first term in the above equation) and an area measure (second term) due to uncertainty reduction. The quantity $\alpha_k$ is the Parameter Uncertainty Reduction Index (PURI) with a range from 0 to 1, and *K* is the total number of uncertain parameters. Figure 1 shows a 2-D description of PURI. The light grey area in Figure 1(a) shows a possible reducible uncertainty range for two parameters with their nominal and extreme values. Suppose we have obtained additional information about the uncertainty of these parameters after making some investment and thus are able to reduce the uncertainty range for these parameters. This reduced uncertainty range is shown in Figure 1 (b). The dark grey area can be taken as the irreducible uncertainty range because we assume this portion of uncertainty cannot be reduced further. To characterize the degree of uncertainty reduction, we use $\alpha_1 \Delta p_1$ and $\alpha_1 \Delta p_1$ to represent the reduced uncertainty range, as shown in Figure 1(b).

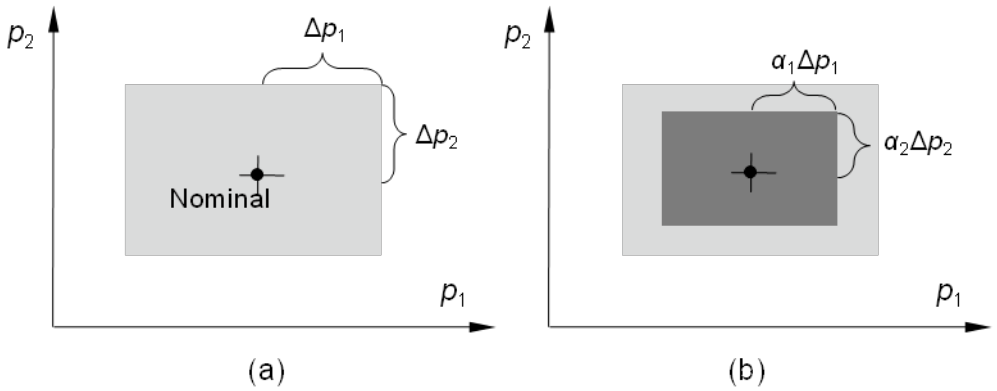


**Figure 1. Definition of reducible uncertainty in a two-dimension uncertainty space.**

With both reducible and irreducible uncertainties presented in the system input, it is important that a formal approach in the assessment of these uncertainties under a MORO framework is established. Figure 2 gives an example of a simulation model. The simulation model generates multiple output values, represented by the objective functions (*f*) and constraints (*g*), where $g \leqslant 0$. The objective in the assessment of reducible and irreducible uncertainties is to ensure that the variations in the objective functions are within an acceptable range. This range is called Acceptable Objective Variation Range (AOVR). Also, the variation in the constraints should not violate feasibility. The idea of assessing uncertain variations in the output functions is represented on the right-hand side of Figure 2, where the variation ranges in both objective functions and constraints for reducible uncertainty are not acceptable. Meanwhile, the extreme points of the variation range in the objective functions and constraints are represented by a Worst Possible Point (as shown by $WPP_f$ and $WPP_g$). The basic idea behind the MORO technique is to ensure that both $WPP_f$ and $WPP_g$ are inside their respective acceptable ranges.

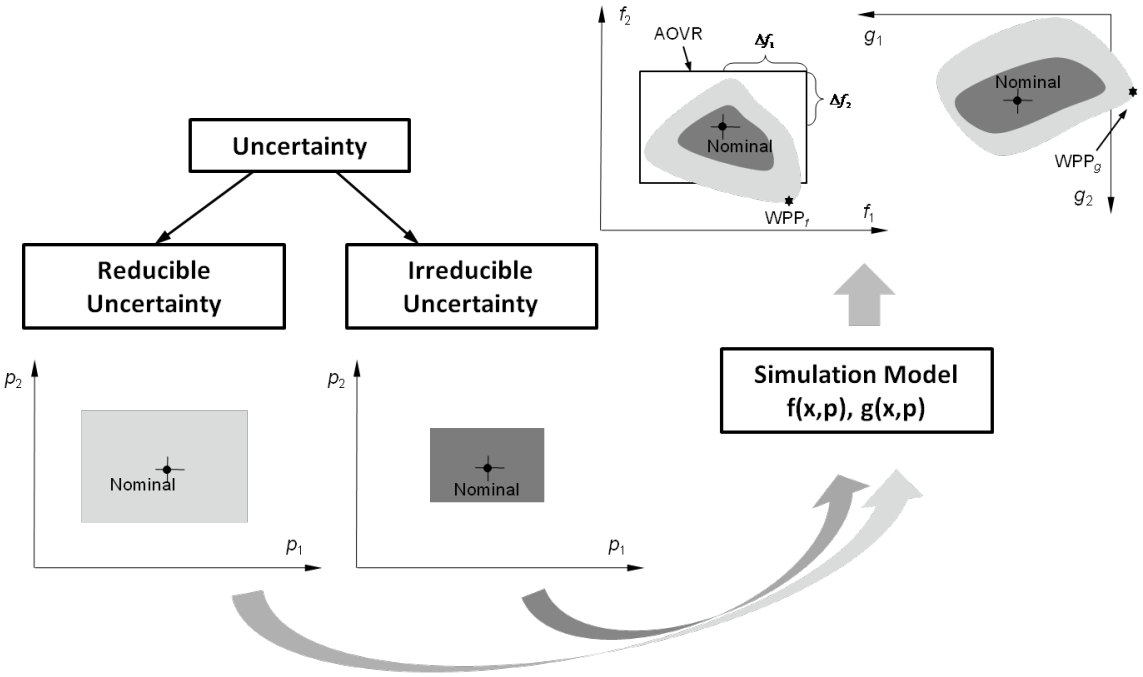


**Figure 2. Assessment of both reducible and irreducible uncertainties in MORO.**

Based on the assessment of both reducible and irreducible uncertainties, we have developed a general MORO framework and applied it to a few numerical examples. We are also planning to integrate our online approximation with this MORO framework. The online approximation collects optimal solution points from MORO as candidate sample points and uses them to build a compact model (or meta-model) that replaces a computationally expensive simulation model. In this way, the accuracy of the meta-models can progressively be improved with a reasonably small number of sampled points. Since the computational time required by a meta-model is much less compared to the actual simulation model, we are expecting that by using approximation we can significantly improve efficiency in applying this new MORO approach. The details of the online approximation assisted MORO with reducible and irreducible uncertainties will be completed and presented in the next quarterly report.

**Agent-based market modeling**

Over the last ten years, wholesale and retail prices for fuel and petrochemical products have risen significantly. This rise in prices is greatly influenced by the crude oil prices. More recently, during the second half of 2010, the price of crude oil in international markets has been in the range of $70-90 per barrel. Despite of the slow pace of recovery in global economies, the overall crude oil price is forecasted to have a rising trend. This explains the rising cost of fuel and petrochemical products but also can reduce the profit margin for producers of these products. It is important for the management of an ADNOC company to make pricing and production decisions on their products based on a careful consideration of the market trends and corresponding uncertainties in order to stay competitive.

We propose the use of agents to represent market players, e.g., producers, customers, and simulate the decisions they make. In this approach, each agent represents a market player (e.g., a firm or customer) and has “intelligence”, i.e., follows real-life rules in making decisions. Also, each agent has a learning behavior; i.e., its future decisions depends on outcome (e.g., profit) of past decisions. Using an agent based approach and following game theory concepts, market equilibrium can be arrived at when no agent would want to deviate from its current decisions; i.e., no agent can be better off in terms of its profit margin by

unilateral deviation. We are planning to investigate a number of scenarios in our agent-based model. One such scenario will consider the impact of a pricing policy for a product by a producer in a market, i.e., how the market will respond and reach an equilibrium based on pricing decisions made by a firm (called the focal firm) and its competing firms. Figure 3 shows an example of an agent-based market model in which a focal firm (e.g., Borouge) competes with a few other firms in a market system that has multiple customer segments with their corresponding customer preferences.

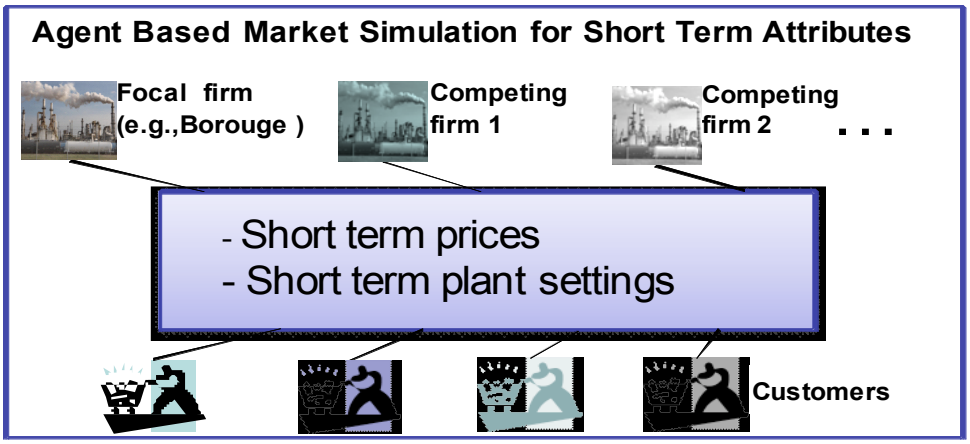


**Figure 3. Agent based market model for multiple competitive refineries.**

In modeling customer agents, a multinomial logit (MNL) choice model [1] can be used to calculate the customer's utility towards a choice of a product produced by a firm. We use $U_{i,j}$ to represent the utility of customer $i$ for product from firm $j$. Particularly, $U_{i,j}$ is composed of two parts as follows:

$$U_{i,j} = \boldsymbol{\beta}_i \bullet \mathbf{X}_{i,j} + \varepsilon_{i,j}, i = 1,2,\ldots,N_i, j = 1,2\ldots,N_j$$

where $\boldsymbol{\beta}_i$ are coefficients denoting the weights for the values of $\mathbf{X}_{i,j}$ and $\mathbf{X}_{i,j}$ is a matrix representing the customer $i$'s attribute levels for product from firm $j$. $\boldsymbol{\beta}_i \cdot \mathbf{X}_{i,j}$ is assumed to be deterministic and $\varepsilon_i$ is a random component. The choice probability $P_i(L)$ for choosing a product from a Firm L is expressed by:

$$P_i(L) = \frac{\exp(\boldsymbol{\beta}_i \cdot \mathbf{X}_{i,L})}{\sum_{j=1}^{N} \exp(\boldsymbol{\beta}_i \cdot \mathbf{X}_{i,j})}$$

We can then calculate the market share for Firm L as:

$$m_L = \sum_{i=1}^{N_i} s_i \cdot P_i(L) = \sum_{i=1}^{N_i} s_i \cdot \frac{\exp(\boldsymbol{\beta}_i \cdot \mathbf{X}_{i,L})}{\sum_{j=1}^{N_i} \exp(\boldsymbol{\beta}_i \cdot \mathbf{X}_{i,j})}$$

where $s_i$ is the market size for customer segment $i$. Using market share, we can obtain profit for a focal and competing firms.

**Relationship between market and engineering decisions: An example model**

In modeling the market interactions using an agent-based approach, we can consider product purity, for instance, as one of the main attributes possibly affecting customer purchase decisions. Each customer may have a specific preference for product purity. Some customers may prefer product with a higher purity while others may not. As mentioned earlier, customer

preference on the product determines the market share and consequently affects product sales and profit. Although seeking a higher purity product might be a good goal, it is not always the best decision to make the product as pure as possible since the production cost can increase, which translates to a higher price and possibly lower profit. On the other hand, product purity is heavily dependent on the plant operational variables and other engineering parameters. Decisions on the operational variables (or engineering decisions) are typically addressed at the engineering level. When making the engineering decisions, it is also important to consider operational and maintenance cost while satisfying engineering constraints. Careful considerations and interplay between various parameters are sometimes ignored when top level management decisions are made. In order to address this problem, in this quarter, we proposed to use a new integrated business and engineering decision support framework in the modeling and optimization.

**Relationship of the agent based approach to the previous integration framework**

It should be noted that the integration framework that we have proposed since the beginning of Phase II can be adopted in the development of the current market and engineering models. However, in our earlier business model, we considered only a single firm and focused on an internal business decision model. In this quarter, we are expanding the previous model and considering multiple competing firms. Therefore, the business model in the previous framework is noticeably different from the model that we are developing now, as shown in Figure 4. The integrated business and engineering framework with the market simulation model we are developing now, Figure 4, is more general and able to provide insightful decision support functions that the previous framework was not.

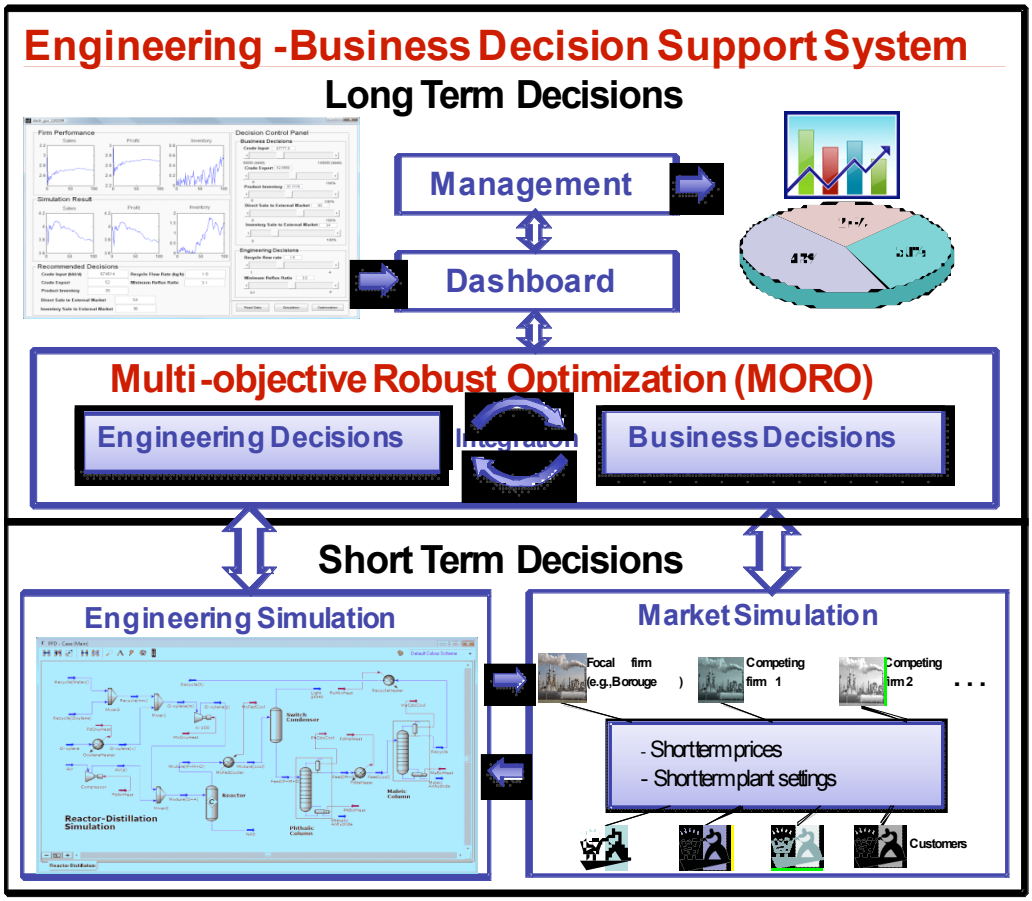


**Figure 4. Decision support system framework.**

## 4. Difficulties Encountered/Overcome

One challenge in the assessment of both reducible and irreducible uncertainties is in determining which uncertain parameter is reducible and which one is irreducible. Although initial study indicates that when a significant amount of information is collected, most uncertain parameters can be considered to be reducible to some extent. It is difficult to identify the uncertainty that investments should be devoted to for collecting information. However, one may also argue that uncertainty for some parameters is not reducible due to the randomness in nature. For example, mixture properties of crude oil have a natural randomness that is irreducible. Therefore, it is critical to identify and categorize uncertainty into reducible and irreducible ones before assessing them. However, this might sometimes be difficult to implement. On the other hand, we have adopted a simple model to quantify the relationship between investment and uncertainty reduction. In reality, this simple model might not necessarily be applicable since the more we reduce uncertainty, the more costly it becomes. We will continue to improve this model as our understanding of the reducible and irreducible uncertainties improves.

## 5. Planned Project Activities for the Next Quarter

- Develop a framework to quantify reducible and irreducible uncertainties for MORO with online approximation.
- Simulate the proposed oil product market using agent based approach in Matlab
- Integrate the new business model in Matlab with Engineering model in Aspen HYSYS in a revised business and engineering integration framework
- Improves the integrated reactor-distillation system by adding complexity to the present process and enhancing its robustness
- Revise dashboard based on the new integrated business and engineering models

# Appendix

## Justification and Background

Many oil, gas and petrochemical systems involve numerous coupled subsystems. These systems and their subsystems usually have uncertain inputs and thus it can be difficult to make the "best" engineering and business decisions in terms of independent operations of these complex systems. It becomes even more difficult to make those decisions when the system consists of many units or plants producing different products. This difficulty presents an opportunity taken on in this project. A review of mainstream literature has revealed that previous models in management of petrochemical systems have been based on either engineering or business decisions but not both. There is a significant gap in the literature as to how these two types of decisions should be devised and integrated. To address this important gap, the focus of this investigation is to develop an integrated robust decision support framework considering both engineering and business models under uncertain conditions. Our overall objective has several underlying research questions, including: (i) how to develop business models that include management decisions in a multi-unit organization and at the same time account for engineering aspects; (ii) how to determine the relative importance and effects of uncertain system and/or subsystem input parameters on subsystem and/or system outputs (e.g., system performance); (iii) how to define a set of metrics, by way of a dashboard, that will serve as a visualization tool to keep track of a company's financial status in view of competition and market systems and provide for easy communication between various levels in the company, and (iii) how to extend our current single-level robust optimization method to multi-subsystem problems and maintain reasonable computational complexity for the method. These underlying questions and corresponding investigations will be organized into tasks throughout the time frame allocated to the project. The details of these tasks are explained in the next section.

## Approach

There are two main tasks in this investigation as detailed in the following.

Task 1 (PI):
Develop and implement engineering analysis models, in a Matlab (or Matlab compatible) environment, for a crude distillation unit case study model.

- Task 1.1: Develop a multi-input multi-output analysis model for a representative petrochemical system with corresponding subsystem analysis models.
- Task 1.2: Extend the analysis model in Task 1.1 to include: (i) additional complexity, (ii) subsystem details and uncertainty to include reasonable representation of engineering side of a plant. The ultimate goal is to develop an integrated multi-subsystem petrochemical analysis model for a plant or a group of units in a plant.

Task 2 (UMD):
Develop and implement a Robust Decision Support System (RDSS).

Engineering Tasks

- Task 2.1: Develop a single level (all-at-once) approximation-assisted robust optimization technique that is able to significantly reduce the computational efforts of making robust decisions.
- Task 2.2: Demonstrate an application of the approach from Task 2.1 with a case study in petrochemical systems which will be developed by PI as a part of Task 1.
- Task 2.3: Develop an approximation assisted multi-objective multi-disciplinary robust optimization approach, which is an extension to Task 2.1.
- Task 2.4: Demonstrate an application of the approach from Task 2.3 with a case study in

petrochemical systems which will be developed by PI as part of Task 1.

Business Tasks

- Task 2.5: Develop business models in Netlogo and/or Matlab and solve a simplified refinery supply chain optimization problem with Matlab.
- Task 2.6: Develop a Dashboard and test the robustness and sensitivity of the Dashboard's elements for the model in Task 2.5.

Integration Tasks

- Task 2.7: Inspect engineering and business problems to determine coupling variables between two problems.
- Task 2.8: Integrate Tasks 2.1 to 2.4 with Tasks 2.5 to 2.6 to formulate a refinery optimization problem that considers both engineering and business objectives and constraints.
- Task 2.9: make the supply chain management problem more realistic by considering more decision levels, more finished products and a wider market, and by increasing the size of the refinery's internal network and then repeat Task 2.8.
- Task 2.10: Verify and validate the integrated model.

## References


[1] Anderson, S. P., Palma, A.d., and Thisse, J., 1992, "Discrete Choice Theory of Product Differentiation", Cambridge, MA, MIT Press, 1992.

[2] Aspen HYSYS, 2009, http://www.aspentech.com, Aspen Technology.

[3] Douglas, J.M., 1988, "Conceptual Design of Chemical Processes", McGraw-Hill, New York, USA.

[4] Forbes, R.J., 1948, "Short History of the Art of Distillation", Brill, Leiden, Holland.

[5] Gargeya, V., 2005, "Plant Level Performance Measurement: An Exploratory Case Study of a Pharmaceutical Encapsulation Company", Technovation, 25(12), 1457-1467.

[6] Gattu, G., Palavajjhala, S., and Robertson, D., 2003, "Are Oil Refineries Ready for Non-Linear Control and Optimization?" International Symposium on Process Systems Engineering and Control, Mumbai, India.

[7] Grossmann, I. E., 2005, "Enterprise-Wide Optimization: A New Frontier in Process Systems Engineering," AIChE Journal, 51(7), p. 1846-1857.

[8] Halemane K. P., Grossmann I. E., 1983, "Optimal Process Design under Uncertainty," AIChE Journal, 29(3), 425-433.

[9] Jackson, J., Hofmann, J., Wassick, J. and Grossmann, I., 2003, "A nonlinear multi-period process optimization model for production planning in multi-plant facilities", Proceedings FOCAPO2003, 281-284..

[10] Janak, L., Lin, X. and Floudas, C. A., 2007, "A New Robust Optimization Approach for Scheduling Under Uncertainty: II. Uncertainty with Known Probability Distribution," Computers and Chemical Engineering, 31(3), 171-195.

[11] Kaplan, R. and Norton, D., 1996, "Using the Balanced Scorecard As a Strategic Management System", Harvard Business Review, 74(1), 75-85.

[12] Kleijnen, J. and Smits, M., 2003, "Performance metrics in supply chain management". Journal of the Operational Research Society, 54(5), 507–514.

[13] Lin, X., Janak, S. L. and Floudas, C. A., 2004, "A New Robust Optimization Approach for Scheduling Under Uncertainty: I. Bounded Uncertainty," Computers and Chemical Engineering, 28(6-7), 1069-1085.

[14] Li, M., and Azarm, S., 2008, "Multiobjective Collaborative Robust Optimization with Interval Uncertainty and Interdisciplinary Uncertainty Propagation," Journal of Mechanical Design, 130(8), pp. 081402-1-081402-11.

[15] Li, M., N. Williams and Azarm, S., 2009, "Interval Uncertainty Reduction and Single-

Disciplinary Sensitivity Analysis With Multi-Objective Optimization," Journal of Mechanical Design, 131(3), pp. 031007-1-031007-11.
[16] Micheletto, S. R., Carvalho, M. C. A. and Pinto, J. M., 2008, “Operational Optimization of the Utility System of an Oil Refinery,” Computers and Chemical Engineering, 32(1-2), 170-185.
[17] Netlogo, http://ccl.northwestern.edu/netlogo/
[18] Pinto, J., Joly, M. and Moro, L., 2000, “Planning and scheduling models for refinery operations”, Computers and Chemical Engineering, 24(9), 2259–2276.
[19] Sahdev, M., Jain, K., Srivastava, P., “Petroleum Refinery Planning and optimization Using Linear Programming”, The Chemical Engineers' Resource Page, http://www.cheresources.com/refinery_planning_optimization.shtml
[20] Simpson, T. W., and Mistree, F., 2001, "Kriging Models for Global Approximation in Simulation-Based Multidisciplinary Design Optimization," AIAA Journal, 39(12), pp. 2233-2241.
[21] Suresh, S. Pitty, Li, W., Adhitya, A., Srinivasan, R., Karimi, A., 2008, “Decision support for integrated refinery supply chains”, Computer and Chemical Engineering, 32, 2767–2786.
[22] Hu, W., M. Li, S. Azarm, S. Al Hashimi, A. Almansoori, and N. Al Qasas, 2009, “On Improving Multi-Objective Robust Optimization Under Interval Uncertainty Using Worst Possible Point Constraint Cuts,” *CD-ROM Proceedings of the ASME International Design Engineering Technical Conferences*, Aug. 30 – Sep. 2, San Diego, CA, USA.

# Dynamics and Control of Drill Strings

**UMD Investigator: Balakumar Balachandran**
**PI Investigators: Hamad Karki and Youssef Abdelmagid**
**GRA: Chien-Min Liao (started in Spring 2007)**
**Other participant: Nicholas Vlajic**
**Start Date: Oct 2006**

## 1. Objective/Abstract

Drill-string dynamics need to be better understood to understand drill-string failures, control drill-string motions, and steer them to their appropriate locations in oil wells. Although a considerable amount of work has been carried out on understanding drill-string vibrations (for example, Leine and van Campen, 2002; Melakhessou *et al*., 2003; Spanos *et al*., 2003; Liao *et al*., 2009), the nonlinear dynamics of this system is only partially understood given that the drill string can undergo axial, torsional, and lateral vibrations, and operational difficulties include sticking, buckling, and fatiguing of strings. In addition, the prior models focus on either bending or torsional or axial motions. Hence, it is important to consider coupled axial-bending-torsional vibrations and contact instability in oil and gas well drilling. A better understanding of these vibrations can help keep the drill string close to the center of the borehole and help realize near-circular bores during drilling operations.

The overall goal of the proposed research is to understand the nonlinear dynamics of the drill string and develop a control-theoretic framework for its stabilization enabling energy efficient drilling with longer life span for the equipment. Specific research objectives of this project are the following: i) building on Phase I efforts, develop and study control-oriented models for the drill strings through analytical and numerical means, ii) investigate the control of an under-actuated nonlinear system (drill string) with complex interactions with the environment, and iii) use the drill-string test-beds constructed at the Petroleum Institute (PI) & the University of Maryland (UMD) to validate the analytical findings and suggest possible strategies to mitigate drill-string failures in fixed and floating platform environments.

## 2. Deliverables for Completed Quarter

- Conducted parametric studies of a drill-string system.
- Examined motions and trajectories of the rotor through experimental and numerical investigations with a reduced-order model.

## 3. Summary of Results

The monitoring of trajectory of a drill-string within a cross-section of the borehole is a useful method to monitor the system dynamics. Using the trajectory as a guide, parametric studies have been conducted and the motions and trajectories of the rotor have been examined through experimental and numerical investigations with a reduced-order model. These studies can help generate systematic information for enhancing drilling operations. Current guidelines for drilling suggests that there may be benefits in operating at low rotational speeds in cases with high friction and that in cases where the drill string has a curved configuration, the rotation speeds need to be carefully chosen to avoid bumping motions. Through the current research effort, system dynamics are examined along with the conditions and bumping motions of the bottom rotor within the borehole.

The rest of this section is organized as follows. In Section 3.1, experimental results are presented and discussed. Following that, in Section 3.2, the numerical results generated by integrating the reduced-order model are presented and compared with experimental results. The influence of the initial position of the rotor is also discussed. In Section 3.3, the new experimental apparatus used to study horizontal drilling configurations is presented, and in Section 3.4, a discussion of the experiment is included.

### 3.1 Experimental Studies

In this section, the experimental arrangement used for studying the drill-string system at different rotational speeds and with different system parameters is presented. Qualitative changes in the system are observed with respect to changes in the following: i) driving speed of motor, ii) magnitude of unbalanced mass attached to the disc, and iii) friction coefficient between the outer shell and the disk at the bottom of the drill string.

#### 3.1.1 Experimental Arrangement

In Figure 1 and Figure 2, the experimental arrangement is presented along with details used for studying the drill-string system for different combinations of the unbalanced mass and coefficient of the contact surface between the bottom disk and the outer shell. On the left-hand side of Figure 41 and Figure 2(a), a string with a bottom disc is illustrated. This system is driven by a motor with a constant rotating speed that ranges from 40 rpm (revolutions per minute) to 190 rpm. Generally, real field drill systems are driven at speeds under 300 rpm, and most of these drilling speeds are studied here. Five different levels of unbalanced mass attachments to the disc are used, and the corresponding masses are 0.0 grams, 28.1 grams 48.1 grams, 61.7 grams, and 87.1 grams. The unbalanced mass may be viewed as being representative of the curvature of the drill string. For instance, the case of zero unbalanced mass corresponds to a straight drill string, while a non-zero unbalanced mass is representative of a drill string in a curved orientation. Due to changes in soil type and rock conditions with respect to the mine-hole depth, the friction coefficient of between a drill bit and the borehole changes during the course of an operation. For mimicking the physical conditions of “real drilling” and better understanding the system dynamics, three different levels of friction coefficients were considered. The details of the bottom disc with outer shell are shown in Figure 2(c).

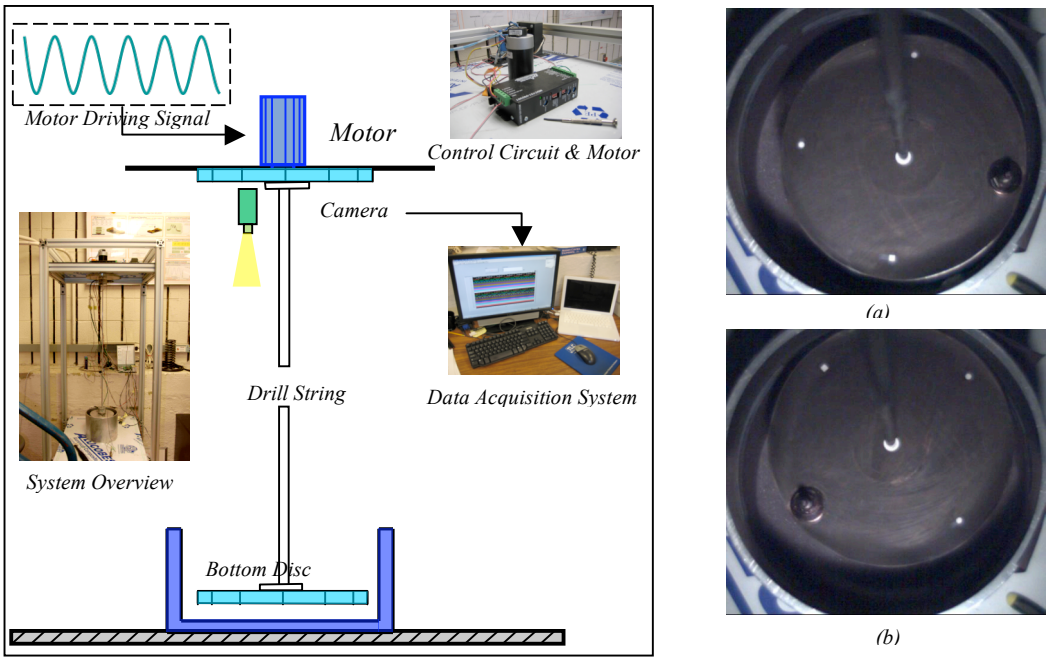


**Figure 1. Experimental setup and procedure.**

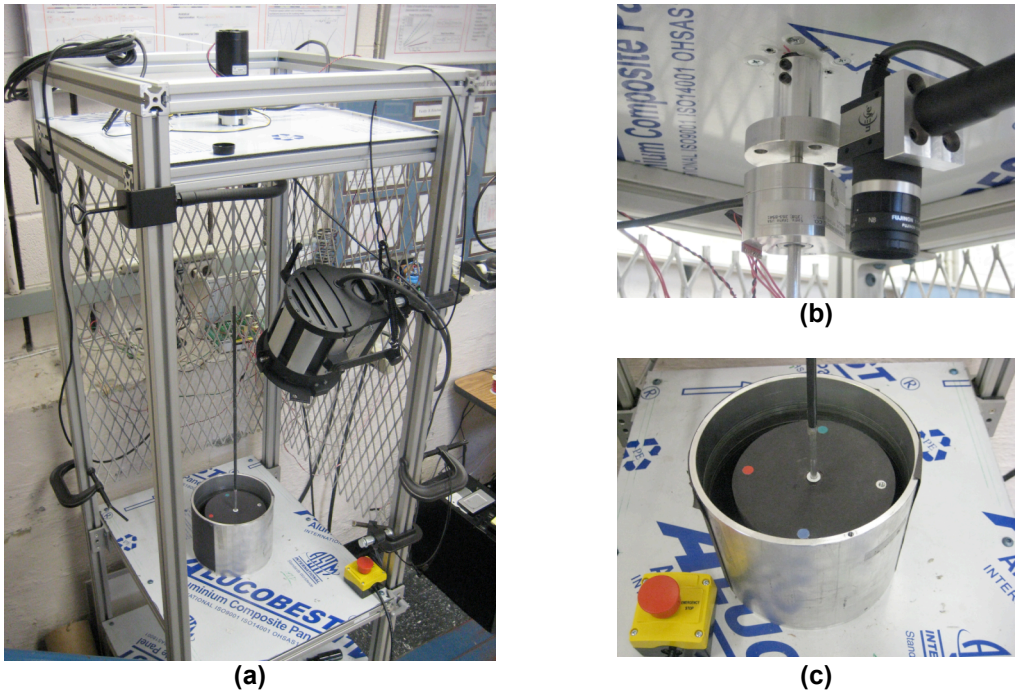


**Figure 2. Experimental setup with details: (a) system overview, (b) camera and encoder, and (c) test platform: disc with outer shell.**

The images of the bottom rotor, which were captured using a video camera, are shown in Figure 2(b). These images were used for monitoring the system response in the experiments. Rotor trajectories were traced and constructed by analyzing the location of center of rotor in each video frame, through a gradient based image processing procedure. An example of a typical image of

the rotor as seen from the camera is shown on the right-hand side of Figure 1. The rotor motions can be clearly seen as one goes from Figure 1(a) to Figure 1(b); the rotor is at a 3 0'clock position within the shell region in (a) and at a 12 o'clock position in (b). The capture rate from the camera is 110 FPS (frame per second), which is sufficient for capturing the response excited by over the range of rotation speeds, which extend up to a maximum rotating speed of 190 rpm.

### 3.1.2 Experimental Results

Rotor trajectories were traced and constructed by analyzing the position of the rotor within each frame of the video, and the obtained results are presented in Figure 3(b) through Figure 3(d). After collecting all the results obtained for the different driving speeds, a diagram of qualitative changes was constructed by sampling the rotor's radial position, with the drive speed serving as the clock frequency. Each intersection with the chosen Poincaré section is shown as a black dot in this diagram, and this location corresponds to the rotor position at a certain time. Such diagrams can be used to understand the system response for a variety of driving speeds; for instance, when the rotor trajectory is erratic, as seen in Figure 3(b) for a drive speed of 79 rpm, the intersections are spread out in case (b) of Figure 3(a). On the other hand, for a regular trajectory such as that shown in Figure 3(d), the corresponding intersections are grouped together. Furthermore, the grouping of the intersections is also indicative of the region in which the motions occur. For instance, in case (c) of Figure 3(a), the motions occur close to the center of the outer shell.

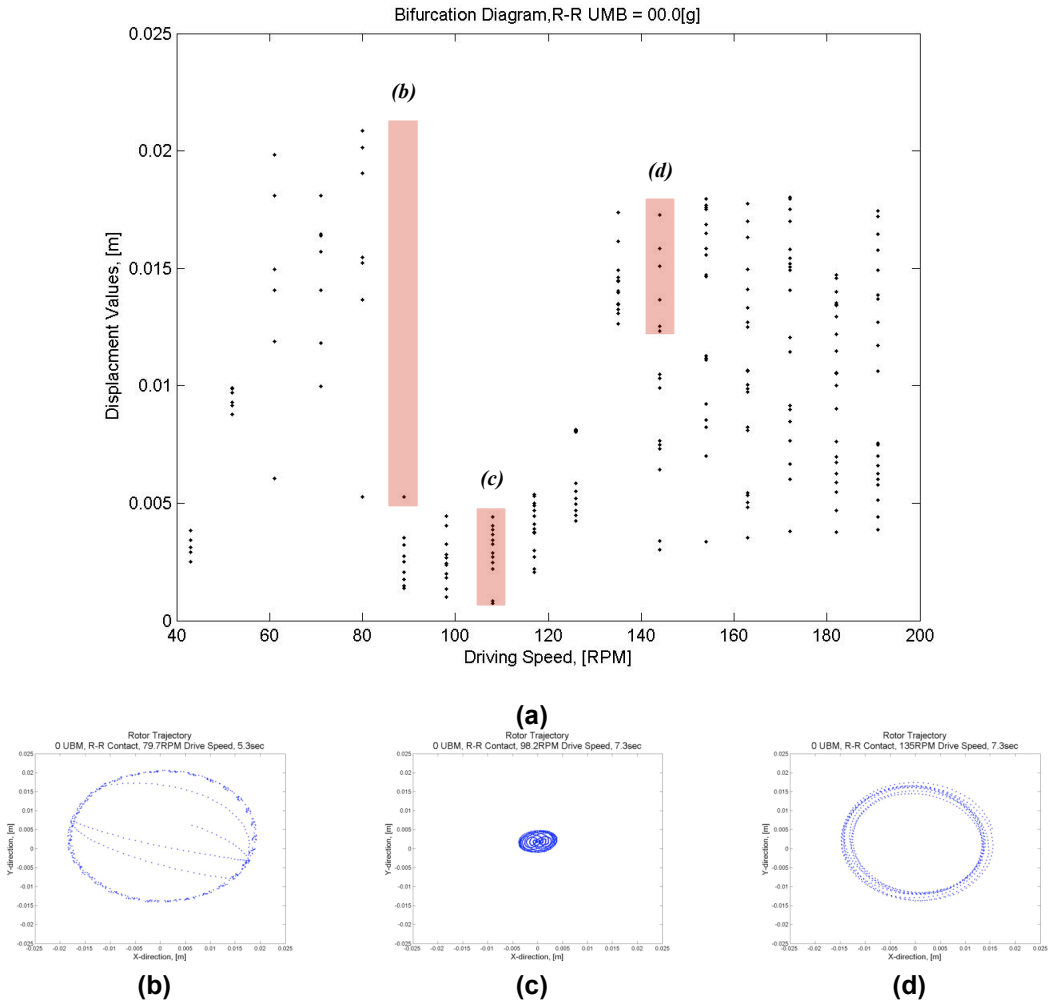


**Figure 3. Illustration of qualitative changes with respect to drive speed.**

The effect of different friction coefficients between the two contact surfaces is illustrated in Figure 4 and Figure 5. In Figure 4, diagrams of qualitative changes obtained for different levels of unbalanced mass, with rubber placed on the outer edge of the bottom rotor, are presented. The rubber-aluminum interface between the rotor and the outer shell are used to create high friction levels representative of what may be encountered in "real" drilling operations. Generally, the rotor moves in an orbital motion at low drive speeds. With increase in the drive speed, the rotor starts moving across the whole shell cross-sectional area, which can be clearly seen for the case with 120 rpm drive speed and 81.3 gram unbalanced mass shown in Figure 4(e). At higher driving speeds, for example, at the drive speed of 130 rpm, the rotor behavior becomes regular, as seen in Figure 4(e). At the highest driving speed, the rotor again behaves erratically, with its trajectory meandering across the shell cross-sectional area again. In short, the rotor moves in a regular orbit at low speeds, and follows an erratic orbit followed by a regular orbit at intermediate speeds before returning to erratic motions at high speeds.

Similar behavior is observed for the rubber-rubber contact surface case of Figure 5. However, when the rotor makes contact with the outer shell, the erratic motions are more pronounced in this case.

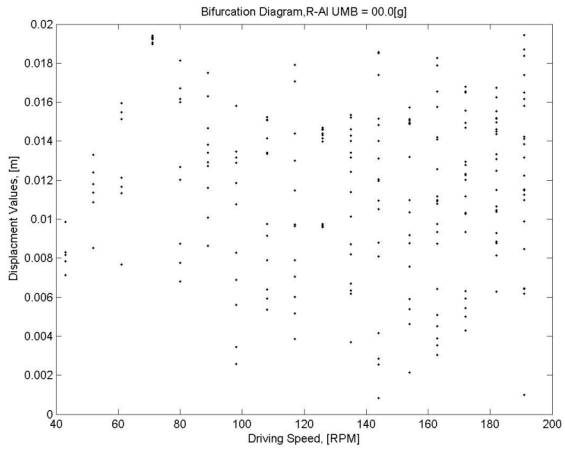


(a)

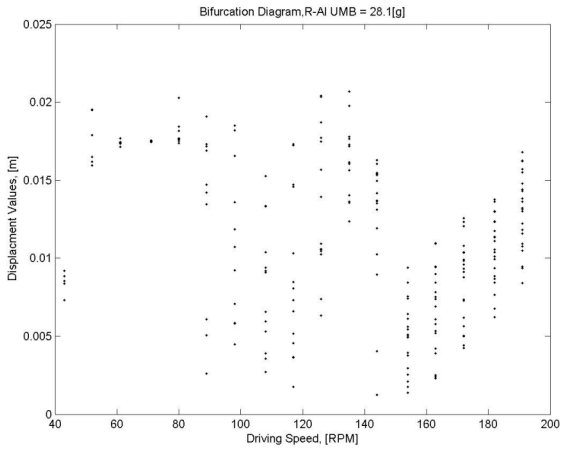


(b)

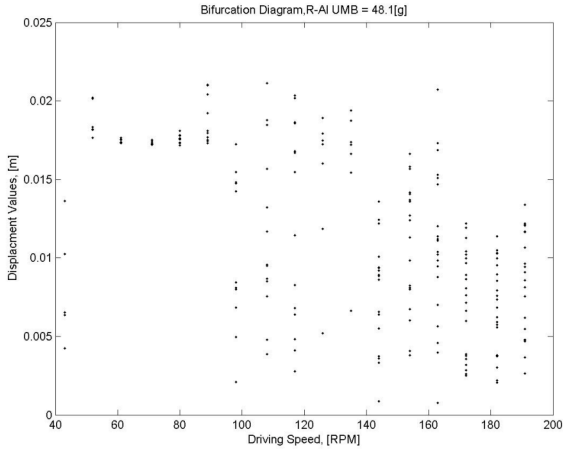


(c)

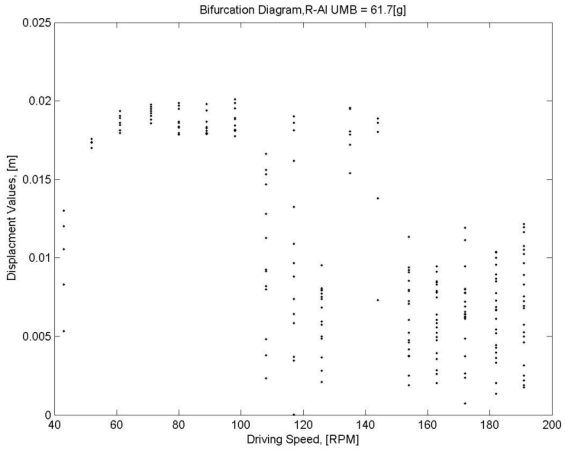


(d)

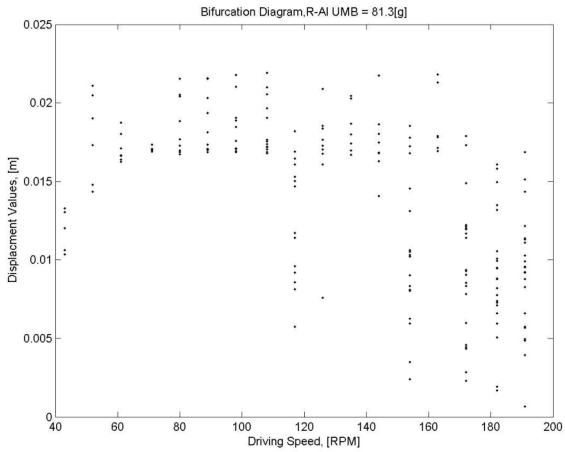


(e)

**Figure 4. Diagram of qualitative changes for different levels of unbalanced mass and rubber-aluminum surface interaction: (a) UMB=0.0 grams, (b) UMB=28.1 grams, (c) UMB=48.1 grams, (d) UMB=61.7 grams, and (e) UMB=81.3 grams.**

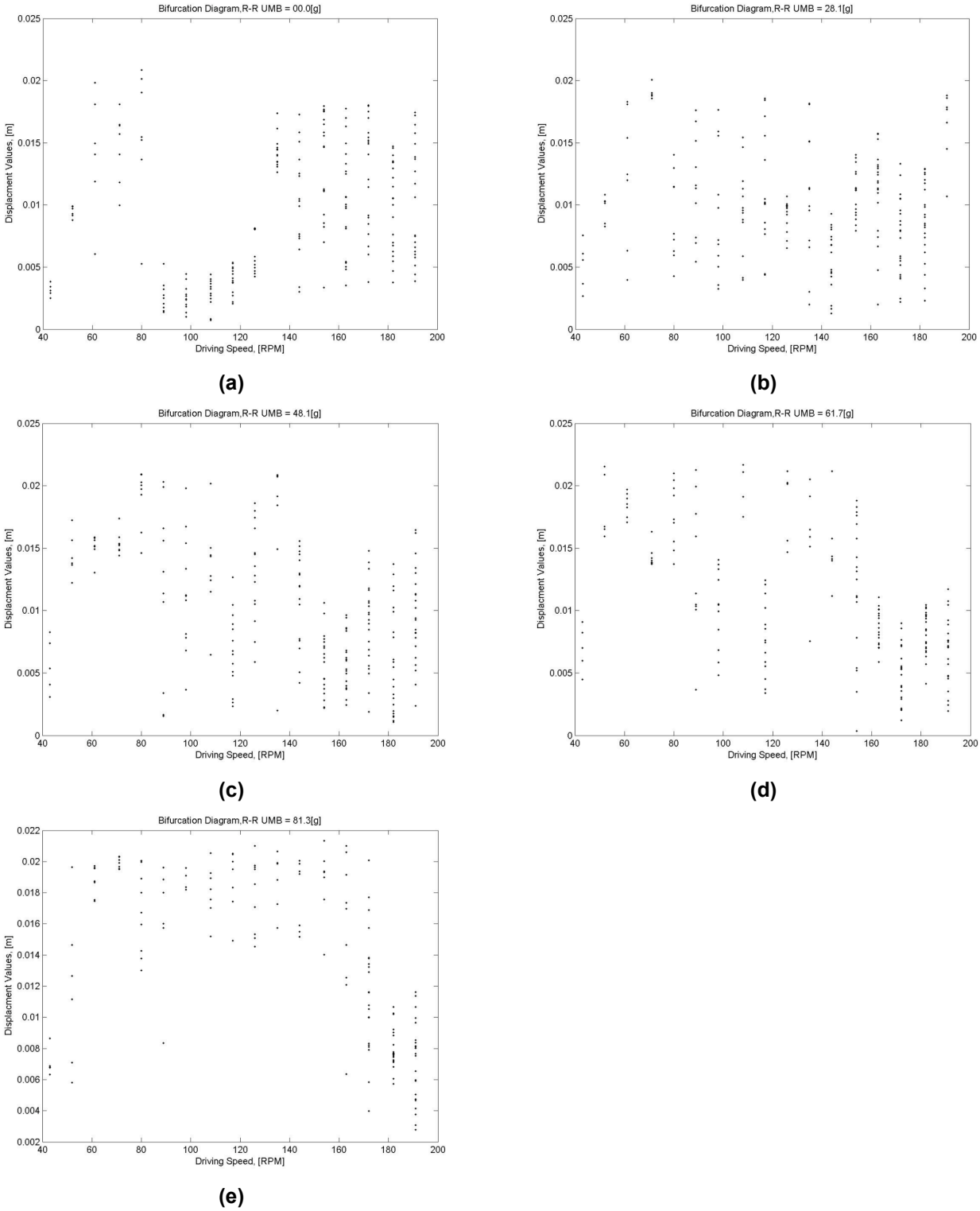


**Figure 5. Diagram of qualitative changes for different levels of unbalanced mass and rubber-rubber surface interaction: (a) UMB=0.0 grams, (b) UMB=28.1 grams, (c) UMB=48.1 grams, (d) UMB=61.7 grams, and (e) UMB=81.3 grams.**

### 3.2 Numerical Investigations

In this section, numerical predictions made by using a model discussed in previous reports are compared with the experimental data. The previous four-degree-of-freedom model can be cast in three-degree-of-freedom form when the drive speed is constant, which is equivalent to adding a constraint to the four-degree-of-freedom system. The equations of motion of the three-degree-of-freedom model are shown in Equations (1) to (3)

$$(m+m_b)\ddot{\rho}-(m+m_b)\rho(\Omega+\dot{\phi})^2+K_r(\rho-\rho_0)$$
$$+\lambda K_p(\rho-\delta)+K_t\rho\phi^2-em_b(\ddot{\alpha}\sin(\beta)+\dot{\alpha}^2\cos(\beta))=0 \quad (1)$$

$$(m+m_b)\rho\ddot{\phi}+2(m+m_b)\dot{\rho}(\Omega+\dot{\phi})+K_t\rho\ \phi$$
$$-em_b\left[\dot{\alpha}(\dot{\alpha}+\Omega)\sin(\beta)-\ddot{\alpha}\cos(\beta)\right]=-\lambda F_t \quad (2)$$

$$(I_2+m_be^2)\ddot{\alpha}+K_{tor}(\alpha-\Omega t)+em_b[-\ddot{\rho}\sin(\beta)+\rho\ddot{\phi}\cos(\beta)$$
$$+\rho\dot{\phi}(\Omega+\dot{\phi})\sin(\beta)+\dot{\rho}(\Omega+2\dot{\phi})\cos(\beta)]=M_{ext}-\lambda F_tR \quad (3)$$

In the equations listed above, $\Omega$ is the constant motor driving speed in radians per second. Considering stick-slip interactions as in the previous reports, numerical results are obtained by integrating the above equations for the system parameter values corresponding to the experimental arrangement of prior reports.

#### 3.2.1 Numerical Results and Comparisons with Experimental Data

Experimental and numerical results are presented in Figure 6. Comparing the numerical and experimental results for a high level of unbalanced mass and with moderate value of the coefficient of friction, certain observations can be made: i) the rotor motion shows similar behavior, such as the transition from a regular orbit to an erratic one, as the drive speed is increased and ii) the rotor returns to a regular orbit at high rotating speeds. In the experiments, the transition from regular to irregular motions is observed at 120 rpm, while in the simulations, this transition is observed at 140 rpm.

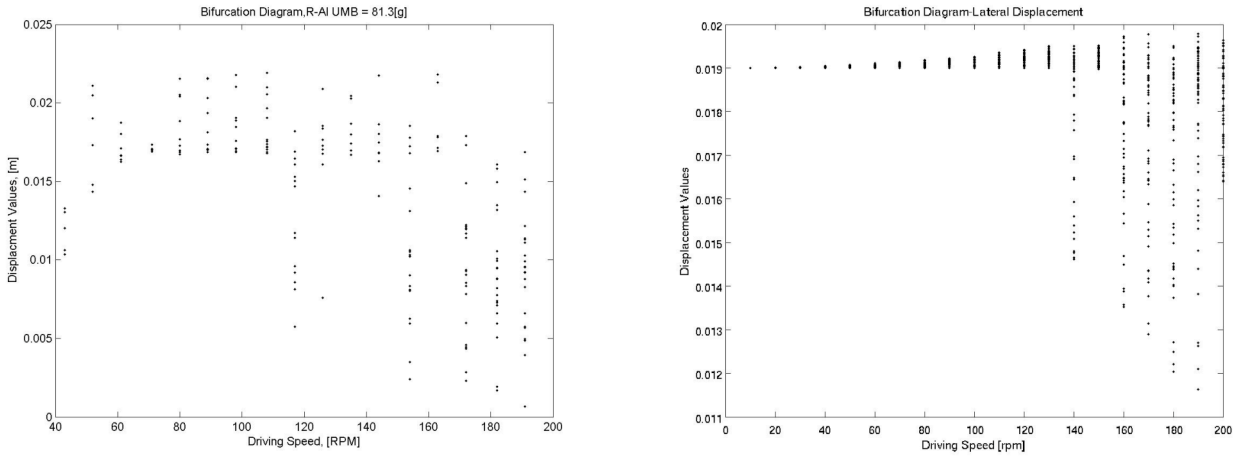


(a) (b)

**Figure 6. Comparisons of qualitative changes: (a) experimental results and (b) numerical predictions.**

### 3.2.2 Numerical Studies for Different Initial Positions

Rotor trajectories are shown in Figure 7 and Figure 8 to illustrate the influence of the initial rotor position of rotor for different driving speeds. When the rotor is near the center (origin) of the shell region, it has less chance of contacting the outer shell. In Figure 7, the numerically determined rotor trajectories for an initial position close to the center are shown. For a fixed initial position, as the levels of unbalanced mass and driving speed are increased, the rotor response level increases and the rotor trajectories also become irregular. On the other hand, if the initial position is varied to bring the initial rotor position close to the edge of shell region, a minor disturbance can bring the rotor into contact with the shell. With contact, the rotor response can take different forms. When the drive speed is low, the rotor moves around the shell; however, at high drive speeds the rotor shows bumping motions, as seen in Figures 8(a), (c), and (e). For increasing levels of unbalanced mass, the amplitude of rotor bumping is decreased, as noted from Figures 8(b), (d), and (f).

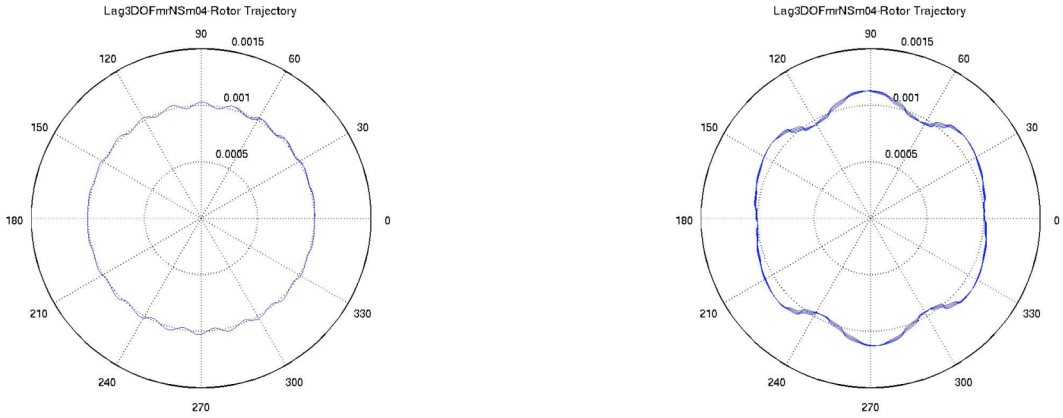


(a) (b)

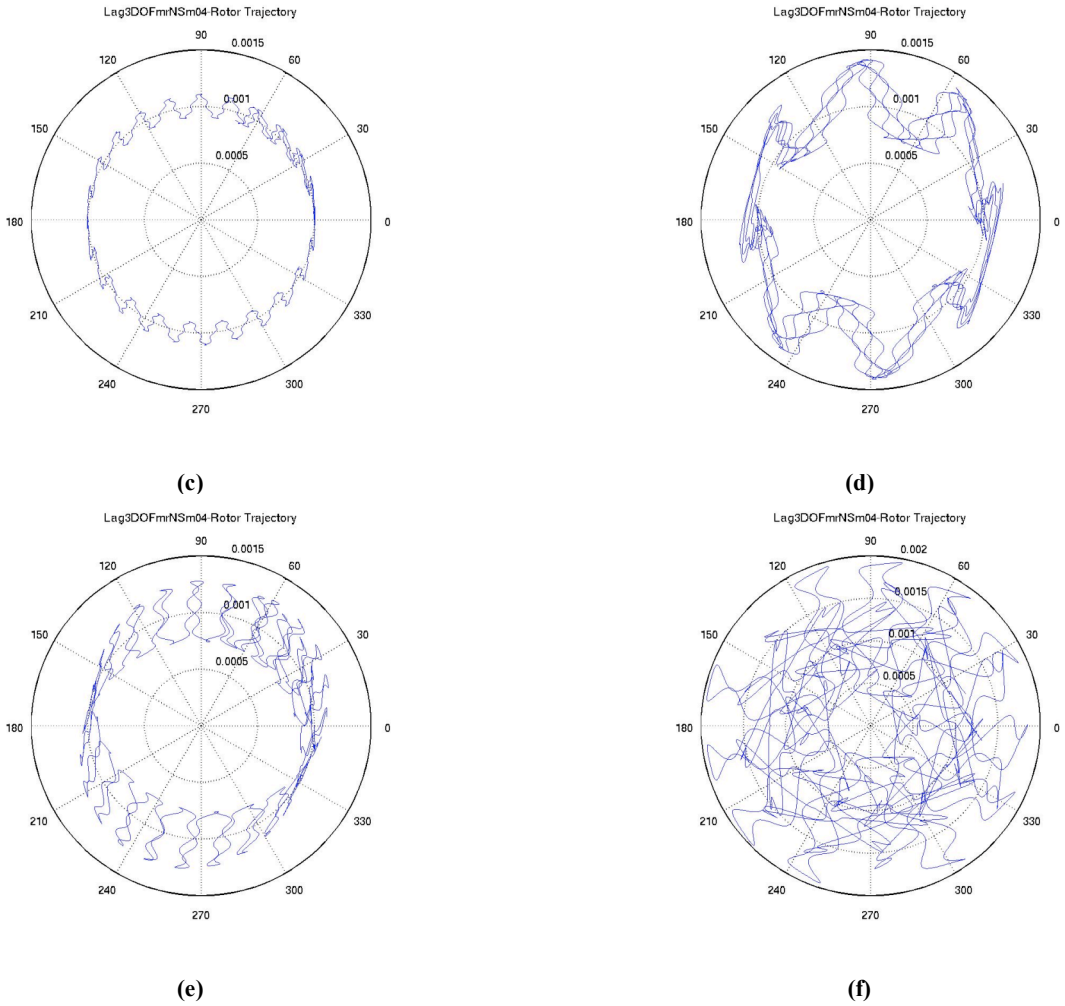


**Figure 7. Rotor trajectories initiated from center for different levels of unbalanced mass and driving speed: (a) UMB=0.0 grams and speed =50 rpm, (b) UMB=0.0 grams and speed =200 rpm, (c) UMB=30.0 grams and speed = 50 rpm, (d) UMB=30.0 grams and speed = 200 rpm, (e) UMB=80.0 grams and speed = 50 rpm, and (f) UMB=80.0 grams and speed = 200 rpm.**

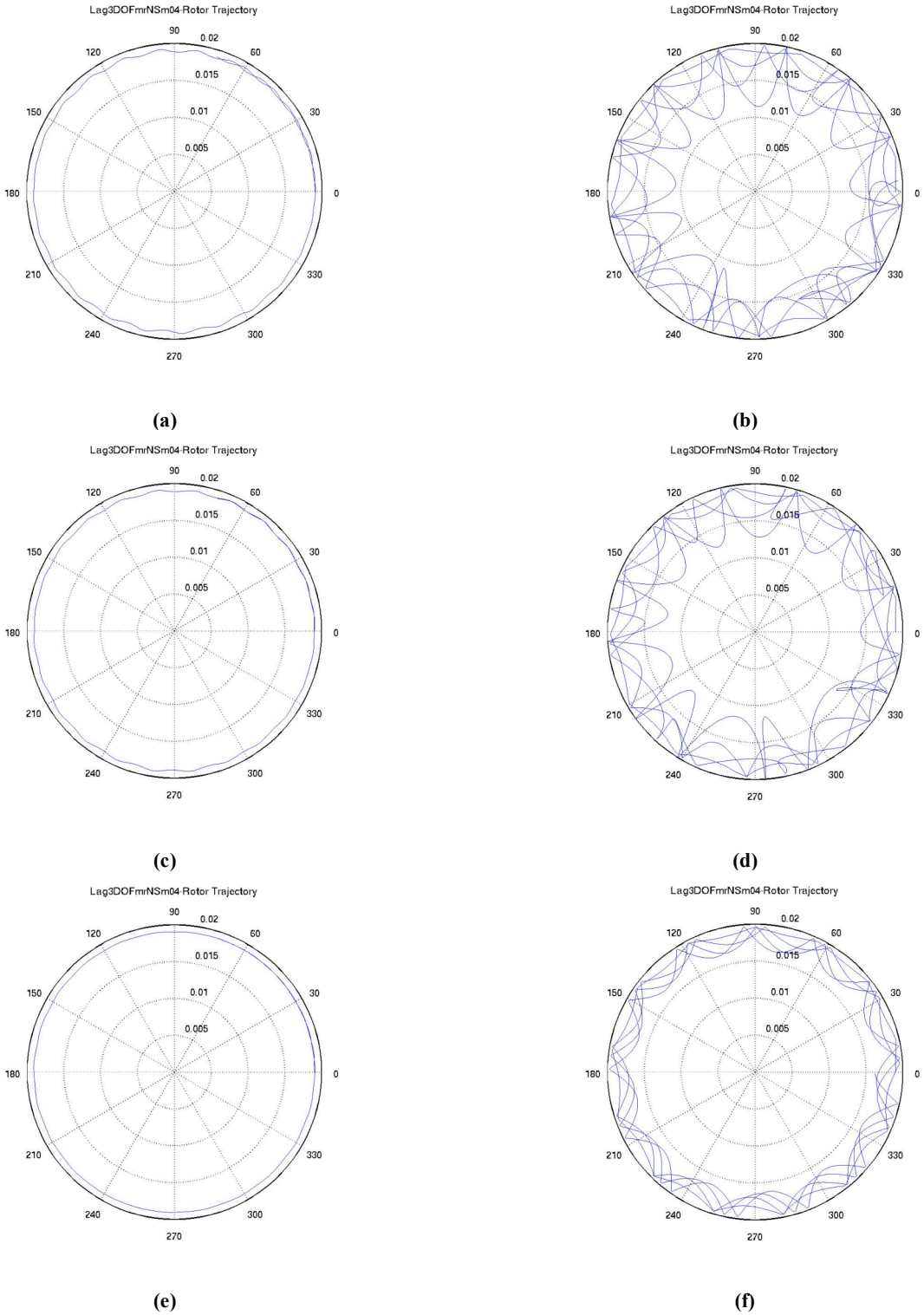


**Figure 8. Rotor trajectories initiated from edge for different levels of unbalanced mass and driving speed: (a) UMB=0.0 grams and speed =50 rpm, (b) UMB=0.0 grams and speed =200 rpm, (c) UMB=30.0 grams and speed = 50 rpm, (d) UMB=30.0 grams and speed = 200 rpm, (e) UMB=80.0 grams and speed = 50 rpm, and (f) UMB=80.0 grams and speed = 200 rpm.**

### 3.3 Experimental Setting for Horizontal Drilling

The previous experiments have primarily focused on a small portion of a vertically configured drill string, and different magnitudes of unbalanced mass were used to replicate the dynamics of a curved drill string. In the next proposed experiment, the focus is to be on the dynamics of a drill string used to bore curved and horizontal wells. The experimental apparatus is shown in Figure 9. An aluminum rod, which is approximately 1.6 mm in diameter and roughly 3.7 m in length, is used to replicate a drill string. The entire string can be seen in Figure 9(a). The string is driven by a motor at one end, and a sensor between the motor and shaft records the actuation torque. This top apparatus is shown in Figure 9(b). The entire drill string is place inside an acrylic tube, which mimics the borehole. A photograph of the drill string and shaft hub, which replicates the stabilizer collars on actual drill strings, inside of the acrylic tube is shown in Figure 9(c).

Experimental data are to be gathered through several means. The top driving apparatus has been designed so that a slip ring may be retrofitted after the torque sensor. The slip ring can allow for sensors to be attached directly to the string, such as resistive strain gauges or piezoelectric sensors, which can be used to measure local strains and vibrations at the bottom of the string, as well as along the curved section of the string. Furthermore, video cameras will be able to determine the position of the string within the acrylic tube. A gradient based edge detection technique similar to what has been used in the vertical experimental configurations will be used to post-process the video data.

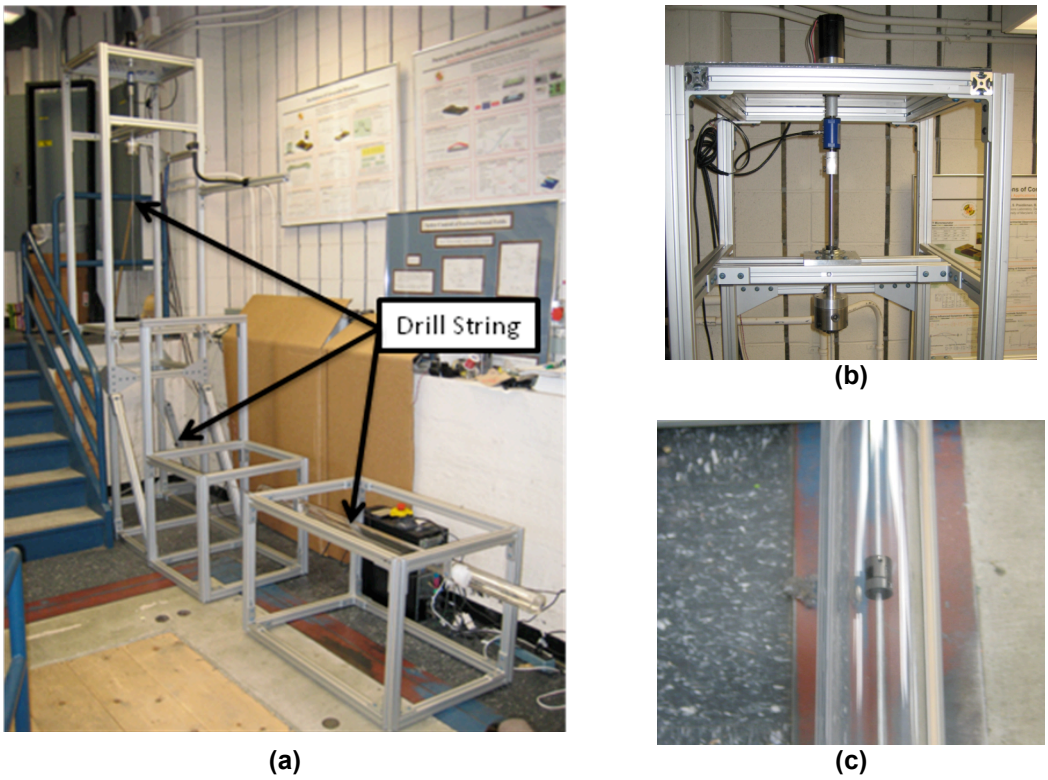


**Figure 9. horizontal drilling experimental apparatus: (a) drill string in horizontal configuration, (b) driving motor and torque sensor at string top, and (c) drill string and stabilizer in acrylic housing.**

## 3.4 Discussion and Future Work

Parametric studies of a drill-string system have been conducted and the results have been detailed within the report. The rotor exhibits regular orbital motions at low driving speeds but this behavior becomes irregular with increase of the drive speed in a moderate speed range. For higher speeds, the rotor is seen to return regular orbital motions, before it reverts back to irregular motions at the highest end of speeds used in the present studies. This complex behavior has been observed in experiments and numerical simulations. The initial rotor position is also an important determinant of the rotor motions, due to the contact between the rotor and the outer shell. The influence of the level of the unbalanced mass and the coefficient of friction has also been studied in this work.

After obtaining an understanding of the complex dynamics of a drill string in a vertical direction, the research is currently moving in the direction of horizontal drill strings with aspect ratios close to those of “real” drill strings. Future reports are to contain findings and results pertaining to horizontal drilling studies.

## Appendix

### Approach

A combined analytical, numerical, and experimental approach is being pursued at the University of Maryland and the Petroleum Institute. Specifically, the drill string is being modeled as a reduced-order nonlinear dynamical system. Appropriate attention is also to be paid to the interactions with the environment. The experiments at UMD and PI are tailored to address specific aspects of the drill-string dynamics as well as complement each other. Actuator and sensor choices are also to be explored to determine how best to control the system dynamics, in particular, through the control rpm. The studies will be initiated with drill strings located on fixed platforms, and later extended to systems located on floating platforms.

### Three-Year Schedule

*Phase II:*

January 1, 2009 to December 31, 2009: Carry out quantitative comparisons between experimental results and predictions of reduced-order models for open-loop studies; understand stick-slip interactions and explore continuum mechanics based drill-string models for fixed platform environments; examine different configurations including horizontal drilling

January 1, 2010 to December 31, 2010: Construct control schemes; carry out experimental, analytical, and numerical studies; and identify appropriate schemes; study horizontal drilling configurations through experiments and analysis

January 1, 2011 to December 31, 2011: Continue horizontal drilling studies; carry out experiments, analysis, and numerical efforts and also examine drill-string operations in off-shore environments

January 1, 2012 to May 1, 2012: Compile results obtained for drill-string operations in vertical and horizontal configurations and provide guidelines for enhancing operations.

### References


[1] Akgun, F. 2004, "A Finite Element Model for Analyzing Horizontal Well BHA Behavior," J. of Petrol. Sci & Eng., Vol. 42, pp. 121-132.

[2] Bednarz, S., 2004, "Design and Exploitation Problems of Drill Strings in Directional Drilling," Acta Montanistica Slovaca, Vol. 9, pp. 152-155.

[3] Downtown, G., 2009, "*New Directions in Rotary Steerable Drilling*", Oilfield Review, pp. 18-29.

[4] Leine, R. I., van Campen, D. H., and Keultjes, W. J. G. (2002). "Stick-Slip Whirl Interaction in Drill String Dynamics," *ASME Journal of Vibration and Acoustics*, Vol. 124 (2), pp. 209-220.

[5] Liao, C.-M., Balachandran, B., and Karkoub, M., (2009). "Drill-String Dynamics: Reduced Order Models," To appear in Proceedings of ASME IMECE 2009, Nov. 13-19 Lake Buena Vista, FL, USA, 2009; Paper No. IMECE2009-10339.

[6] Melakhessou, H., Berlioz, A., and Ferraris, G. (2003). "A Nonlinear Well-Drillstring Interaction Model," *ASME Journal of Vibration and Acoustics*, Vol. 125, pp. 46-52.

[7] Mihajlović, N., van Veggel, A. A., van de Wouw, N., and Nijmeijer, H. (2004) "Analysis of Friction-Induced Limit Cycling in an Experimental Drill-String System," *ASME Journal of Dynamic Systems, Measurement, and Control*, Vol. 126(4), pp. 709-720.

[8] Mihajlović, N., van de Wouw, N., Rosielle, P.C.J.N., and Nijmeijer, H. (2007) "Interaction between torsionalal and lateral vibrations in flexible rotor systems with discontinuous friction," *Nonlinear Dynamics*, Vol. 50, pp. 679-699.

[9] Nayfeh, A. H. and Balachandran, B. (1995). *Applied Nonlinear Dynamics: Analytical, Computational, and Experimental Methods*, Wiley, New York.
[10] Spanos, P. D., Chevallier, A. M., Politis, N. P., and Payne, M. L. (2003). "Oil and Gas Well Drilling: A Vibrations Perspective," *Shock and Vibration Digest* Vol. 35(2), pp. 85-103.
[11] Short, J. A. "Introduction to Directional and Horizontal Drilling " Pennwell Pub, 1993.
[12] Singh, S.P. and Balachandran B. (2009). "Rolling Rub Translations of a Flexibility Connected Disk," pre-print.

# Studies on Mobile Sensor Platforms

**UMD Investigators: Balakumar Balachandran, Nikil Chopra**
**GRAs: Rubyca Jaai**
**PI Investigator: Hamad Karki, Sai Cheong Fok**
**GRAs: Hesham Ishmail (ADNOC Fellow)**
**Start Date: April 2009**

## 1. Objective/Abstract

Mobile sensor platforms can be employed in a variety of operations including environmental and structural health monitoring operations in harsh and remote environments. The overall objective of this project is to carry out a combined analytical, numerical, and experimental effort to develop mobile sensor platforms and appropriate simultaneous localization and mapping (SLAM) algorithms for cooperative sensor platforms to operate autonomously in a harsh environment. Research objectives are the following: i) develop SLAM algorithm-based platforms taking into account system constraints such as constrained communication, the type of sensors considered, allowable dynamics, and factors such as sensor failures and reliability of the considered sensors and ii) carry out experimental and supporting simulation studies by using mobile platform test platforms at the University of Maryland and the Petroleum Institute.

## 2. Deliverables for Completed Quarter

- The EKF algorithm and numerical results are presented.
- The experimental arrangement proposed in the previous report has been constructed to test the SLAM algorithms.

## 3. Summary of Results

The results on the EKF algorithm studied are presented in Section 3.1 and the associated numerical results are given in Section 3.2. The development of the experimental arrangement is discussed in Section 3.3.

### 3.1 Extended Kalman Filter-based SLAM

It is assumed in this report that the mobile agent has the kinematics shown in Eq. (1), which in the state space form is the system model, X(k)=f(X(k-1),U(k-1),w(k-1), as shown in Eq. (2).

$$\begin{aligned} \dot{x} &= V\cos\phi \\ \dot{y} &= V\sin\phi \\ \dot{\phi} &= V\tan\gamma / L \end{aligned} \tag{1}$$

$$X_r(k)=f(X_r(k-1),\ U(k-1),w(k-1)) = \begin{bmatrix} x(k) \\ y(k) \\ \phi(k) \end{bmatrix} = \begin{bmatrix} x(k-1)+\Delta tV(k-1)\cos\phi(k-1) \\ y(k-1)+\Delta tV(k-1)\sin\phi(k-1) \\ \phi(k-1)+\Delta tV(k-1)\tan\gamma(k-1)/L \end{bmatrix} + w(k-1) \tag{2}$$

Here, $X_r$ is the vector of robot pose represented by its position (x,y) and the heading angle □ . The control input U is given by the input velocity V and steering angle γ (see Figure 1 for illustration). The input noise is represented by w(k). The range and bearing measurements obtained by the mobile sensor platform with respect to the ith landmark are also affected by noise. The range and bearing measurements are related to the mobile platform pose and landmark position as shown in Eq. (3).

The observed landmark $F_i$ is added to the state vector and assumed to be stationary. Hence, the state vector X grows in size with every new landmark observed. The measurement model H is given by Eq. (3).

$$z_i(k) = (r_i(k), \theta_i(k)) = H(x(k), v(k))$$

$$r_i(k) = \sqrt{(x_i - x_r(k))^2 + (y_i - y_r(k))^2} + v_r(k)$$

$$\theta_i(k) = tan^{-1}\frac{y_i - y_r(k)}{x_i - x_r(k)} - \phi(k) + v_\theta(k) \qquad (3)$$

where $r_i$ and $\theta_i$ represent the range and bearing measurements for landmark $F_i$ whose position is given by $(x_i,y_i)$. $v_r$ and $v_\theta$ are the noise in the range and bearing measurements, respectively.

The EKF SLAM algorithm implementation includes a recursive prediction step and a measurement update step. The prediction step is implemented by using the system model to estimate at every time step k-1, the system state at time k based on the control input at time k-1.

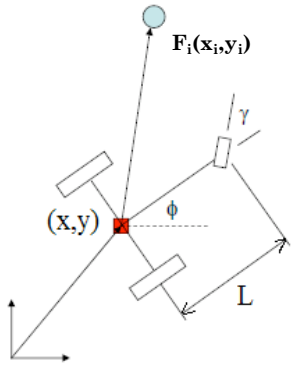


**Figure 1. Schematic of mobile platform and landmark. Vector (x,y,□) represents the pose of the mobile platform at any given time and vector $F_i$ $(x_i,y_i)$ represents the position of the $i^{th}$ landmark.**

Measurement updates are then carried out with every observation z(k) by using the measurement model. Uncertainty in the estimates of the system state caused by noise in the system model as well as the measurements is captured by the covariance matrix P. Further, the EKF algorithm requires an initial estimate or assumption to be made regarding the state vector and covariance matrix at time 0. Typically, the initial state vector is assumed to consist only of the mobile platform's initial pose, as no landmarks are known *a priori.*

Prediction step:

$$\hat{x}(k)^{-} = f(\hat{x}(k-1), u(k-1))$$
$$P(k)^{-} = F(k)P(k-1)F(k)^{T} + W(k)Q(k-1)W(k)^{T} \quad (4)$$

Measurement update step:

$$\hat{x}(k) = \hat{x}(k)^{-} + K(k)(z(k)^{-} H(k))$$
$$P(k) = I - K(k)J_{h}(k)P(k)^{-}$$

where K is the Kalman gain given by

$$K(k) = P(k)^{-} J_{h}(k)^{T} (J_{h}(k)P(k)^{-} J_{h}(k)^{T} + V(k)R(k)V(K)^{T})^{-1} \quad (5)$$

and F(k) is the Jacobian of f with respect to (x,y, φ), W(k) is the Jacobian of f with respect to w and $J_h(k)$ is the Jacobian of H with respect to the full state vector X (which is the vector of the mobile platform pose and all the landmark positions observed until the time step k). The state vector X and the covariance matrix P at any given time represent the current estimate of the map (with the position of the mobile platform within the map) and the associated uncertainty (modeled as a Gaussian with covariance matrix P).

### 3.2 Numerical studies

The algorithm shown in the previous section is used to carry out SLAM by using point landmarks. The mobile platform's kinematics are assumed to be of the form shown in Eq. (1). In this study, the range and bearing measurements are assumed to be obtained by using sensors with limited range with additive Gaussian noise. It has been assumed that the point landmarks are all uniquely identifiable, and therefore further processing to determine data association is not required. In Figure 2, the path taken by the mobile platform and the positions of the point landmarks in the simulation are shown. The results obtained using the EKF SLAM algorithm are shown in Figure 3. The estimates of the landmarks in Figure 3 are shown with the associated uncertainty by using the uncertainty ellipse based on the final value of the covariance matrix.

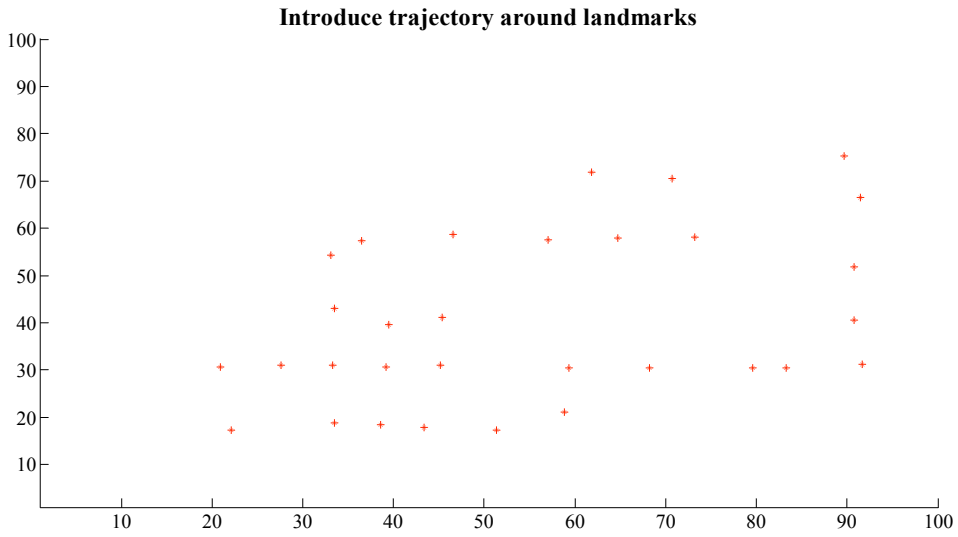


**Figure 2. Input trajectory and map used for EKF based SLAM.**

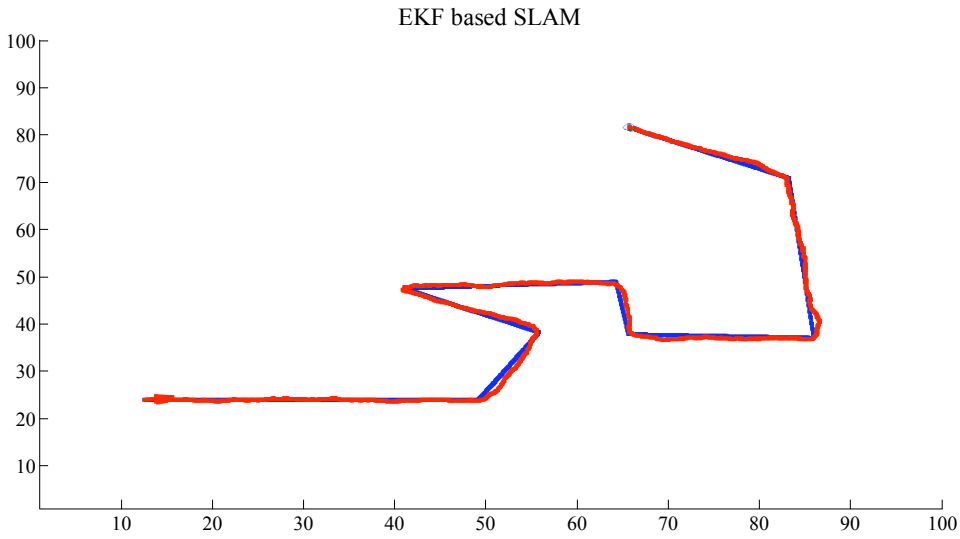


**Figure 3. EKF based SLAM results: Red line shows the estimated mobile platform position, with the blue line being the actual input trajectory. Landmark estimates are shown with uncertainty.**

### 3.3 Experimental work

In order to experimentally test the SLAM algorithms such as the one presented above, the experimental arrangement proposed in the previous report has been constructed, as shown in Figure 4. This arrangement represents a scaled version of a corridor leading to different

enclosures. The set-up is constructed such that the positions of the "walls" can be changed. In Figure 5, the Garcia (sensor platform described in the previous report) is shown as it navigates through the arrangement collecting data for SLAM. The Garcia navigates within the set-up using infra-red sensors and implementing obstacle avoidance. It is further equipped with a laser sensor for range and bearing measurement of landmarks and two encoders to provide positional information as it navigates. The laser and encoder data are wirelessly downloaded to a computer. Further, to track the performance of the SLAM algorithm, the mobile platform's movements are tracked using a camera. The position information obtained from the camera is to be used to evaluate the position estimates obtained from the SLAM algorithm.

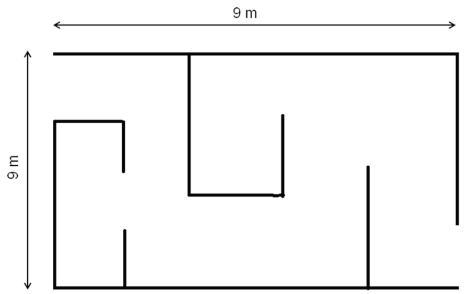


**Figure 4. Schematic (top) view of experimental set-up to demonstrate SLAM algorithms.**

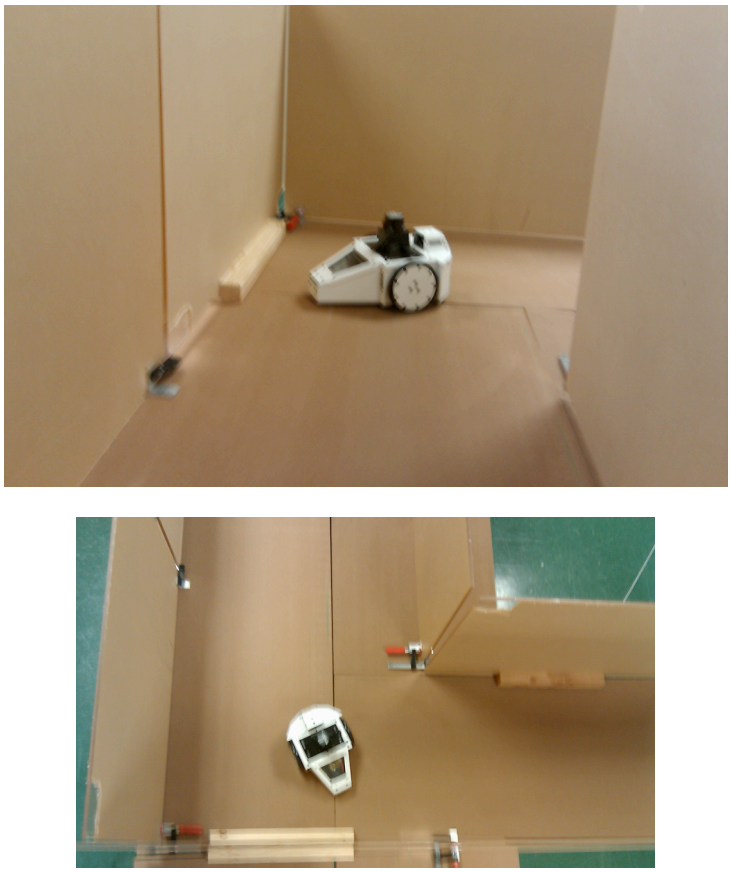

**Figure 5. (a) and (b): Data collection for SLAM using Garcia in experimental arrangement.**

In order to implement SLAM on the experimental data using the EKF algorithm described in the previous section, it was necessary to carry out additional processing on the range and bearing measurements obtained from the laser sensor. In the case of the numerical studies it was assumed that the landmarks were uniquely identifiable, but in the case of the experimental data obtained, the laser data obtained by reflections from the walls is not unique. This is known as the data association or correspondence problem.

**Data association or correspondence problem**: This problem arises due to uncertainty in uniquely identifying landmarks. This can lead to errors not only in the locations of the landmarks but also in the locations of the mobile agent as well as the sensor readings of range and bearings of the landmarks used to determine the position of the mobile agent in the map. In order to solve this problem, an additional algorithm (proposed by Dissanayake *et al*. 2001) is to be implemented for every observation as follows:

- Based on the measurement z(k), calculate the possible location of the landmark.
- Calculate the distance (Mahalanobis distance) between the estimated landmark position and every confirmed landmark already in the state vector.
- The measurement is associated with the landmark for which the distance calculated falls within a threshold.
- If two or more such landmarks qualify then the measurement is not associated with either.

- In order to maintain higher confidence in landmark estimates, only landmarks that are associated with a certain number of measurements are considered to be confirmed, else they are placed in a list of potential landmarks and steps 3-4 are implemented for every potential landmark.
- When the number of associated measurements increases beyond the threshold, the potential landmark is moved to the state vector as a confirmed landmark. Landmarks that do not reach this threshold within a certain amount of time are then rejected.

This algorithm implemented along with the EKF SLAM can solve the data association problem and therefore can be used to create a map from the experimental data. Implementation of this algorithm is currently in progress.

## 4. Planned Project Activities for the Next Quarter

An experimental study will be conducted to demonstrate the capabilities of SLAM to create the location specific defect map in a pipeline inspection setting. Furthermore, this study will also involve a comparison of the SLAM based inspection results and results obtained without the use of SLAM. In particular, two cases without SLAM will be studied as follows: i) path information based on odometer data from the mobile sensor platform and ii) path information using odometer data as well as external sensors. Further, these experiments will involve the use of ultrasonic sensors as these are the sensors that can be used in the context of pipeline inspection in the presence of oil. A scaled experimental pipeline arrangement with typical features seen in oil pipelines will be built at the University of Maryland to implement the proposed study.

## Abstract

### Motivation

Pigging refers to the practice of using pipeline inspection gauges (pigs) to perform the task of pipeline inspection without stopping the flow of the product in the pipeline. Intelligent pigs for pipeline inspection can be used to detect aspects such as corrosion, surface pitting, cracks or other weld defects by using sensors that detect changes in magnetic flux leakage or ultrasonics.

The goal of an inspection task is to not only to detect the defects but also to provide the location of the defect for monitoring and maintenance purposes. In order to achieve this objective, it is

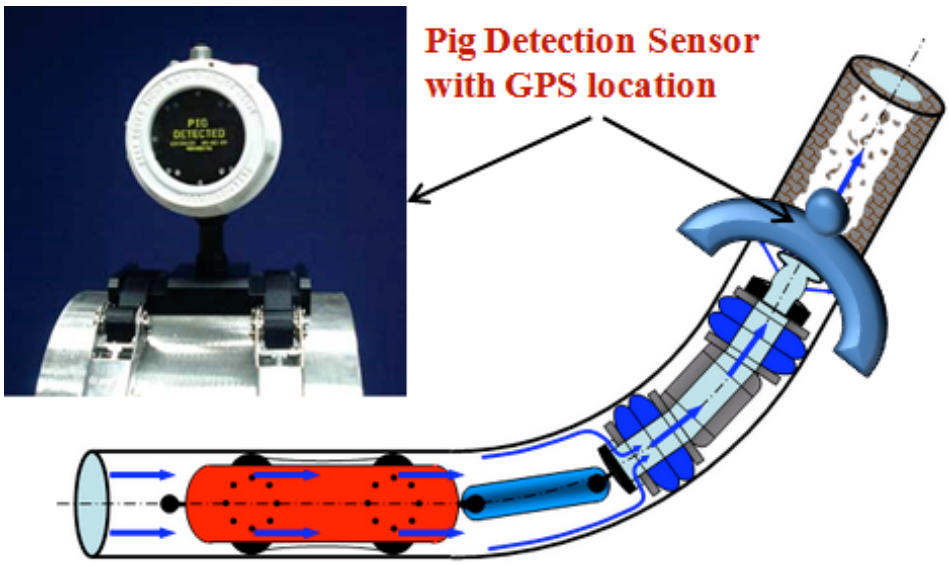


**Schematic of pig in a pipeline with external sensor to detect passage of the pig. An example of such an external sensor is shown in the inset.**

necessary to determine the path taken by the pig during inspection. Combining the position information over time with the sensor data can then provide a location-specific defect map. In current pigging techniques, location-specific defect information is determined by using a combination of internal sensors housed within the pig and external sensors that are located outside the pipeline (see schematic of Figure 1.1). First, the pig records positional information on the inspection path by using devices such as odometers and gyroscopes while the inspection is taking place. It is to be noted that the pig cannot communicate with external equipment during the inspection process, and hence, this mobile platform has no access to GPS location data. As the recorded position data is subject to incremental errors, location verification is further accomplished by the means of external sensors that are to used to follow the passage of the pig. The external sensors are equipped with GPS capabilities to determine the position at which the passage of the pig was detected. This positional data is combined with the pipeline evaluation data (corrosion, cracks, and so on) to provide a location-specific defect map. The drawback of this approach is that it requires the use of external sensors to detect the passage of the pig and provide the required accuracy in location information to create the defect map of the path obtained from the pig during inspection.

Simultaneous localization and mapping (SLAM) is a technique that can provide autonomy to mobile sensor platforms by building a consistent map and by simultaneously determining its location within the map (Durrant-Whyte and Bailey, 2006). The basic aim of the SLAM algorithm is to provide the capability to navigate through an unknown environment from an initially unknown location. In the SLAM problem, an agent or a mobile sensor platform makes use of relative sensing information between the agent and the surrounding environment in order to determine a map that constitutes the locations of landmarks or features in the surrounding environment as well as its own position within the map. SLAM techniques can therefore be employed to carry out inspection as they solve the problem of locating defects by building incremental maps using the sensor information. Walter, Hover, and Leonard (2008) studied the use of SLAM for ship hull inspection by using a remotely operated underwater vehicle. Features for map building in this case were manually selected. The SLAM algorithm implemented in this study was proposed by Walter, Eustice, and Leonard (2007). These earlier studies motivate the use of SLAM techniques with intelligent pigs to determine a map of the inspection path taken by the pig. Automatically selected features that are part of pipelines such as bends, joints, man-holes, and so on (see Figure 1.2) can be used in building the map and localizing the intelligent pig within that map. *The use of SLAM techniques can therefore facilitate the creation of the location specific defect map without the use of external sensors*.

**Schematic of pig in a pipeline. SLAM techniques can be applied to create the defect map by using features such as joints and bends shown above.**

## Approach

In order to develop and study the application of SLAM techniques to the pipeline inspection problem or an oil storage tank problem, it is necessary to get a good understanding of SLAM algorithms available in literature. This will help develop an understanding of the limitations in the current state of the art in SLAM and help build a background for further developments in the algorithms. To this end, SLAM based on the extended Kalman Filter (EKF) algorithm has been studied and the obtained simulation results are provided. Further, a ground based arrangement has been constructed in order to experimentally implement the SLAM algorithms and study them.

## EKF SLAM

In the SLAM problem, an agent or a mobile sensor platform makes use of relative sensing information between the agent and a feature from its environment for updating the agent's location as well as the associated map.

While the SLAM problem in the ideal noise-free case can be solved with relatively ease, noise in sensor measurements can be a primary impediment to robust SLAM. The convergence properties of the Kalman filter based SLAM algorithm was proved by Dissanayake, Newman, Clark, Durrant-Whyte, and Csorba (2001) for the linear Gaussian case. However, in order to extend the algorithm to include non-linear systems, various formulations such as the extended Kalman filter, unscented Kalman filter, particle filter and so on have been used. In this report, the extended Kalman filter based SLAM algorithm as shown in Thrun, Burgard, and Fox (2006) was analyzed for the two-dimensional case.

## Three-Year Schedule

*Phase II:*

April 1, 2009 to December 31, 2009: Carry out analytical and numerical investigations into SLAM algorithm based mobile platforms for representative geometrical profile measurements, construction of experimental test platforms, and preliminary experimental findings

January 1, 2010 to December 31, 2010: Continuation of analytical, experimental, and numerical efforts, with one of the focus areas to be development of appropriate communication and motion planning protocols for operations in harsh environments.

January 1, 2011 to December 31, 2011: Continuation of experimental and numerical studies and formulation of recommendations for appropriate sensor and mobile platform configurations for use in oil pipelines and storage tanks.

## References


[1] Dissanayake, M.W., Newman, P., Clark, S., Durrant-Whyte, H.F. and Csorba, M., “A Solution to the Simultaneous Localization and Map Building (SLAM) Problem,” Robotics and Automation, IEEE Transactions on, Vol.17, No.3, pp. 229–241, June 2001.

[2] Durrant-Whyte, H. and Bailey, T., 2006, “Simultaneous localization and mapping: part I," IEEE Robotics & Automation Magazine, Vol.13, no.2, pp. 99-110, June.

[3] Thrun, S., Burgard, W., and Fox, D., 2006, “Probabilistic Robotics,” MIT Press.

[4] Walter, M., Eustice, R., and Leonard, J., “Exactly Sparse Extended Information Filters for Feature-Based SLAM,” International Journal of Robotics Research, Vol. 26, No. 4, pp. 335–359, 2007.

[5] Walter, M., Hover, F., Leonard, J., "SLAM for Ship Hull Inspection using Exactly Sparse Extended Information Filters," *Robotics and Automation, 2008. ICRA 2008. IEEE International Conference on*, pp.1463–1470, 19–23 May 2008.

# Development of a Probabilistic Model for Degradation Effects of Corrosion-Fatigue Cracking in Oil and Gas Pipelines

**UMD Investigator: Mohammad Modarres**
**PI Investigators: Abdennour Seibi**
**GRA: Mohammad Nuhi**
**Start Date: Oct 2006**

## 1. Objectives/Abstract

This research continues phase-I mechanistic modeling of the *corrosion-fatigue* phenomenon for applications to pipeline health, risk and reliability management. The objective of this study is to perform additional mechanistic-based probabilistic models derived from physics of failure studies and validate them using the state-of-the-art experimental laboratory being developed at the PI as part of Phase I of this study. Where possible, observed field data from ADNOC operating facilities will be used to supplement observations from the laboratory experiments based on the well-established Bayesian approach to mechanistic model updating and validation developed in Phase I. Uncertainties about the structure of the mechanistic models as well as their parameters will also be characterized and accounted for when such models are applied. The proposed models will allow the end users (e.g., maintenance analysts and Inspection crew) to integrate observed performance data from a wide range of pipelines and selected refinery equipment, such as pumps, compressors and motor-operated valves. Admitting the fact that modeling all degradation mechanisms would be a challenging undertaking, the proposed research will additionally address the following degradation phenomena related to the petroleum industry: creep, pitting corrosion, and stress cracking corrosion (SCC).

## 2. Deliverables for the Completed Quarter

The following tasks have been completed in the last three months:

3.1. Theoretical effort in support of model development
- 3.1.1 Literature review on specifying the temperature dependencies of creep curve parameters
- 3.1.2 Results and discussion
- 3.1.3 Comparison between empirical and Evan's creep models by applying statistical methods
- 3.1.4 Separation of pitting and corrosion-fatigue WinBugs model program [1,2]

3.2 Experimental efforts in support of corrosion and creep model development.

## 3. Summary of Project Activities

### 3.1 Theoretical effort in support of model development

#### *3.1.1 Literature review on specifying temperature dependencies of creep curve parameters*

Creep is generally associated with time dependent plasticity of materials under a fixed stress at an elevated temperature, often greater than approximately 0.4-0.5$T_m$, where $T_m$ is the absolute melting temperature. The process is also temperature-dependent since the creep or dimensional change that occurs under an applied stress increases considerably as temperature increases [3,4].

Dorn [5], and Evans [6,7] suggest that temperature dependency has the exponential form like:

$$\dot{\varepsilon} = \frac{d\varepsilon}{dt} = A * \sigma^n * \exp(-Q/RT)$$

where $\dot{\varepsilon}$ is the strain rate of the creep and Q is the activation energy of the corresponding creep process and A is a material constant.

To study the temperature dependencies of creep parameters, we suggested the following empirical model (the details of which were described in the fourth quarterly report):

$$\varepsilon_c = a \cdot t^n + c \cdot t^m \cdot \exp(p \cdot t)$$

where $\varepsilon_c$ is the creep strain, t is the time and A, n, B, m, and p are stress and temperature dependent material parameters.

To explain the temperature dependency of the parameters of our generic empirical model, we used the temperature dependency diagram given by R. W. Bailey [8]. Bailey's temperature dependency diagram is given in Figure 1.

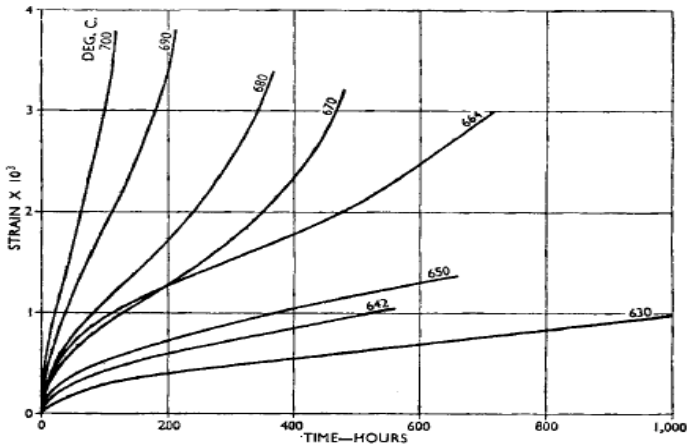


**Figure 1. Creep test results for Mo-V steel for a stress [8].**

We used the high temperature pipeline steel's data to evaluate the general temperature dependency of parameters a, n, c, m and p of the above mentioned empirical relation. Figure 2 shows the corresponding simulated data, evaluated by Digitalizer, Excel, and regression analysis of our WinBugs program.

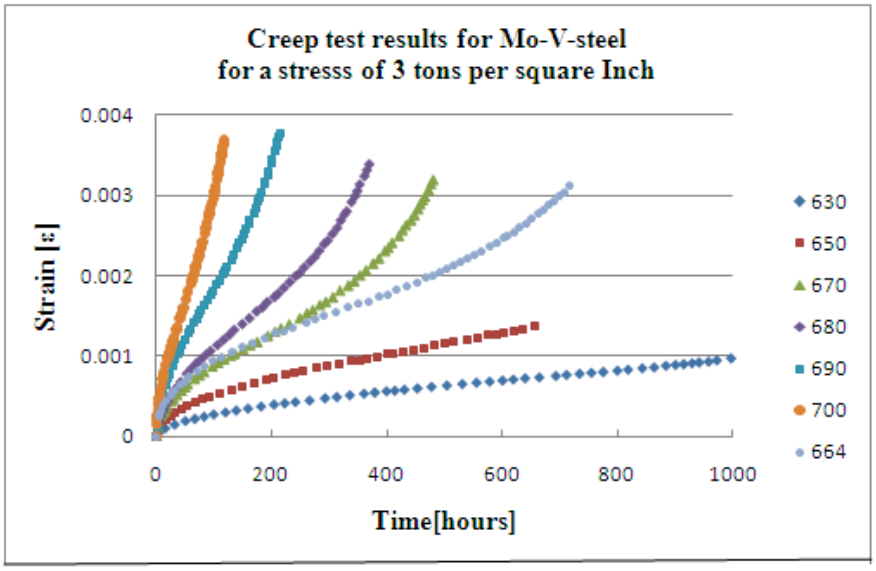


**Figure 2. Simulated creep test result for Mo-V steel.**

To do the regression analysis with Winbugs, one needs to guess prior values for the parameters. In fact, one of the major challenges in Winbugs is to choose the most appropriate values for the prior distribution of the parameters. This challenge will be explicitly issued in an upcoming paper.

### *3.1.2 Results and discussion*

Table 1 (a and b) shows the estimated parameters' data for high temperature pipeline Mo-V steel used for pressure vessels in power plants and oil refineries. The values of strains versus times are calculated for different temperatures by a given applied stress, using Excel and Winbugs maximum likelihood regression analysis.

**Table 1. Data calculated by regression analysis in Excel (a) and by Winbugs (b) to develop our model, evaluated under seven different temperature conditions for mo-v pipeline steel at given definite applied stresses**

**(a)**

| Parameters<br>T[K] | a | n | c | m | p |
|---|---|---|---|---|---|
| 903 | 2.33E-05 | 0.531649 | 8.60E-09 | 0.06101 | 0.00852 |
| 923 | 5.78E-05 | 0.4665 | 5.32E-06 | 0.2462 | 0.00288 |
| 937 | 1.33E-04 | 0.481 | 2.40E-06 | 0.324 | 0.0055 |
| 943 | 9.25E-05 | 0.48406 | 8.90E-08 | 1.019 | 0.00692 |
| 953 | 8.20E-05 | 0.563 | 2.18E-09 | 1.68 | 0.0087 |
| 963 | 1.44E-04 | 0.5398 | 3.08E-08 | 1.501 | 0.0116 |
| 973 | 2.10E-04 | 0.503 | 1.54E-07 | 1.67 | 0.0098 |

**(b)**

| Parameters<br>T[K] | a | n | c | m | p |
|---|---|---|---|---|---|
| 903 | 2.37E-05 | 0.5282 | 2.95E-08 | 0.03948 | 0.007653 |
| 923 | 5.55E-05 | 0.4779 | 3.70E-06 | 0.2812 | 0.003444 |
| 937 | 1.38E-04 | 0.3997 | 8.93E-06 | 0.324 | 0.004569 |
| 943 | 8.63E-05 | 0.4875 | 9.26E-06 | 0.2234 | 0.007852 |
| 953 | 8.68E-05 | 0.5496 | 1.86E-08 | 1.412 | 0.008295 |
| 963 | 1.50E-04 | 0.5174 | 1.41E-07 | 1.342 | 0.009735 |
| 973 | 2.11E-04 | 0.502 | 7.77E-08 | 1.875 | 0.007409 |

According to our calculations, parameters n, B and p are temperature independent. The temperature dependency of A and m parameters are given as:

$$\varepsilon(t) = a \cdot t^{n} + c \cdot t^{m} \cdot \exp(p \cdot t)$$
$$a = \alpha \cdot \exp(-E_A / kT)$$
$$m = \beta \cdot T + \gamma \quad or \quad m = \beta \cdot \exp(\gamma \cdot T)$$

$$\varepsilon(t) = [\alpha \cdot \exp(-E_A/kT)] \cdot t^{n} + c \cdot t^{(\beta \cdot T - \gamma)} \cdot \exp(p \cdot t)$$
$$E_A = Creep's \quad Activation \quad Energy$$

The use of exponential Arrhenius and linear temperature dependencies for empirical parameters is justified by several investigations [9-11]. It should be mentioned that the temperature and stress dependencies (evaluated in the last PI report) of parameters would be justified by the experiments on X-70 carbon steel and 7075 aluminum alloys in the physics of failure laboratory of the reliability department of the University of Maryland.

### *3.1.3 Comparison between empirical and Evan's creep models by applying statistical methods*

Usually the models cannot capture the first part of experimental creep curve for low creep ductility materials very well; further model modifications are needed to achieve an agreement with the experimental data. For instance, theta-projection model is modified by adding further term to it [12]. Then the nonlinear regression analysis is used to fit the data with the theta 4-parameter-projection and 6-parameter-extended theta models and compare the residuals as a measure of exactness [12, 13].

However, adding terms and extra parameters to the original model is not a good method to deal with the problem; moreover, it brings additional complications to the further calculations such as the regression analysis. To compare the results of our empirical model with those of other models, we took the same data and plotted the strain versus time for aluminum alloy tested at 100 $^{0}$C and 340 MPa stress. Figure 3 shows this plot together with other models.

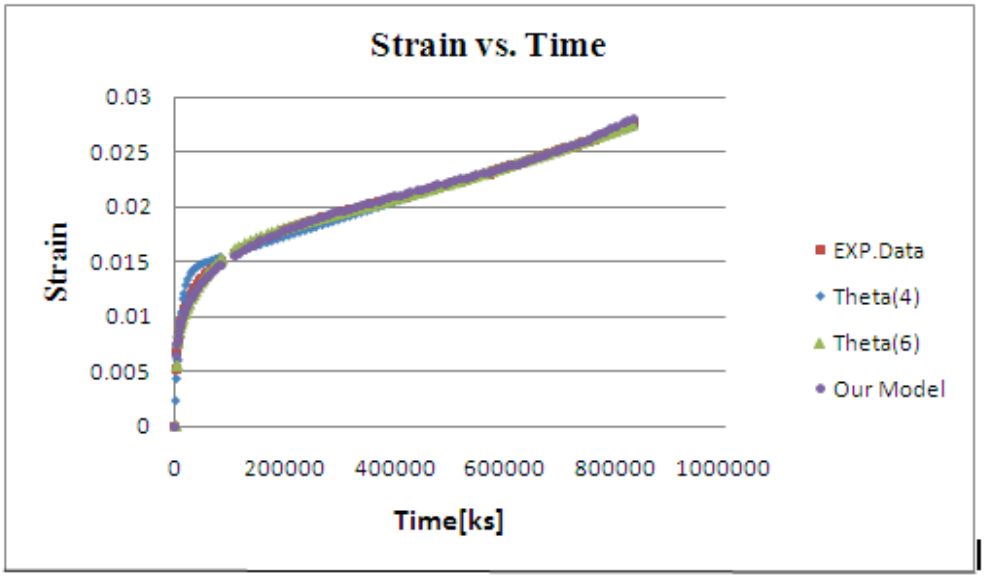


**Figure 3. Creep curves for an aluminum alloy tested at 100$^0$C and340 MPa with the use of three sets of data [12]**

As can be seen, our empirical model captures the primary part of creep curve without the need of any further modifications, which indicates that the power law model is an appropriate choice.
A complete description of the problem and results will be discussed in a new paper in the near future.

In order to compare the creep models, it is customary to calculate the residual of the model, as a measure of exactness, and plot it versus time. The smaller the residual, the better the model is.
Figure 4 compares the residuals of theta (4) and theta (6) creep models. As can be seen, the modified model (theta (6)) has the smaller residuals.

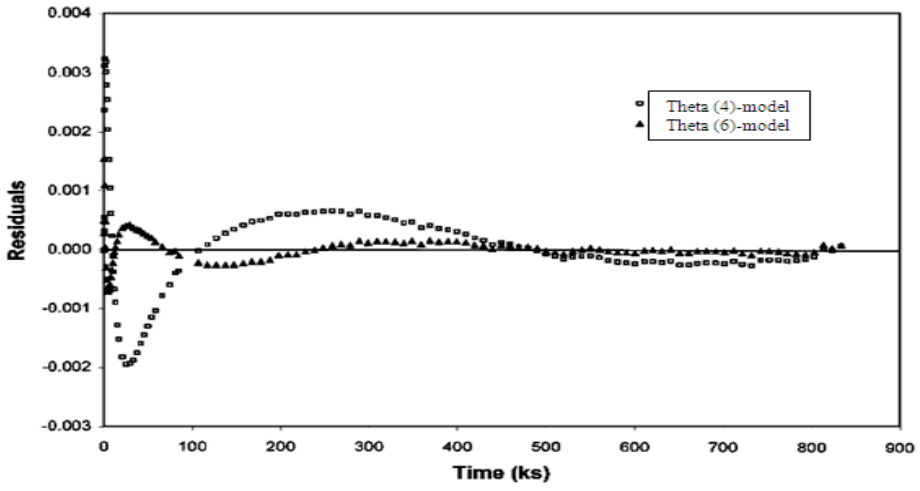


**Figure 4. Residual errors derived from Figure 3 [12].**

To compare our empirical model with the theta models, we calculated the residual of our model with the same data (aluminum alloy creep curve tested at 100 $^0$C and 340 MPa stress) that Evan used, and plotted them versus time. Figure 5 shows the results achieved by our empirical model.

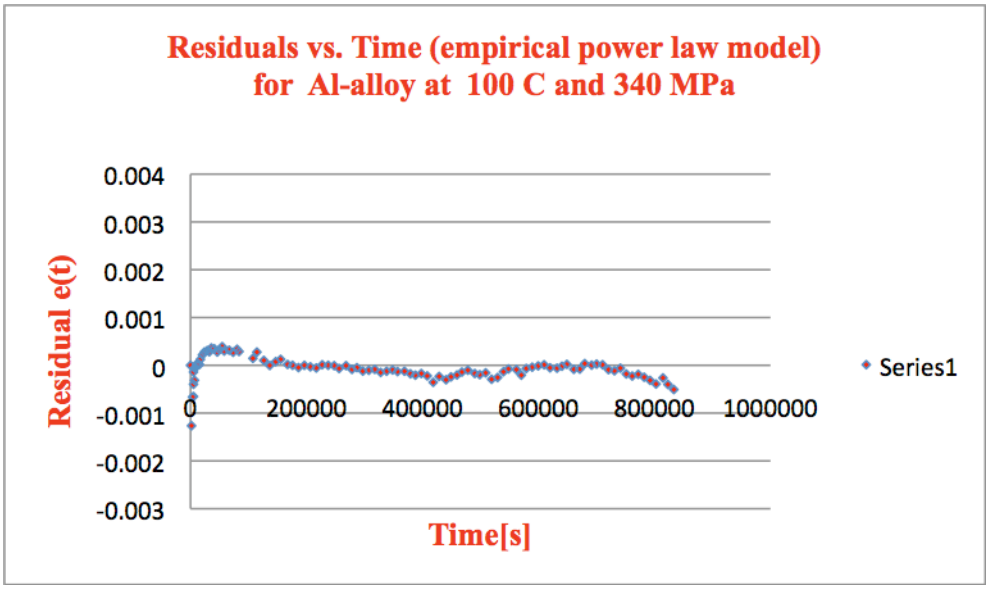


**Figure 5. Residual errors derived from Figure 3.**

In this part, we compared our model with Evan's theta models and showed that not only it captures the primary part of the creep curve without any further modifications, but also it has the smaller residual.

### *3.1.4 Separation of corrosion-fatigue WinBugs model program*

We renewed the separation of the Winbugs [3,4] corrosion-fatigue model to corrosion and corrosion-fatigue parts. This time, we used the pitting corrosion data from the PI intern program to update the Winbugs corrosion model. To update the corrosion-fatigue part, we used the corrosion-fatigue data taken from the Cortest equipment (when it was installed at the UMD). This study shows that the exponent of the parameters (in M. Chooka's model) doesn't need to be changed. The model will be ready for further data updating of the refinery data.

## 3.2 Experimental effort in support of model development

Dr. Abdennour Seibi also suggested extending the creep experiment on steel tubes under different purged gases or corrosive environments (for high temperature alloys used in heat exchangers) and multi-axial conditions. We are waiting to receive the material specification. As soon as we receive the specifications, we will make the appropriate grips for high-temperature creep corrosion experiments. Meanwhile, we designed and made the relevant stands and prepared the dial gauge for further experiments. Figure 6 shows the sample, gauge and stand fixed in a well-designed holder.

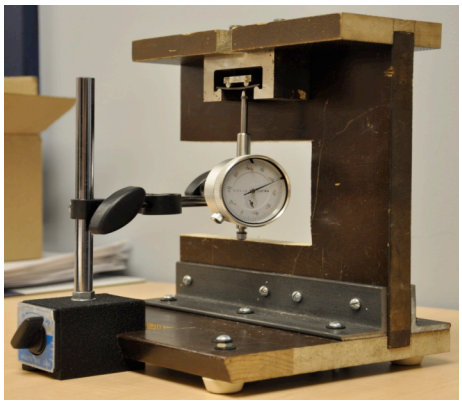

**Figure 6. Dial gauge and specimen fixed in the holder for applying definite stress on the sample.**

## 4. Future Work

The model verification and justification by performing creep experiments of Al 7075 dog-bone shaped specimens and X-70 carbon steel CT specimens will be the next phase of our study. This will be followed by the statistical evaluation of the experimental data and nonlinear regression analysis by the Matlab program. Finally, we will compare our model with other empirical models according to AIC (Akaike Information Criterion) [14], and BIC (Bayesian Information Criterion) [15].

## 5. Planned Project Activities for the Next Quarter

1. Simulation and refinement of the stress and temperature dependency of creep parameters of mechanistic models (PoF models) for creep will be performed. The related report will be submitted.
2. The corresponding simulation and statistical tool to help both model development and field applications will be done.
3. We are planning to realize Dr. Seibi's suggestion and design the related grips and extensometers.
4. We will prove the stand and the gauge for further stress in an experiment on the MTS machine.

## Appendix

### Approach

The test rig for this research exists the University of Maryland. The rig is used to conduct experimental studies reflecting field conditions for model validation developed in EERC Phase I & II. The equipment used would include MTS fatigue machine, heating furnace, corrosion test cells, autoclaves, multiphase flow loops, and testing machines for slow strain rate and crack growth testing. This activity also requires a complete line of monitoring equipment for evaluation of corrosion, scaling, and chemical treatment for field and laboratory. This test rig will be a useful tool for teaching, research, and possibly training field engineers from operating companies.

### Background

A number of deterministic models have been proposed to assess reliability and life-remaining assessment of pipelines. Among these models is the ASME B31G code, which is most widely used for the assessment of corroded pipelines. However, these models are highly conservative and lack the ability to estimate the true life of the pipelines and other equipment used in the oil industry. To address this shortcoming one needs to develop a best-estimate assessment of the life (to assess reliability and risk imposed) by these structures and equipment and assess the uncertainties surrounding such estimates. The proposed probabilistic mechanistic models, when fully developed, would integrate the physics of failure of the leading failure degradation phenomena in the oil industry into the formal risk and reliability assessments. Such physical models will be validated using a state of the art reliability assessment laboratory (being developed at PI). Uncertainties about the model structures and parameters will also be quantified. Such models will incorporate inspection data (characterizing limited and uncertain evidences). The rate of degradation is influenced by many factors such as pipeline materials, process conditions, geometry and location. Based on these factors, a best estimate of the structure (pipeline) or equipment (primarily valves, pumps and compressors) service life (reliability and remaining life) is to be calculated and uncertainties associated with the service life quantified. This estimate would serve as a basis that guides decisions regarding maintenance and replacement practices.

Phase I of this research focused on developing a corrosion-fatigue model. It successfully proposed such a model and developed an advanced laboratory for testing this phenomenon at PI. The current research continues in the same line of research by investigating and developing additional degradation phenomena (SCC, pitting corrosion, and creep-fatigue) and integrates these phenomena with reliability and risk assessment through four different tasks. The long-term objective of this research is to develop a comprehensive library of probabilistic mechanistic models for all degradation phenomena pertinent to structures (piping, and pressure vessels) used in the oil industry.

## Two-Year Schedule

This project involves three distinct tasks. The first task is the development of the mechanistic models, development of a corresponding simulation tool to help both model development and field applications. The second task focuses on experimental activities to generate relevant data to validate the proposed models of Task 1. Finally, the third task involves the actual validation of the models proposed in Task 1 with the experimental results obtained in Task 2, including Bayesian estimation of the model parameters.

**Task 1**: Develop the best estimate mechanistic (physics of failure) empirical models for pitting corrosion, SCC, and fatigue-creep. The model development involves the following activities.

Task1.1: Gather, review and select most promising physics of failure based methods and algorithms proposed in the literature.

- Literature surveys for creep and stress corrosion cracking (SCC) degradation mechanisms are almost completed and will be classified for finding the relevant models (100% done).

Task1.2: Select, develop or adopt a detailed mechanistic model (one deterministic model for each phenomenon) that properly describes the degradation process.

- Development of the mechanistic models and of a corresponding simulation tool to help both model development and field applications after classifying the models and choosing the appropriate one should be done in the next future (80% complete).

Task 1.3: Develop a Monte-Carlo based mathematical simulation routine on Matlab depicting the detailed mechanistic model of each degradation phenomenon (far faster than real-time).

- This part was completed for the empirical model developed based on the works of the PI interns for pitting corrosion. After proposing the similar models for SCC and creep-fatigue, it will be repeated (70% completed).

Task 1.4: Based on the results of the simulation a simplified empirical model that best describes the results of simulation will be proposed. Such a model relates the degradation (e.g., depth of the pit or the crack growth rate) to applied loads such as pipeline internal pressure and chemical composition of the product inside the pipeline, as a function of time or cycle of load application.

- This part is completed for the pitting corrosion and corrosion-fatigue, but further work will be done for the other failure mechanisms (70% complete).

**Task 2:** A PoF reliability analysis laboratory has been designed and being developed at PI. The advanced corrosion-fatigue purchased by the PI that was installed at the University of Maryland (the Cortest Rig) has already been sent to Cortest to ship to PI.

Task 2.1: Completing the remaining corrosion-fatigue tests being conducted by Mr. Nuhi and Chookah. (100% Completed)

Task 2.2: Pitting Corrosion Experiments (develop test plan, prepare samples and the facility, perform the test, and evaluate the test results) (100% Completed).

Task 2.3 SCC Experiments (develop test plan, prepare samples and the facility, perform the test, and evaluate the test results). (Not started yet)

- This task will be done in the near future, but SCC specimen holders have already designed and made according to the recent patents and ASTM-Standard.

Task 2.4 Creep-Fatigue Experiments: The equipments and samples are completely ready (100% completed); the tests will be performed in future and the results will be evaluated.

- A small-scaled corrosion-fatigue (or creep) chamber has been designed (not as part of this project), made and tested for dog-bone specimens and checked its workability on the UMD MTS machines using an Aluminum alloy sample. Another more sophisticated one has been already designed and tested for CT-specimens and is tested. Moreover, another chamber has been made for long specimens.
- A heating chamber has been designed and tested for creep experiments.
- New dial gauges with stand are prepared and will be tested in an experiment.

**Task 3:** This task involves modification, advancement and use of the WinBugs' Bayesian formalism for model validation using experimental data and integration of the field data and information including sensor-based data (acoustics and/or optical) to update the empirical models and estimate the remaining life of oil pipelines and structures. (70% Complete)

- The WinBugs' Bayesian formalism for model estimation and validation was developed as part of M. Chookah's work. This formalism is being updated and new applications of the formalism have been performed using past experimental data and new data of corrosion and fatigue obtained since departure of Dr. Chookah. Further work with this software for integration the experimental data has already be done.

## Schedule/Milestones/Deliverables

Tasks 1.1-1.3 (5/1/09-12/15/09); Task 1.4 (12/15/09-3/1/10); Task 2.1 (completed 7/1/09); Task2.2 (7/1/09-12/15/09); Task 2.3 (12/15/09 – 6/1/10); Task 2.4 (6/1/10-2/1/11); Task 3 (12/15/09-3/15/11).

The Cortest rig was boxed and shipped to the Cortest Corporation to test and send to **PI.**

The project is on schedules and there is no issue or delay at this point.

Dr. Seibi was appointed as a Co-Advisor of Mr. Nuhi.

## Visits

- Dr. A.Seibi visited UMD in July 2009
- Dr. A.Seibi visited UMD in July 2010
- Two PI students Abdullah Al Tamimi, and Mohammad Abu Daghah took parts at summer internship (2009).
- A PI student Taher Abu Seer took parts at summer internship (2010).
- Prof. Modarres attended the 1st Annual PI Partner Schools Research Workshop. The Petroleum Institute, Abu Dhabi, U.A.E. January 6-7, 2010.

## Papers Published and Prepared for Publication by the Team

1- M. Chookah, M. Nuhi, and M. Modarres, "Assessment of Integrity of Oil Pipelines Subject to Corrosion-Fatigue and Pitting Corrosion", presented by Prof. Modarres at the International Conference of Integrity- Reliability-Failure (IRF) in Porto, Portugal, July 20-24 2009**.** (The cost of the conference and associated travels was not covered by EERC)

2- M. Chookah, M. Nuhi, and M. Modarres, A. Seibi "A Probabilistic Physics of Failure Model for Prognostic Health Monitoring of Piping Subject to Pitting and Corrosion –Fatigue" is sent for publication to the "Journal of Reliability Engineering and System Safety".

3- A paper on "Development of a Database of Mechanistic Models of Failure for Application to Pipeline and Equipment Risk, Reliability and Health Management (Pitting Corrosion- Pit Depth and Density), prepared for publication at a conference. We are studying the possibility that the PI interns present the paper.

4- Abstract: "Reliability Analysis for Degradation Effects of Pitting Corrosion in Carbon Steel Pipes" is prepared and sent it to a conference in Italy and waiting for its acceptance in December.

5- Abstract: "Classification of Creep Models for Metallic Materials – A Comparative Study and Suggestions for Improvements is prepared and sent to the same conference and waiting for its acceptance in December.

## References


[1] Brooks, S. P. (1998). "Markov Chain Monte Carlo Method and its Application," The statistician, Royal Statistical Society, Vol. 47, No. 1, pp. 69-100.
[2] Spiegelhalter, D., Thomas, A., Best, N., and Lunn, D. (2003). WinBUGS 1.4, Manual.
[3] Metal Handbook (ASTM), Jeffery C. Gibeling "Creep deformation of Metals, polymers, ceramics, and composites".vol.8, Metal testing and evaluation p363-382, 2000
[4] Metal Handbook,(ASTM),Howard R. Voorhees, "Assessment and use of Creep-Rupture properties", vol. 8, Metal testing and evaluation p383-397, 2000
[5] Dorn, J.E. "Some fundamental experiments on high temperature creep, J.Mech.Phys.Solids,3,(1955)
[6] R.W. Evans and B. Wilshire," Introduction to creep", The institute of materials,1993
[7] R.W. Evans and B. Wilshire, *Creep of Metals and Alloys* (London: The Institute of Metals, 1985), pp. 203–243.
[8] R.W.Bailey, "Steam piping for high pressure and high temperature", A Archive: Proceeding of the institution of mechanical Engineers, 1847-1982, (vol. 1-196), vol. 164, 1951, pp.324-350.
[9] A.Klenk,et al., "Experimental and Numerical Investigation on Creep Damage Evolution", Key Engineering Materials, Trans. Tech. Publications, vol. 171-174 (2000), pp25-34.
[10] M.Malchin and Lupinc, "Modeling the high temperature creep behavior of a new single crystal Nickel based superalloy" Key Engineering Materials, Trans. Tech. Publications, vol. 171-174 (2000), pp245-252.
[11] F.R.N.Nabarro and H.L. de Villiers, "The Physics of Creep", Taylor & Francis Publisher, 1995, pp. 32-33.
[12] R.W.Evans, "The θ-projection method and the low creep ductility materials", Materials Science and Technology, January 2000, Vol.16.
[13] R.W.Evans, "Predicting times to low strain for a 1CrMoV rotor steel using a 6-$\mu$ projection technique", Journal of Material Science, 35 (2000) 2937 – 2948
[14] Akaike information criterion, en.wikipedia.org/wiki/Akaike_information_criterion
[15] Bayesian information criterion, en.wikipedia.org/wiki/Bayesian_information_criterion